

# The Characterisation and Modelling of the Wireless Propagation Channel in Small Cells Scenarios

Cheng Fang

This is a digitised version of a dissertation submitted to the University of Bedfordshire.

It is available to view only.

This item is subject to copyright.

**THE**  
**CHARACTERISATION AND MODELLING**  
**OF THE WIRELESS PROPAGATION CHANNEL**  
**IN SMALL CELLS SCENARIOS**

**CHENG FANG**

A thesis submitted for the degree of

**DOCTOR OF PHILOSOPHY**

September, 2015

**UNIVERSITY OF BEDFORDSHIRE**

## DECLARATION

I declare that this thesis is my own unaided work. It is being submitted for the degree of

Doctor of Philosophy at the University of Bedfordshire.

It has not been submitted before for any degree or examination in any other University.

Name of candidate: Cheng Fang

Signature:

Date: 10 September 2015

## ABSTRACT

The rapid growth in wireless data traffic in recent years has placed a great strain on the wireless spectrum and the capacity of current wireless networks. In addition, the makeup of the typical wireless propagation environment is rapidly changing as a greater percentage of data traffic moves indoors, where the coverage of radio signals is poor. This dual fronted assault on coverage and capacity has meant that the tradition cellular model is no longer sustainable, as the gains from constructing new macrocells falls short of the increasing cost. The key emerging concept that can solve the aforementioned challenges is smaller base stations such as micro-, pico- and femto-cells collectively known as small cells. However with this solution come new challenges: while small cells are efficient at improving the indoor coverage and capacity; they compound the lack of spectrum even more and cause high levels of interference. Current channel models are not suited to characterise this interference as the small cells propagation environment is vast different. The result is that overall efficiency of the networks suffers.

This thesis presents an investigation into the characteristics of the wireless propagation channel in small cell environments, including measurement, analysis, modelling, validation and extraction of channel data. Two comprehensive data collection campaigns were carried out, one of them employed a RUSK channel sounder and featured dual-polarised MIMO antennas. From the first dataset an empirical path loss model, adapted to typical indoor and outdoor scenarios found in small cell environments, was constructed using regression analysis and was validated using the second dataset. The model shows good accuracy for small cell environments and can be implemented in system level simulations quickly without much requirements.

Using the same data the values of key channel parameters, which are required for a range of wireless network planning applications, were extracted for indoor and outdoor scenarios. Comparative study of these parameter values provides useful characterisation of the small cell wireless channel. Furthermore, the signal strength and correlation of dual-polarised MIMO sub-channels were investigated, the result showing significant, yet consistent differences amongst co-polar and cross-polar sub-channels, with respect to frequency and receiver orientation. The result was used to produce a new polarisation diversity combination scheme and test against the data shows significant improvement in channel capacity.

The knowledge gained through the investigation provide a better understanding of the intricacies of the small cell propagation environment, which will help to increase the efficiency of the overall wireless network, allowing it to be in the best possible shape to face the challenges yet to come.

## ACKNOWLEDGEMENTS

I am very grateful to my Director of Studies: Dr Enjie Liu, for her guidance and patience throughout. I also want to thank Professor Ben Allen, my second supervisor, for his invaluable guidance and support. I am also indebted to Professor Jie Zhang, who provided me the opportunity to undertake this study, as well as for his help along the way.

I also want to state my gratitude to the Department of Computer Science and Technology, University of Bedfordshire, and Ranplan Wireless Network Design Ltd, for their financial support, without which, all of this would not have been possible.

Special thanks have to be given to Professor Fredrik Tufvesson and Dr Andres Alayon Glaznov, for their help and technical expertise during the measurement campaign as well as during post processing of the measurement data. The latter also provided me with valuable mentorship towards my understanding of wireless concepts. Also thanks to Lunds Tekniska Högskola, for lending their expensive RUSK channel sounder equipment for the measurement campaign.

I should also extend my thanks to my colleagues Dr Xu Zhang, Dr Shyam Mahato and Dr Zhihua Lai for their help, suggestions, encouragement and support throughout my study.

Finally, I would like to thank my family, including my partner Jiayue Huang, because they were always there for me.

# TABLE OF CONTENTS

<b>DECLARATION</b>	<b>I</b>
<b>ABSTRACT</b>	<b>II</b>
<b>ACKNOWLEDGEMENTS</b>	<b>IV</b>
<b>TABLE OF CONTENTS</b>	<b>V</b>
<b>LIST OF FIGURES</b>	<b>VIII</b>
<b>LIST OF TABLES</b>	<b>X</b>
<b>LIST OF PUBLICATIONS</b>	<b>XI</b>
<b>CHAPTER 1 INTRODUCTION</b>	<b>1</b>
1.1 Growth of Mobile Wireless Technology	2
1.2 Emerging Trends and associated Challenges	5
1.2.1 Growth of Indoor Wireless Data Traffic	5
1.2.2 Small Cells	7
1.2.3 Heterogeneous Networks and Interference	8
1.3 The need for Propagation Models	10
1.4 Aim and Objectives of this Thesis	12
1.5 Contributions of this Thesis	14
<b>CHAPTER 2 PROPAGATION PREDICTION MODELS</b>	<b>16</b>
2.1 Background and General Considerations	17
2.1.1 Small Scale Propagation Models	21
2.1.2 Large Scale Propagation Models	22
2.2 Overview of Propagation Models	24
2.2.1 Deterministic Models	24
2.2.2 Semi-deterministic Models	28
2.2.3 Semi-empirical Models	31
2.2.4 Empirical Models	33
2.2.5 Hybrid Models	37
2.2.6 Summary	38

---

<b>CHAPTER 3</b>	<b>EMPIRICAL PATH LOSS MODEL.....</b>	<b>39</b>
3.1	Introduction .....	40
3.2	Channel Measurement Campaign .....	42
3.2.1	<i>Theoretical Background.....</i>	<i>42</i>
3.2.2	<i>Channel measurement System .....</i>	<i>43</i>
3.2.3	<i>Measurement set-up .....</i>	<i>44</i>
3.2.4	<i>Measurement Location.....</i>	<i>47</i>
3.3	Empirical Path Loss Model.....	52
3.3.1	<i>Data Reduction .....</i>	<i>52</i>
3.3.2	<i>Path Loss Formulation .....</i>	<i>53</i>
3.3.3	<i>Path Loss Model .....</i>	<i>54</i>
3.4	Model Validation .....	62
3.4.1	<i>Model comparison for Luton data .....</i>	<i>64</i>
3.4.2	<i>Comparison between Lund and Luton datasets .....</i>	<i>65</i>
3.5	Summary.....	67
<b>CHAPTER 4</b>	<b>CHANNEL PARAMETERS AND RELATED STATISTICS .....</b>	<b>68</b>
4.1	Introduction .....	69
4.2	Analysis of Channel Parameters .....	70
4.2.1	<i>RMS Delay Spread .....</i>	<i>71</i>
4.2.2	<i>Coherence Bandwidth.....</i>	<i>75</i>
4.2.3	<i>RMS Angular Spread.....</i>	<i>78</i>
4.3	Summary.....	80
<b>CHAPTER 5</b>	<b>ANTENNA POLARISATION EFFECTS ON RECEIVED SIGNAL.....</b>	<b>81</b>
5.1	Introduction .....	82
5.2	Considerations and Methodologies.....	85
5.2.1	<i>Methodological issues relating to Distribution Analysis.....</i>	<i>87</i>
5.2.2	<i>Methodological Issues Relating to Correlation Analysis.....</i>	<i>90</i>
5.3	Polarisation Effects on Signal Distribution.....	93
5.3.1	<i>Polarisation effects on amplitude distribution in relation to frequency .....</i>	<i>93</i>
5.3.2	<i>Polarisation effects on phase distribution in relation to frequency.....</i>	<i>99</i>
5.3.3	<i>Polarisation effects on amplitude distribution in relation to Rx orientation .....</i>	<i>105</i>
5.3.4	<i>Polarisation effects on phase distribution in relation to Rx orientation .....</i>	<i>108</i>
5.4	Polarisation Effects on Signal Correlation.....	110
5.4.1	<i>Polarisation effects on amplitude correlation in relation to frequency.....</i>	<i>112</i>



---

5.4.2	<i>Polarisation effects on phase correlation in relation to frequency</i> .....	116
5.4.3	<i>Polarisation effects on signal correlation in relation to frequency</i> .....	118
5.4.4	<i>Polarisation effects on signal correlation across receiver orientation</i> .....	120
5.4.5	<i>Polarisation effects on coherence bandwidth</i> .....	124
5.4.6	<i>Correlation of previous findings observed from different positions</i> .....	127
5.5	Data based analysis of polarisation diversity gain .....	131
5.5.1	<i>Effect of cross-polar discrimination on selection gain</i> .....	133
5.5.2	<i>Effect of sub-channel correlation on diversity gain</i> .....	135
5.5.3	<i>Polarisation diversity combination scheme</i> .....	136
5.6	Summary.....	141
<b>CHAPTER 6 CONCLUSIONS AND FUTURE WORK .....</b>		<b>143</b>
6.1	Conclusions .....	144
6.2	Future Work.....	147
<b>BIBLIOGRAPHY .....</b>		<b>148</b>
<b>LIST OF ACRONYMS .....</b>		<b>162</b>

# LIST OF FIGURES

FIGURE 1-1: GLOBAL NUMBER WIRELESS SUBSCRIPTIONS, AND PER 100 INHABITANTS, 1995-2013.....	2
FIGURE 1-2: ROLLING ANNUAL CUSTOMER GROWTH FOR EUROPE 1991 – 2008.....	3
FIGURE 1-3: DOWNLINK TRAFFIC FROM CELLULAR HANDSETS WORLDWIDE, BY REGION, 2008 – 2015.....	4
FIGURE 1-4: SERVICE PROPORTIONS OF DOWNLINK WIRELESS NETWORK TRAFFIC IN DEVELOPED REGIONS.....	6
FIGURE 1-5: HETEROGENEOUS CELLULAR NETWORK AND SOME OF THE ASSOCIATED CHALLENGES.....	8
FIGURE 2-1: ATTENUATION FACTOR FOR OKAMURA MODEL .....	35
FIGURE 3-1: RUSK LUND CHANNEL SOUNDER.....	44
FIGURE 3-2: DUAL POLARISED ANTENNA ARRAYS: TX (LEFT), RX (RIGHT).....	45
FIGURE 3-3: THE E-HUSET BUILDING OF LUND INSTITUTE OF TECHNOLOGY AND ITS SURROUNDING AREAS.....	47
FIGURE 3-4: OVERVIEW OF MEASUREMENT POSITIONS.....	48
FIGURE 3-5: MEASUREMENT POSITIONS IN ROOMS 2425-30 .....	49
FIGURE 3-6: MEASUREMENTS IN OFFICES IMMEDIATELY NEIGHBOURING THE TX. ....	50
FIGURE 3-7: PATH LOSS VS. T-R SEPARATION WITH LLS FIT.....	54
FIGURE 3-8: PATH LOSS VS. T-R SEPARATION SHOWING SEPARATE SCENARIOS .....	55
FIGURE 3-9: FIT OF PROPOSED PATH LOSS MODEL AGAINST MEASURED DATA.....	58
FIGURE 3-10: GOODNESS OF FIT OF MODEL (3.6) FOR DIFFERENT VALUES OF $W$ .....	59
FIGURE 3-11: PREDICTED VS. MEASURED PATH LOSS FOR MODEL (3.6).....	60
FIGURE 3-12: OVERVIEW OF THE LUTON MEASUREMENT CAMPAIGN .....	62
FIGURE 3-13: SCATTER PLOT OF THE LUTON DATA COMPARING THE PREDICTIONS MADE BY THE MODELS .....	64
FIGURE 3-14: COMPARISON BETWEEN MEASURED AND PREDICTED PATH LOSS.....	65
FIGURE 4-1: RMS DELAY SPREAD PDF: I2I (TOP), I2O (BOTTOM), RC FACING TX (LEFT), RX OPPOSITE TX (RIGHT) .....	72
FIGURE 4-2: RMS DELAY SPREAD CDF COMPARISON: I2I (LEFT), I2O (RIGHT) .....	73
FIGURE 4-3: COHERENCE BANDWIDTH PDF FOR I2O (TOP) AND I2I (BOTTOM) .....	76
FIGURE 4-4: COHERENCE BANDWIDTH CDF COMPARISON.....	77
FIGURE 4-5: PDF OF ANGLE OF MAXIMAL RECEIVED POWER .....	78
FIGURE 4-6: PDF OF RMS ANGULAR SPREAD .....	79
FIGURE 5-1: PROPAGATION OF A RADIO WAVE .....	83
FIGURE 5-2: AN ILLUSTRATION OF THE CONTROL CHART. ....	90
FIGURE 5-3: AMPLITUDE DISTRIBUTION OF THE 4 POLARISATION SETTINGS ACROSS 81 FREQUENCIES .....	94
FIGURE 5-4: HISTOGRAM OF SIGNAL AMPLITUDE AND FITTINGS TO THREE DISTRIBUTIONS .....	96

FIGURE 5-5: VARIATION OF AMPLITUDE MEAN ACROSS THE FREQUENCY DOMAIN. ....	97
FIGURE 5-6: PHASE DISTRIBUTION OF THE 4 POLARISATION SETTINGS ACROSS 81 FREQUENCIES .....	99
FIGURE 5-7: HISTOGRAM OF PHASE DISTRIBUTION AT 2.6 GHz, SHOWING A NON-UNIFORM DISTRIBUTION.....	101
FIGURE 5-8: SIMULATED PHASE DISTRIBUTION WITH NON-ZERO MEAN .....	102
FIGURE 5-9: Q-Q PLOT OF SIGNAL PHASE DATA AT FREQUENCY 2.6 GHz AND UNIFORM CDF.....	103
FIGURE 5-10: VARIATION OF PHASE MEAN ACROSS THE FREQUENCY DOMAIN. ....	104
FIGURE 5-11: AMPLITUDE DISTRIBUTION OF THE 4 POLARISATION SETTINGS ACROSS 16 RX ORIENTATIONS .....	105
FIGURE 5-12: HISTOGRAM OF SIGNAL AMPLITUDE AND FITTINGS TO THREE DISTRIBUTION DENSITIES .....	106
FIGURE 5-13: VARIATION OF AMPLITUDE MEAN ACROSS THE 16 RECEIVER ORIENTATIONS.....	107
FIGURE 5-14: PHASE DISTRIBUTION OF THE 4 POLARISATION SETTINGS ACROSS 16 RX ORIENTATIONS .....	108
FIGURE 5-15: VARIATION OF PHASE MEAN ACROSS THE 16 RECEIVER ORIENTATIONS.....	109
FIGURE 5-16: HEATMAP OF AMPLITUDE CORRELATION BETWEEN SAME POLARISATION SETTINGS.....	114
FIGURE 5-17: HEATMAP OF AMPLITUDE CORRELATION BETWEEN DIFFERENT POLARISATION SETTINGS .....	115
FIGURE 5-18: HEATMAP OF PHASE CORRELATION BETWEEN SAME POLARISATION SETTINGS.....	116
FIGURE 5-19: HEATMAP OF PHASE CORRELATION BETWEEN DIFFERENT POLARISATION SETTINGS. ....	117
FIGURE 5-20: HEATMAP OF SIGNAL CORRELATION BETWEEN SAME POLARISATION SETTINGS.....	118
FIGURE 5-21: HEATMAP OF SIGNAL CORRELATION BETWEEN DIFFERENT POLARISATION SETTINGS .....	119
FIGURE 5-22: HEATMAP OF AMPLITUDE CORRELATION IN RELATION TO RX ORIENTATION.....	121
FIGURE 5-23: HEATMAP OF PHASE CORRELATION IN RELATION TO RX ORIENTATION.....	122
FIGURE 5-24: HEATMAP OF SIGNAL CORRELATION IN ASSOCIATION WITH RX ORIENTATION .....	123
FIGURE 5-25: HEATMAP OF SIGNAL CORRELATION ACROSS THE FREQUENCY DOMAIN .....	125
FIGURE 5-26: COHERENCE PROFILE GENERATED FROM CORRELATION MATRIX.....	126
FIGURE 5-27: CORRELATION OF PHASE CORRELATION ACROSS MEASURING SITES.....	128
FIGURE 5-28: CORRELATION OF AMPLITUDE CORRELATION ACROSS MEASURING SITES.....	129
FIGURE 5-29: CORRELATION OF SIGNAL CORRELATION ACROSS MEASURING SITES.....	130
FIGURE 5-30: 2 × 2 MIMO SYSTEM WITH DUAL-POLARISED ANTENNAS.....	132
FIGURE 5-31: POLARISATION DIVERSITY GAIN AS A RESULT OF XPD.....	135
FIGURE 5-32: POLARISATION DIVERSITY COMBINATION SCHEME FOR DUAL-POLARISED MIMO CHANNEL.....	136
FIGURE 5-33: POLARISATION DIVERSITY GAIN FOR EACH POLARISATION SETTING ACROSS DIFFERENT FREQUENCIES	137
FIGURE 5-34: MEAN POLARISATION DIVERSITY GAIN ACROSS ALL MEASUREMENT POSITIONS FOR DIFFERENTLY POLARISED SUB-CHANNELS .....	138
FIGURE 5-35: HISTOGRAMS OF THE RAW CHANNEL POWER FOR DIFFERENT POLARISATION SETTINGS IN COMPARISON WITH POWER ACHIEVED THROUGH PROPOSED DIVERSITY COMBING SCHEME .....	139
FIGURE 5-36: CDF OF SUB-CHANNEL POWER FOR DIFFERENT POLARISATION SETTINGS IN COMPARISON WITH POLARISATION DIVERSITY COMBING SCHEME .....	140

## LIST OF TABLES

TABLE 3-I: MEASUREMENT PARAMETERS FROM THE MEASUREMENT DATA FILE .....	46
TABLE 3-II CONFIGURATION OF THE ATTENUATOR AND LNA IN ROOMS 2325-30 .....	50
TABLE 3-III CONFIGURATION OF THE ATTENUATOR AND LNA IN ROOMS 2313-26 .....	51
TABLE 3-IV DETAILS OF THE I2O MEASUREMENT POSITIONS .....	51
TABLE 3-V: PARAMETER VALUES FOR THE COMPLETE DATA SET .....	55
TABLE 3-VI: PARAMETER VALUES FOR EACH SCENARIO .....	56
TABLE 3-VII: PARAMETER VALUES FOR MODEL (3.6) .....	57
TABLE 3-VIII: PARAMETER VALUES OF EACH SCENARIO FOR PROPOSED MODEL.....	61
TABLE 3-IX: PARAMETER VALUES OF MODEL (3.6) FOR LUTON DATA .....	66
TABLE 3-X: PARAMETER COMPARISON BETWEEN DATASETS AND MODELS .....	66
TABLE 4-I: RMS DELAY SPREAD FOR SELECTED R <sub>x</sub> COLUMNS .....	74
TABLE 4-II: COHERENCE BANDWIDTH .....	77
TABLE 4-III: SUMMARY OF THE CHANNEL PARAMETERS.....	80

## LIST OF PUBLICATIONS

C. Fang, B. Allen, E.J. Liu, J. Zhang, A.A. Glazunov, F. Tufvesson, "Empirical indoor-to-outdoor and building-to-building propagation model at 2.6 GHz," *IC1004 Joint workshop on Small Cell Cooperative Communications*, May 2012

C. Fang, B. Allen, E.J. Liu, P. Karadimas, J. Zhang, A.A. Glazunov, F. Tufvesson. "Indoor-indoor and indoor-outdoor propagation trial results at 2.6 GHz," *Loughborough Antenna and Propagation Conference*, Nov 2012

X. Gao, A.A. Glazunov, J. Weng, C. Fang, J. Zhang, F. Tufvesson, "Channel measurement and characterization of interference between residential femto-cell systems," *In Antennas and Propagation (EUCAP), Proceedings of the 5th European Conference on (pp. 3769-3773). IEEE*, Apr 2011

C. Fang, M.U. Rehman, E.J. Liu, "A polarisation diversity combining scheme based on analysis of sub-channel correlation in dual-polarised MIMO systems," submitted to *IEEE Transactions on Antenna and Propagations*.

# CHAPTER 1

## INTRODUCTION

*This chapter reports on the growth of wireless technology, in particular growth of indoor wireless traffic, and how the concepts of small cells is viewed as key to meet to the ever increasing network coverage and capacity requirements. One significant challenge facing small cells is the issue of spectrum scarcity leading to signal interference, which is described here. Further it is shown that the problem of interference can be greatly mitigated by developing accurate propagation prediction model for this newly emerged propagation environment.*

*In this thesis, the term “small cells scenarios” refers to propagation channels with one or both ends of the link located within or close to buildings. This includes indoor, indoor-to-outdoor, outdoor-to-indoor and building-to-building (indoor-outdoor-indoor) propagation scenarios where the link distance is within the ranges of small cells.*

## 1.1 Growth of Mobile Wireless Technology

Mobile wireless technology has experienced tremendous growth in recent years. Aspects of the growth include increased traffic volume, extended range of applications, and new air interfaces delivering the service. All of these factors contribute to the issue of spectrum scarcity, which ultimately leads to increased levels of signal interference. [1]

Initially, the main utility of wireless technology was to provide mobile voice communication. The mobility aspect was a huge success which ensured the technology's remarkable and continuing growth. In terms of volume of traffic, the growth is comprised of two factors: the number of subscribers, shown in Figure 1-1, and the amount of data usage per subscriber. Both factors have experienced, or is experiencing, periods of exponential growth in different markets around the world.

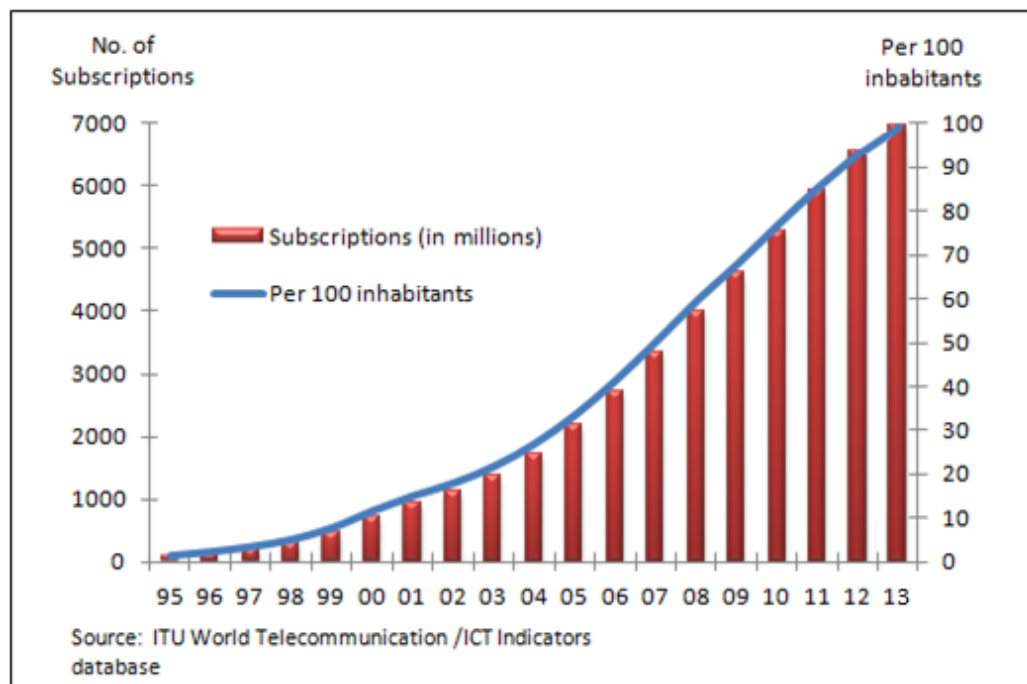
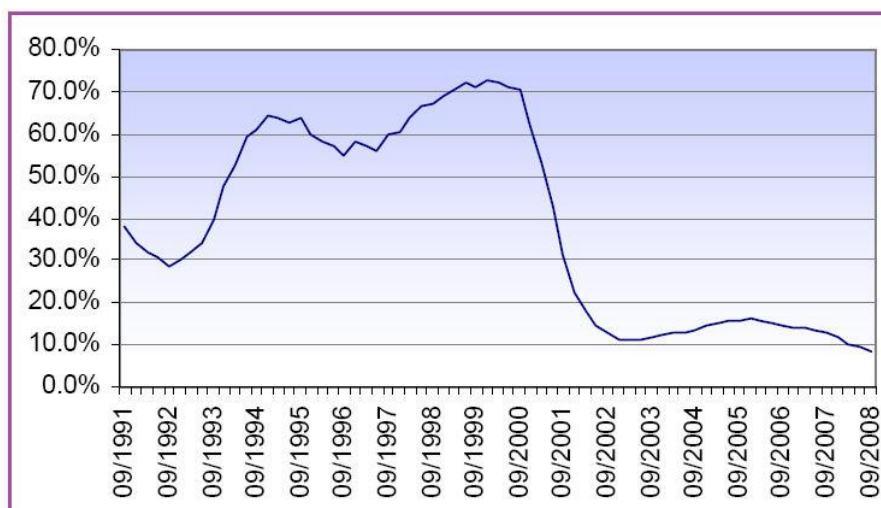


Figure 1-1: Global number wireless subscriptions, and per 100 inhabitants, 1995-2013

The European market was one of the first to develop, Figure 1-2 shows that it experienced the highest rate of subscriber growth during the 1990s. Although this growth factor dropped off as the market neared 100% saturation, the data usage factor maintained a high growth rate throughout the 2000s, which continues to the present day and beyond, sees Figure 1-3. In emerging markets such as Central/Southern America and Africa, both the growth in subscribers and the data traffic per subscriber are contributing making these markets the fastest growing mobile markets in the world [2].

**Europe: Rolling Annual Customer Growth, Q3 91 - Q3 08**



**Figure 1-2: Rolling annual customer growth for Europe 1991 – 2008**

According to Cisco, Global IP traffic increased eightfold between 2006-2011 with the majority of the growth attributed to wireless traffic, and by 2016, traffic from wireless devices will exceed those from wired devices [3]. This explosive growth in wireless traffic creates great demands on the spectrum which is a limited resource. At the same time, the application of wireless technology has expanded to facilitate the likes of video calling, mobile internet, satellite navigation, WLAN, personal medical devices, and electronic interfaces. Each new application requires their



own band to operate in and many of them require communicating volumes of data that are orders of magnitudes greater than voice communication. Furthermore, developments on the horizon such as wireless cloud computing and wireless energy transfer could have paradigm shifting effects [4, 5]. Many of these technologies operate in wireless networks of different scales, from global satellite networks all the way down to personal area networks and wireless networks inside electronic devices. These networks exhibit vastly different characteristics such as transmission distance, frequency, altitude, network topology and environmental obstacles, and each characteristic affects the signal attenuation in various ways.

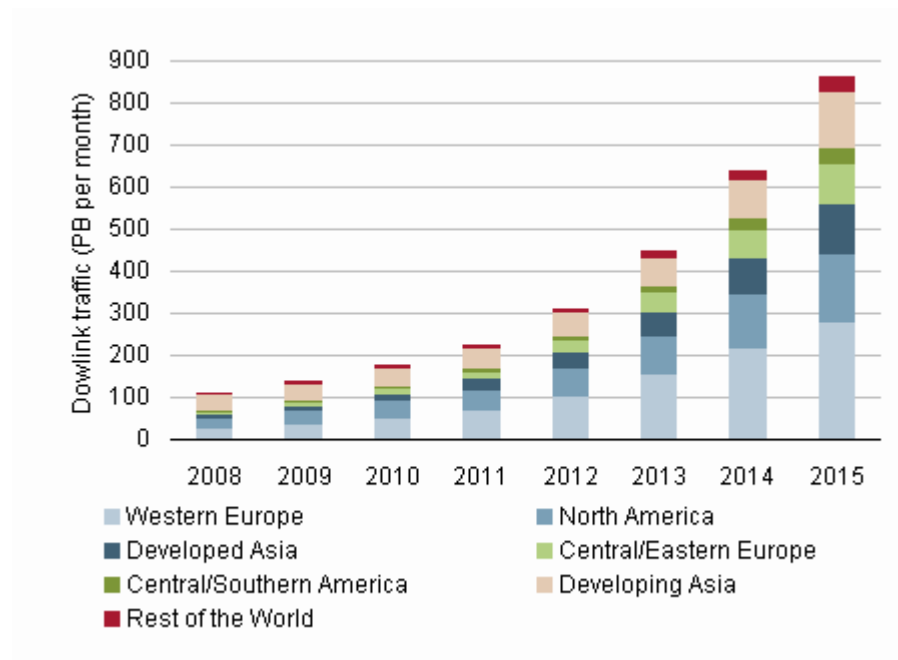


Figure 1-3: Downlink traffic from cellular handsets worldwide, by region, 2008 – 2015

## **1.2 Emerging Trends and associated Challenges**

Through many years of sustained growth and evolution, greater flexibility and convenience to mobile customers have been achieved. Traditional problems such as lack of coverage, peak hour dropped calls and expensive inter-operator calls have been greatly reduced. New services such as web browsing and video conferences have allowed customers to use their mobile phones in different ways and through changing habits new trends gradually appear in the volume of data communicated wirelessly over the world. These changes affect the efficiency and operation ability of existing infrastructures, creating new gaps and technical challenges that need to be addressed.

### **1.2.1 Growth of Indoor Wireless Data Traffic**

One of the key trends underlying the evolution of wireless communication has been the increase in the percentage of indoor wireless data traffic, which involves establishing radio links partially (I2O, O2I) or wholly (I2I) within indoor environments. This happens when either the base station or the user equipment (UE) or both are located inside buildings. According to market research [6], 50% of calls and 70% of data services will involve indoor traffic in the coming years. The increasing popularity of smart phones, tablets and other small personal wireless devices serve as testaments to this trend. The existing macro-cellular network was designed primarily for outdoor traffic, and whilst each macrocell can provide a large coverage area, their capacity, i.e., the maximum volume of traffic they can serve at one time, is limited. By spreading this limited capacity over a large area, the volume of service each sector receives is further reduced. This is fine for voice traffic, which uses much lower volumes of data than the more recent advents of wireless communication such as video calls and web browsing. However as Figure 1-4 shows, in a period of just 7 years from 2008 to 2015, the percentage of voice

traffic will drop staggeringly from over 50% to 5%, to be replaced by video, web and other high volume applications. This will create a substantial shortage in capacity which is further compounded by the increasing need for better indoor coverage. Macrocells are not efficient at providing indoor coverage, as indoor wireless signals experience attenuation through the walls and ceilings resulting in weaker signal strength, yet the volume of indoor wireless traffic continues to grow at an unrelenting pace rendering the coverage provided by existing macrocells insufficient. Worse still, building additional macrocells to improve indoor coverage is not cost effective and becomes increasingly prohibitive as the demand grows.

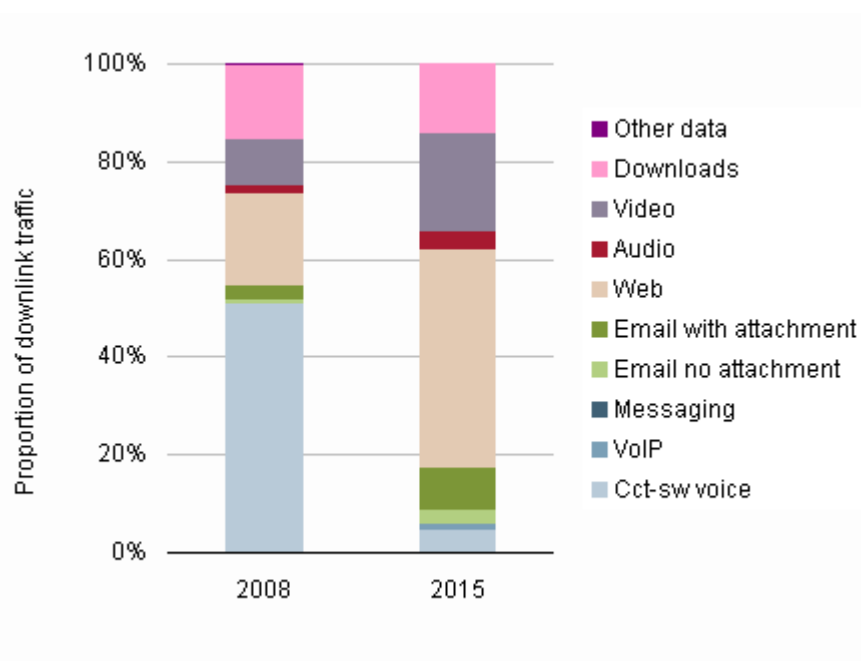


Figure 1-4: Service proportions of downlink wireless network traffic in developed regions

Two key concepts, Small cells and HetNets, have emerged and evolved in recent years in the efforts to meet the rapidly increasing demand for indoor coverage and capacity. Like pieces of a jigsaw puzzle, these concepts naturally fit around each other and, when combined, offer a well-rounded solution in many aspects such as cost, ease of implementation, technical challenges and scalability.

### 1.2.2 Small Cells

Small cells are low powered base stations with a coverage range of 10 to 2000 meters, in contrast to the macrocells which usually range over 10 kilometres. With mobile operators having to support ever growing mobile data traffic, and in particular indoor traffic, many are taking advantage of mobile offloading as a more efficient use of the radio spectrum. Small cells can readily provide data offloading as they can be easily backhauled through broadband internet such as DSL or Cable. The concept of small cells is applicable to all standards, including GSM, CDMA2000, WCDMA, TD-SCDMA, WiMAX and LTE/LTE-Advanced. In particular, for LTE-Advanced, many mobile network operators see small cells as the key to managing the spectrum more efficiently than existing macrocells [7]. Annual unit shipments of small cells are expected to reach 70 million worldwide by the end of 2017 [6].

The term small cell encompasses femtocells, picocells and microcells, listed in order of increasing base station power. Femtocell has the smallest coverage range which is in the orders of 10 meters. Consequently, they are typically designed for use in homes and installed inside buildings. This naturally allows them to provide better coverage and higher capacity when there is no existing signal or poor macrocell coverage, such as in attenuated buildings or cell edges. Their low unit production cost and strategic placing allows them to be much more cost effective at reaching this goal than macrocells, which is further improved as femtocells have self-organising and management capabilities meaning they can be installed and activated with little or no central planning. Picocells (range < 200m) and microcells (range < 2km) are similar in concept to femtocells except they operate on a greater scale. They are strategically placed to increase service provision to hotspots in the network but differ from femtocells in some aspects such as not always having self-organising capabilities and thus require more central planning. Another difference

is that they are not always installed indoors like femtocells, whilst some of them might be located inside shopping malls and airports; others are placed on outdoor towers like macrocells.

### 1.2.3 Heterogeneous Networks and Interference

Whilst small cells can provide good quality of service in their individual areas of coverage, there exist the need to integrate them into the overall network so that long distance communication links can be established; this is where *Heterogeneous Networks* (HetNet) come in. HetNet refers to the inter-operation of existing networks with different access technologies such as cellular, WLAN, and fixed broadband. HetNet provides a service by combining these network elements together, along with the capability to handover between the various network elements [8]. For example, the integration of small cells into the macrocellular network would result in a HetNet, seen figure 1.5.

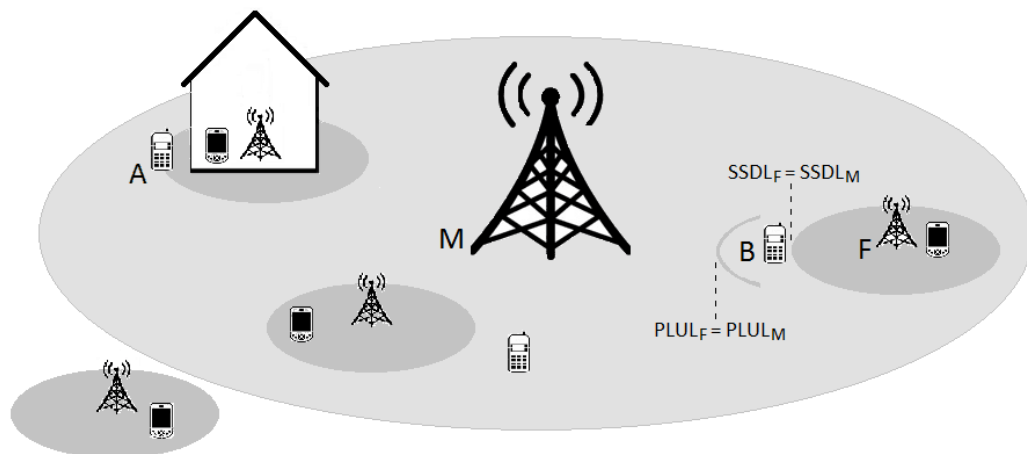


Figure 1-5: Heterogeneous Cellular Network and some of the associated challenges

However, the process of integration is not without obstacles or compromises. One of the key compromises in large scale implementations of small cells is the spectrum sharing between the small cells and their encompassing macrocells, which result in two-tiered networks. Reusing the spectrum is a consequence of the limited and scarce nature of the frequency bands available for wireless communication. While this approach allows both layers of cells to operate within the same frequency bands, the signal quality is compromised from *Cross-Tier Interference* between macrocells and small cells. For example, a femtocell located in a house close to a street would radiate its signals into the street, which could jam the downlink signal of nearby *User Equipment* (UE) on the street, since both the femtocell and the macrocells are operating within the same frequency band, see UE A in figure 1.5. This problem is especially severe close to cell edges where the macrocell signal can degrade significantly.

Another challenge of HetNet is the complexity related to cell service areas especially in cell edge scenarios. In networks that maximizes the utilisation of the licensed bandwidth by employing a frequent reuse of one, e.g. LTE, the UE normally camps on the cell with the highest *Downlink Signal Strength* (SSDL), hence the point of handover between two cells is where the UE experience equal SSDL from both cells. In homogenous networks, the point of equal SSDL between two macrocells typically coincides with the point of equal *Uplink Path Loss* (PLUL) between the macrocells. However, in HetNet the points of equal SSDL and PLUL will not necessarily be the same between cells of different power output. This is illustrated in figure 1.5, where UE B is served by macrocell M rather than femtocell F because  $SSDL_M > SSDL_F$ , however, the uplink path loss from B to M is actually larger of the two cells.

### 1.3 The need for Propagation Models

As discussed in the previous section, the increasing number bandwidth intensive mobile data services and data subscribers have placed a great challenge on network planners to meet the coverage and capacity requirements whilst using limited radio resources. Operators are meeting this challenge in a variety of ways, including utilising higher frequency spectrum, developing multiple and smart antennas, and implementing more efficient modulation coding schemes. However, these measures alone are not enough in densely populated urban areas and at cell edges. Operators are increasingly integrating small cells into their macrocellular networks to spread traffic loads, increasing capacity, and maintaining quality of service whilst reusing the same spectrum. The continued integration of small cells results in the emergence of HetNet and brings with it a set of challenges, such as *Co-tier Interference* between neighbouring small cells, which require accurate calculations of signal properties such as signal strength and path loss.

Other differences between traditional homogenous macro-cellular networks and HetNet which affect the propagation environment include greater number of base stations, reduced antenna heights, and higher concentration of obstacles. The effect of these factors has not yet been comprehensively studied, thus investigations into the channel characteristics and development of accurate and computationally efficient propagation models for HetNet becomes prerequisites to potential resolutions to the challenges posed by HetNet. The availability of such models and related simulation tools are essential for the successful operation of NetNet, as they are required for interference mitigation, network planning, coverage patterns prediction, spectrum allocation and more.

A wide variety of propagation models for different wireless services are known. Many are adapted to address the specific and varying challenges associated with different operating frequency and propagation environment. The cost of this over specialisation is that every time a new wireless system comes along with a new operating frequency or environment, new propagations models are needed, as old models simply do not achieve the desired accuracy. The push towards indoor traffic and GHz bandwidth discussed in the previous section introduces both new frequency and environment, making the need for new propagation models greater than ever. There is no end in sight for the foreseeable future in the ever increasing growth of wireless systems thus propagation models will be constantly in demand to better characterise the new environments and to improve the efficiency at using the already congested wireless spectrum. This provides the research motivation for this work, to study the characteristics of the newly emerged propagation environment with the ultimate goal of providing a new propagation model for the challenges ahead.



## 1.4 Aim and Objectives of this Thesis

The aim of this thesis is to study the properties of wireless propagation in newly emerged environments where the behaviour and characteristics of the wireless channel have not been fully understood, the environment in question mainly relates to small cells which entail buildings and scenarios such as indoor, indoor-to-outdoor, and building-to-building propagation.

The investigation will look into aspects including propagation environment, path loss, signal strength, frequency, amplitude, phase, delay spread, coherence bandwidth, angular spread, distribution statistics, multiple-input-multiple-output antenna (MIMO) channels, antenna orientation, antenna polarisation and more in order to see the whole picture and reveal the inner workings, patterns, and relationships between the various components. The ultimate goal of is to develop a comprehensive system of prediction for wireless propagation in the small cell environment, including a propagation model, channel parameters and statistics and effects relating to various elements.

### ***Objectives***

The main objectives of this thesis can be summarised as follows:

- 1. To conduct a literature review on the current and state-of-the-art approaches to modelling and characterising the propagation channel associated with small cells.**

By over-viewing the existing propagation models and discussing their capability to predict the propagation characteristics to the level of accuracy required within a reasonable time, a better understanding is garnered about the challenges and requirements imposed by the small cells environment. By identifying the merits

and potentials of the existing models, opportunities for adaptations and improvements are presented.

- 2. To develop an accurate propagation model that is suitable for the small cells scenarios including indoor, indoor-to-outdoor, and indoor-outdoor-indoor; and to validated the model through comparative study.**

An accurate model greatly helps in network planning, coverage prediction, spectrum efficiency and many other tasks. It would be an invaluable tool for in-depth studies on issues such as interference mitigation, which will lead to better understanding and solutions.

- 3. To characterised the small cells wireless channel by analysing channel parameters with respect to delay, frequency, polarisation and antenna orientation. To compare individual parameters in different environments including I2I, I2O and IOI.**

Looking at the various parameters will allow a better understanding of the complete picture. Knowledge on Inner workings of a parameter gained allows for better manipulation of it toward the overall goal. Patterns revealed allows for their predictable nature to be exploited and arrive at better solution in expected ways.

## 1.5 Contributions of this Thesis

The main contributions of this thesis can be summarised as follows:

1. A new empirical path loss prediction model for small cell environments is proposed, with different parameters for individual scenarios including I2I, I2O and IOI. The model produces accurate results for small cell environments and has been validated through a second set of measurement data. The model can be quickly implemented for system level simulations without requiring complex equipment or computation. Furthermore, a comparative study between two datasets collected from Lund, Sweden and Luton, UK is made which enhances the characterisation of small cells wireless channel and provides validation for the model.
2. Characterisation of the small cells wireless channel through extraction and analysis of key channel parameters. Statistical descriptions of these important channel parameters including RMS delay spread, coherence bandwidth and RMS angular spread was determined for both I2I and I2O scenarios and a comparative study was carried out. Knowledge of the parameter will help towards the design of more efficient wireless communication systems, resulting in better characterisation and understanding of the wireless channel in the small cells environment.
3. A new data-oriented perspective was employed to analyse the distribution and correlation of sub-channel signal power and phase for dual-polarised MIMO system. The analysis was carried out for individual polarisation settings which demonstrated significant, yet consistent differences between the polarisation settings across with an average cross polar discrimination of 3dB across all measurement scenarios. It is shown that sub-channel power and correlation

varies differently with respect to frequency for co-polar and cross-polar settings. Based on these results, a novel MIMO polarisation diversity combination scheme is proposed which takes advantage of the variations of signal strength and correlation in differently polarised channels. The scheme was tested against the data collected and results show a mean diversity gain of 10.6dB, with cross-polarised channels achieving 12.2dB.

4. Designed and implemented a comprehensive channel measurement campaign in the typical small cell scenarios. Data was measured in three types of small cell scenarios, including I2I, I2O and IOI, and features dual-polarised MIMO antenna arrays. The channel transfer matrix at each measurement position consisted of a 4-dimensional matrix array of size  $10 \times 81 \times 128 \times 32 = 3317760$  complex values, which captured full information on amplitude, phase, frequency, delay, polarisation and antenna orientation. The considerable scope of the data provides a valuable resource which can be explored in many different ways and provides an ideal platform for future research.

## CHAPTER 2

### PROPAGATION PREDICTION MODELS

*This chapter describes the principles of the radio propagation mechanism and gives an overview of existing propagation prediction models - categorised by their principle and operating environment. In particular, attention is focused on propagation models for small cells and the indoor environment.*

## 2.1 Background and General Considerations

Propagation models seek to describe the transformation a radio signal experiences as it travels from source to destination. This allows for useful predictions on the characteristics of the signal at the receiver. One of the most significant parameter that needs to be predicated is the path loss, an accurate value of path loss enables swift and accurate determination of many key values such as: signal coverage, received signal strength, signal to noise ratio (SNR), and carrier to interference ratio (C/I). Predicting the path loss accurately is a complex task due to the multitude of factors involved in a wireless radio link, including:

- Antenna properties:  
e.g. orientation, polarisation, radiation pattern, multiplicity.
- Signal properties:  
e.g. carrier frequency, amplitude, phase, modulation.
- Spatial variables:  
e.g. height, distance, topology, material, obstacles.
- Temporal variables:  
e.g. mobility, traffic volume, weather conditions.

Many of these factors are random in nature and difficult to predict, and the overall effect often results in variations of the receiver performance due to interference and fading. Evaluation of efforts to mitigate these problems depends heavily on the accuracy of prediction that can be obtained for path loss.

The locations of the base stations and mobile stations are the two greatest influences on the path loss of radio links. In traditional homogenous macro-cellular

networks, the radio link formed from a tower serving an outdoor UE is characterised by outdoor propagation. Due to the great macrocell height and outdoor antennas, the propagation is mostly line of sight. The density of obstacles and reflectors are low which in turn reduces random variations of signal strength caused by phenomenon such as diffraction and penetration. Thus, the demand for accuracy in this scenario is relatively low and many existing path loss models are sufficient.

In HetNet the base station and mobile station can be situated indoors which create new propagation scenarios such as I2I, I2O, O2I and IOI. These scenarios can involve non line-of-sight propagation, attenuation through buildings, lower antenna heights, and greater concentration of obstacles, all of which add to the difficulty of predicting the path loss accurately. As HetNet is an emergent phenomenon, existing path loss models are not tailored to the HetNet propagation environment, which happens to be more complex than those of existing infrastructures, thus the demand for accuracy is greater. On the other hand, the potential benefits of small cells is promising in many ways that if a sufficiently accurate path loss model can be developed to overcome the issue of interference, all of these benefits can be harnessed. This provides the main motivation behind the research presented in this thesis.

The prediction from propagation models is used in key processes like interference mitigation, coverage planning and multipath calculations, which forms the basis of the high level network planning process. With each new system, the network planning process differs slightly and between generations of systems, the difference can be great. For example, the network planning process for 3G systems such as UMTS are fundamentally different to 2G systems such as GSM [9], and for 4G systems the processes are different again. As a result, the propagation prediction models crucial to the network planning process need to be adapted to changes in the process, or new models must be constructed to take their place.

The environments where wireless communication systems are installed ranges from wide open rural areas to densely built urban centres, as well as indoor environments. This means different propagation prediction models are required to cover the whole range of scenarios from macrocells to femtocells, from outdoors to indoors. The attenuation a radio wave experiences can be described by propagation mechanisms such as reflection, diffraction, penetration and scattering. While the underlying principles of the mechanisms are not dependent on the environment considered, their contribution to the overall attenuation are. For example, signals from an urban macrocell to a receiver on the street are mainly affected by rooftop diffractions, whereas the predominant mechanism behind outdoor microcells transmitting to indoor mobile stations is wall penetration.

Considering all the existing radio propagation mechanisms, the decision to focus on which ones and in how much detail depends on what we are interested in modelling, be it signal strength, delay spread, fading statistic, or any other characteristics. Once a scenario of study is established, whatever prevailing mechanisms that may exists must be identified and investigated; whilst a mathematical description the propagation phenomena resulting from the mechanisms acting on the environment must be found. Steps required in this process include:

- Converting the analogue terrain into digital terrain data.
- Defining mathematical approximations for the physical propagation mechanisms.
- Coalescing the data and information gathered into a model.

Propagation models are generally more efficient when only the dominant phenomena are taken into account; however the nature of mobile radio environment provides a number of challenges to the investigation of propagation phenomena:



- The distances between the base station and the mobiles vary greatly, ranging from few metres to several kilometres.
- The height of the antenna varies from below the rooftop of residential houses to towering above multi storey buildings.
- The size of natural and man-made objects in the environment ranges from smaller than a wavelength to many orders of wavelengths, each having an effect on propagation.
- The description of the environment is usually not available in much detail.

Solutions to overcoming these challenges come from two main approaches:

### ***Experimental Approach***

Experimental solutions produce a class of propagation models known as *Empirical Models* which are based on measurements in the real world, thus they give a closer representations to reality. However, these models are limited by the environment from where the data is collected which results in weaker control over the environment and less generalised models.

### ***Theoretical Approach***

Theoretical investigations generally involve software simulation or analytical studies and consider not reality itself but simplified models of reality. Nevertheless, simplifications often allow the environments to be more easily described and modified giving this approach more control over its environment. The types of model associated with this approach include *Deterministic Models* and *Statistical Models*.

Together, deterministic models, statistical models, and empirical models make up the main categories of propagation models. The key difference between them is that statistical models are *Small-scale propagation models* where as the other two

types are *Large-scale propagation models*. The meaning of the terms in italics their implications will be discussed in the following subsection.

### 2.1.1 Small Scale Propagation Models

*Small-scale propagation models*, also known as *Statistical Channel Models* or *Fading Models*, are based on probability theory. The signal is modelled over short distances on the order of wavelengths. Fading is the term used to describe the phenomenon of large, and apparent random deviations in channel attenuation properties over small changes in frequency, position or time. A channel that experiences fading over time is known as time-selective fading channel, for example, in *Fast Fading*, the receiver experiences significant deviations in signal strength over short periods of time despite of constant frequency, in contrast to *Slow Fading*, where changes in the magnitude and phase imposed by the channel can be considered roughly constant over the symbol duration.

Similarly, a channel that experiences fading over frequency can be separated into *Flat Fading* and *Frequency Selective Fading*, the latter is caused by partial cancellation of a signal with itself in multipath propagation. As its name suggests, in frequency selective fading the magnitude of fading varies with the carrier frequency, whereas in flat fading all frequency components experiences the same degree of fading. The coherence bandwidth, measures the maximum separation of in frequency in which two frequency components of a signal experiences correlated fading. In flat fading, the coherence bandwidth of the channel is larger than the bandwidth of the signal, where as in frequency selective fading the coherence bandwidth of the channel is smaller than the bandwidth of the signal, thus different frequency components will experience uncorrelated fading.

Fading is a frequent occurrence in wireless communication and is due to either multipath or shadowing. Multipath results from the presence of scatterers in the

propagation environment creating multiple paths that a signal can potentially follow. As a result, the Rx sees the superposition of multiple copies of the signal, each traversing a different path. The signals will in turn experience differences in attenuation and arrive at Rx with different power, delay and phase shift, resulting in constructive or destructive interference. Strong destructive interference will cause a sharp drop in the channel signal to noise ratio and could sever the communication link completely. Shadowing occurs when large bodies temporarily obstruct the path of the signal, which can have a random effect on the channel characteristics due to the nondeterministic nature of the position, velocity and geometry of the obstructing body.

In statistical models, by modelling the fading as a Gaussian processes, a probability distribution that represents the channel impulse response is obtained. The probability density function of the random variable described by the distribution is then used to simulate the amplitude and phase information of the radio waves passing through the channel. Prominent fading channel models includes: Log-normal [10], Rayleigh [11], Rice [12], Nakagami [13], Weibull [14] and Loo [15]. These models are generally adapted for rural and macro-urban environments of varying circumstances. For example Rician fading is suited for open areas where there is a dominant line of sight, whereas Rayleigh fading works best for more densely built up areas where there are many scatterers and no dominant line of sight.

### **2.1.2 Large Scale Propagation Models**

*Large-scale propagation models* aim to model the signal propagation over large distances, usually to work out a value for the average signal strength at the receiver. As mentioned in the previous section, this prediction can be used to compute the values of SNR and C/I which are the cornerstones of the wireless

network planning process. The validity of the predications from these models is usually verified through measurements in field.

*Large-scale propagation models* can be roughly divided into deterministic models and empirical models. A finer division allows for semi-deterministic models, semi-empirical models, and hybrid models in addition to the previously types, this results in a spectrum of propagation models. On one extreme is empirical models, the spectrum then shift along toward semi-empirical models, then toward semi-deterministic models and finally to Deterministic model at the other extreme.

Empirical models are based purely on experimental data and do not purposely try to consider or calculate factors such as obstacle influence; such influences are simply included in the data as part of the measurement, albeit with randomising effects. Despite this lack of consideration, the fact many empirical models have been successfully adapted to various scenarios makes them fine advocates of the experimental approach paradigm motioned in the previous section.

Deterministic models are the exact opposite, all details and considered in advance with the influences of various factor and mechanism are included with the help of theoretical formulations. They are a shining example of the theoretical approach paradigm discussed in section 2.1. Due to the multitude of different types large scale models in the spectrum, the whole of the next section will be devoted to describing and evaluating each of them in detail.

## 2.2 Overview of Propagation Models

This section provides an overview and comparison between the main types of large scale propagation models, which include deterministic, empirical, semi-deterministic, semi-empirical, and hybrid model.

### 2.2.1 Deterministic Models

Mathematically speaking deterministic models, as their name suggest, refer to the models that, given the same input, produce the same output every time with no random variations in the result. In the context of propagation modelling, the phrase usually refers to computational algorithms that simulate the wave propagation by converting environmental information into signal strength. They are generally more accurate than the rest but suffer from low computational speed. Deterministic models work with the theoretical principles of the wave propagation phenomena and thus can be applied, in theory, to all environments without affecting the accuracy. In practice, their implementation requires large databases of parameters relating to the properties of the objects in the environment, such as the refractive index, which are often impractical to obtain. Moreover, the numerical algorithms employed in these models are often exponential or higher in complexity, making it prohibitively time consuming to archive both the required accuracy and coverage area.

Acceleration techniques do exist and range from theoretical simplifications such as *Universal Theory of Diffraction* (UTD) to physical hardware like the *Graphic Processing Units* (GPU). These improvements have achieved varying degrees of success although the simulation times for typical scenarios remains impractically high. Nevertheless, by virtual of having their basis in numerical algorithms, the potential is there for ever increasing speeds with the introduction of new software

and hardware. One aspect worth mentioning is that unlike empirical models, deterministic models are not reliant on the availability of measurement data from the target environment. This provides the models a greater degree of freedom, which can result in better generalisation, i.e. better suited for a wider range of environments. Furthermore, their basis in Physics can prove useful for the characterisation and understanding of physical phenomena found within the wireless channel. There are many ways of constructing deterministic models, these can roughly be categorised into two main approaches:

### ***Electromagnetic Wave Based Simulation***

This involves solving Maxwell's equations or some other wave equation with certain boundary conditions, usually through iterative calculation and update of the electric and magnetic field values over the entire domain.

### ***Ray Based Methods***

By simplifying the wave propagation problem and viewing radio wave as rays similar to light rays, geometric calculations on propagation phenomenon such as reflection, refraction and diffraction can be performed.

### ***Wave Based Simulation***

In this approach, the mechanisms behind the propagation of electromagnetic wave can be investigated from either a pure theoretical point of view or from computations based on full-wave formulations. Conceptually, this approach can be likened to performing virtual measurements as it involves computation of field strengths at individual points across the domain. As a bonus, the simulated measurements have the advantage of providing much better control over the environments. As with real measurements however, all propagation mechanism are mixed into the results and extracting the various physical phenomena and their relative contributions from the simulation requires further analysis. Methods

using this approach include *Transmission Line Matrix* (TLM) [16, 17] and *Finite-Difference Time-Domain* (FDTD) [18, 19]. FDTD, which works by numerically solving Maxwell's equations in the time domain, can achieve great accuracy in indoor environments. The process goes as briefly as follows:

1. The time dependent Maxwell's equations in its partial differential form are converted into finite-difference equations using central-difference approximations.
2. The resulting equations are then solved in either software or hardware in a leapfrog manner:
  - a) Solve the electric field vector components at a given instant in time.
  - b) Solve the magnetic field vector components at the next instant in time.
  - c) Repeat A and B until both field behaviours are fully evolved.

By the virtue of being a time-domain method, a single simulation run of FDTD can cover a wide range of frequencies. However, because the algorithm works by solving electromagnetic flows, it has to constantly expand along all 3 dimensions until it covers the whole domain. Therefore memory requirement increases rapidly with the transmitting distance. This has limited the algorithm's application to such an extent that it is currently almost exclusively used in its 2D form. This compromise is based on the rational that in some scenarios, such as an open environment, the third dimension (height) contributes less significantly. Even with the reduced workload, the 2D algorithm is still restricted by scenario size. However many research efforts, e.g. Valcarce-Rial [20], are focused on increasing its scope. The full 3D algorithm would be many times more accurate but it is current limited to very small scenarios such as small rooms, though recent advances in GPU and early results from their experimentation do show some promise of gains, and has led to a number of work on this subject [21, 22, 23].

***Ray Based Methods***

As with all theoretical approaches, assumptions lead to substantial simplifications of the problem. Considering the propagation of radio waves, some simplifications can be obtained by assuming high frequency small wavelengths. This leads to viewing radio waves as rays similar to light. Under this assumption, the waves only interact with the environment through the mechanisms of reflection, refraction, diffraction, absorption, and scattering. These are concepts *Geometrical Optics* and their effects can be determined through geometrical calculations. A consequence of this is that the different propagation phenomenon will be clearly distinguished each having their own mathematical and physical description. This sets it apart from empirical and wave simulation methods. At a larger scale, several rays can be viewed as a single ray; the density of rays will be a determining factor for both the speed and accuracy of the algorithm.

Ray optical methods have been commonly adopted especially in urban microcell modelling with typical coverage range of 0.2 to 2km, example of such methods include *Ray Tracing* [24] and *Ray Launching* [25], which differs in the direction the ray is followed. In general, ray methods works by considering a number of rays between the Tx and Rx before calculating the path loss along each ray, the final result is obtained by simply combing the values on all of the rays. Ray optical methods are generally faster than wave simulation methods, however, as with all numerical methods there is a trade-off between speed and accuracy depending on the level of refinement specified by the input parameters. In environments of more obstacles, both the number of rays and the number of interactions each ray has with the environment increases. When combined, these two factors rapidly inflate the computational workload. At the femtocell level, with typical transmission range in the order of 10 meters, ray based algorithms are forced to make an unworkable compromise between speed and accuracy. However, as with all numerical algorithms there are many aspects in which they can be improved



upon, for example, Beam Tracing [26], which launches multiple rays at the same time, and Intelligent Ray Launching Algorithm developed by Lai et al [27], which have been demonstrated to archive reasonable speed and accuracy for the Outdoor-to-Indoor channel.

### **2.2.2 Semi-deterministic Models**

Semi-deterministic models are similar to deterministic models in many ways; most of the main environmental factors are included in the formulation. However they do contain elements of experimentation and parameters obtained empirically through trial and error, the values of which they do not attempt to prove or justify. The model most widely associated with semi-deterministic models is the COST-231 Walfisch-Ikegami model [28], which considers factors such as street width and building heights.

#### ***COST-231 Walfisch-Ikegami Model***

This path loss model is an enhancement by the COST 231 project based on a combination of the empirical models of Walfisch [29] and Ikegami [30]. The model considers the buildings in the vertical plane between the transmitter and the receiver. Street widths, buildings heights as well as transmitter and receiver heights are considered. The accuracy of this empirical model is quite high because in urban environments the propagation in the vertical plane and over the rooftops (multiple diffractions) is dominating, especially if the transmitters are mounted above roof top levels. If the wave guiding effects due to multiple reflections in streets are dominating, the accuracy of the COST Walfisch-Ikegami model is limited, as it is focused on the multiple diffractions in the vertical plane. The COST Walfisch-Ikegami model calculates the path loss of LOS and NLOS separately. For LOS conditions, the formulation is as follows:

$$L_{LOS} = 42.6 + 26 \log_{10} d + 20 \log_{10} f$$

Where

$d$  is distance in km,  $d > 0.02\text{km}$

$f$  is the transmit frequency in MHz

For NLOS condition, the calculation is conditioned on 2 different scenarios: waves the go through rooftop diffractions and waves below rooftops:

$$L_{NLOS} = \begin{cases} L_0 + L_{rts} + L_{msd} & L_{rts} + L_{msd} > 0 \\ L_0 & L_{rts} + L_{msd} \leq 0 \end{cases} \quad (2.1)$$

where

$L_0$  is the free space path loss

$L_{rts}$  is the multi-screen path loss

$L_{msd}$  is the rooftop path loss

$L_0$ , the free space path loss from equation (2.1) is calculated as:

$$L_0 = 32.45 + 20 \log_{10} d + 20 \log_{10} f$$

$L_{rts}$ , the roof top path loss from equation (2.1) is calculated as:

$$L_{rts} = -16.9 - 10 \log_{10} w + 10 \log_{10} f + 20 \log_{10}(\Delta h_{mobile}) + L_{ori}$$

$w$  is street width in km

$$\Delta h_{mobile} = h_{roof} - h_{mobile}$$

The value of  $L_{ori}$  depends on the angle of incidence  $\varphi$  with respect to the ground at the mobile station:

$$L_{ori} = \begin{cases} -10 + 0.354\varphi & 0^\circ \leq \varphi < 35^\circ \\ 2.5 + 0.075(\varphi - 35) & 35^\circ \leq \varphi < 55^\circ \\ 4.0 - 0.114(\varphi - 55) & 55^\circ \leq \varphi \leq 90^\circ \end{cases}$$

$L_{msd}$ , the free multi screen path loss from equation (2.1) is calculated as:

$$L_{msd} = L_{bsh} + k_a + k_d \log_{10} d + k_f \log_{10} f - 9 \log_{10} b$$

where

$$L_{bsh} = \begin{cases} -18 \log_{10}(1 + \Delta base) & h_{base} > h_{roof} \\ 0 & h_{base} \leq h_{roof} \end{cases}$$

$$\Delta h_{base} = h_{base} - h_{roof}$$

$$k_a = \begin{cases} 54 & h_{base} > h_{roof} \\ 54 - 0.8\Delta base & h_{base} \leq h_{roof} \text{ and } d \geq 0.5km \\ 54 - 0.8\Delta base \frac{d}{0.5} & h_{base} \leq h_{roof} \text{ and } d < 0.5km \end{cases}$$

$$k_d = \begin{cases} 18 & h_{base} > h_{roof} \\ 18 - 15 \frac{h_{base}}{h_{roof}} & h_{base} \leq h_{roof} \end{cases}$$

$$k_f = \begin{cases} 0.7(\frac{f}{925} - 1) & \text{for medium size city and suburb} \\ 1.5(\frac{f}{925} - 1) & \text{for metroplian centres} \end{cases}$$

As can be seen from the above formulations, the model takes into account many different environmental factors, such as the building height, street width, gap between buildings, height difference between antennas, but there are also a fair number of arbitrary looking figures plugged into the equations, this is precisely the characteristic of semi-deterministic propagation models.

### 2.2.3 Semi-empirical Models

Semi-empirical models are largely based on experimental data but additional environmental information is considered, although not as much as semi-deterministic models. The most quoted examples of semi-deterministic model are the Motley Keenan [31] and the COST231 Multiwall [28] models.

#### ***Motley Keenan Model***

The Motley Keenan Model is empirically obtained path loss model that takes into account the penetration loss from walls. However, unlike deterministic models, it does not consider the effects from mechanism such as reflection, diffraction scattering. It was designed to predict the path loss in indoor environments which explain the special treatment of walls, and because of this, it does not give satisfactory results when used outdoors [32].

In general, the Motley Keenan Model provides a higher accuracy than pure empirical models such as the Hata Model described in the next section. However, the model is prone to overcompensation for the attenuation through walls and obtains results that are too pessimistic. Mathematically, the model can be expressed:

$$L = 20 \log_{10} \frac{4\pi f}{c} + 20 \log_{10} d + nA_W$$

where

$d$  is Transmitter-Receiver separation distance (m)

$n$  is the Number of walls between transmitter and receiver

$A_W$  is the Wall Attenuation Factor (dB)

Enhanced version of the model can also be found in the literature, works by Cheung [33], Lima [34], Aragon-Zavala [35] and Solahuddin [36] have made various improvements upon the Motley Keenan model but the underlying approach has remained the same.

### ***COST231 Multiwall Model***

As mentioned just above, this model is an improvement over the Motley Keenan Model. In addition to including parameters to model the walls loss, the multiwall model also considers floor loss, as well as the type of material of each obstruction. The model is formulated as follows:

$$L = L_1 + 20 \log_{10} d + L_W + L_F$$

where

$L_1$	is the free space path loss 1m from the transmitter (dB)
$d$	is the Transmitter-Receiver separation distance (m)
$L_W = \sum_{i=1}^n a_{w_i} k_{w_i}$	is the total loss from walls
$L_F = a_f k_f$	is the total loss from floors
$n$	is the total number of different types of walls
$a_{w_i}$	is the penetration loss through a single wall of type $i$ (dB)
$k_{w_i}$	is the number of walls of type $i$
$a_f$	is the transmission loss through 1 floor (dB)
$k_f$	is the number of floors

The COST231 multiwall models is generally more accurate than similar empirical models that do not consider wall loss, and can be optimised by fine tuning wall

and floor loss factors by collecting data from experiments. However, like the Motley Keenan Model, it tends to be too pessimistic, it also does not account for the scenarios where signals can go around a wall rather than through it. Overall, the multiwall model is most often used in indoor environments.

#### **2.2.4 Empirical Models**

Empirical models are obtained through direct measurement of physical parameters, such as signal strength and impulse response, using dedicated equipment. Due to the nature of measurements, all environmental influences are implicitly recorded regardless of whether they can be separately recognised. The data collected are post processed and models arise from trends in the data. Empirical models are in general more site-specific than deterministic models, as the data used to derive these models are obtained from individual locations. However, because studies tend to focus on specialised scenarios, the site specific nature of empirical models can often be turned into an advantage. What really stands out for empirical models is their execution speed; whereas deterministic models are mostly computationally intensive, empirical models often involve only a few calculations. Thus they can be applied quickly without needing much computing power

With proper considerations with regard to the scenario of study, an empirical model can make highly accurate predictions. As efforts can be focused on obtaining measurement data exclusively from small cell environments, the empirical approach is certainly viable. With proper care and consideration given to the scenario and measurement process, any data collected would prove very useful in formulating a path loss model and provide insights into the wireless channel behaviour in small cell environments.

**COST-231 Hata**

The COST-231 Hata model [28] is derived from the Okumura model [37] which was originally developed in the 1960's using data collected from large scale studies conducted in and around Tokyo. It works within the ranges of

- frequency: 150 – 1920 MHz
- base station antenna height: 30 – 1000m
- station antenna height: 1 – 10m
- link distance: 1 – 100km

The model is formally expressed as:

$$L = PL_f + A(f, d) - G(h_{Tx}) - G(h_{Rx}) - G(f, tr)$$

Where:

$$PL_f = 20 \log \left( \frac{4\pi df}{c} \right) \quad \text{is free space path loss in dB}$$

$$G(h_{Tx}) = 20 \log \left( \frac{h_{Tx}}{200} \right) \quad \text{is base station antenna gain}$$

$$G(h_{Rx}) = \begin{cases} 10 \log \left( \frac{h_{Rx}}{3} \right) & h_{Rx} < 3m \\ 20 \log \left( \frac{h_{Rx}}{3} \right) & 3m < h_{Rx} < 10m \end{cases} \quad \text{is the mobile antenna gain}$$

$G(f, tr)$  is the 1<sup>st</sup> correction factor , a function of frequency and type of terrain.

$A(f, d)$  is the 2<sup>nd</sup> correction factor, a function of frequency and distance

The values of the correction factors are provided by graphical charts shown in Figure 2-1.

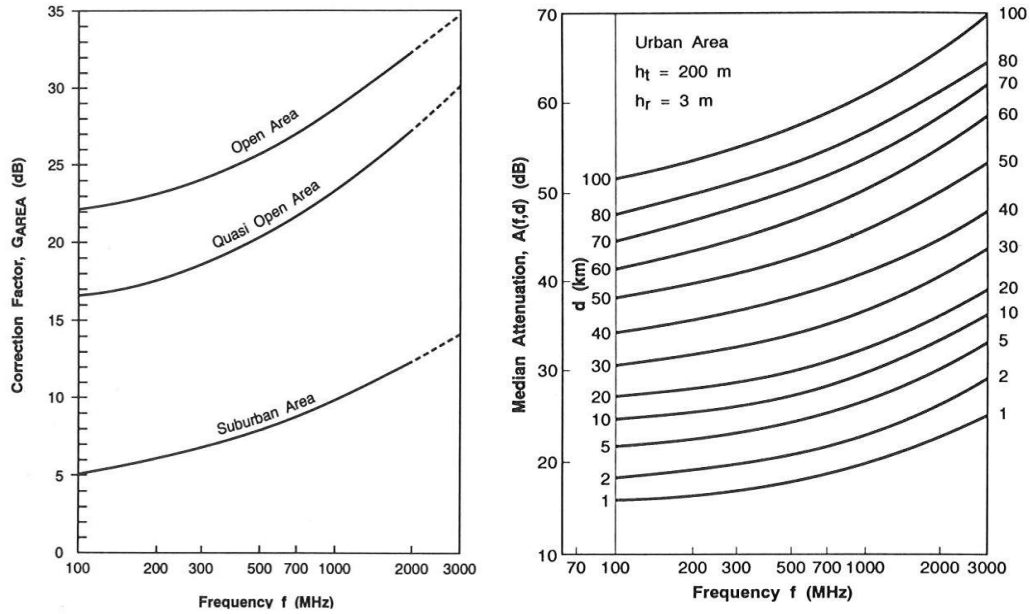


Figure 2-1: Attenuation factor for Okamura Model

The Hata model [38] is an enhancement of the Okumura model; it provides analytical expression for the correction graphs, giving it versatility. Expressions are available for urban, suburban, and rural areas. Also, a number of correction factors can be applied to extend it to any environment. The Hata model includes 3 separate parts: Urban areas, Suburban areas and Open areas. Path Loss in Urban areas is given by:

$$L_U = 69.55 + 26.16 \log f - 13.82 \log h_{Tx} - C_H + [44.9 - 6.55 \log h_{Tx}] \log d$$

Where:

- $f$  is the frequency (150 – 1500MHz)
- $d$  is the Tx - Rx separation distance (1 – 20km)
- $h_{Tx}$  is the effective base station height (30 – 200m)
- $C_H$  is the correction factor for mobile antenna height.



For small or medium sized cities:

$$C_H = 0.8 + (1.1 \log_{10} f - 0.7) h_M - 1.56 \log_{10} f$$

For large cities:

$$C_H = \begin{cases} 8.29 (\log_{10}(1.54h_M))^2 - 1.1 & , \text{ if } 150 \leq f \leq 200 \\ 3.2 (\log_{10}(11.75h_M))^2 - 4.97 & , \text{ if } 200 < f \leq 1500 \end{cases}$$

Path Loss in Suburban areas is given by:

$$L_{SU} = PL_U - 2 \left( \log \frac{f}{28} \right)^2 - 5.4$$

Path Loss in Open areas is given by:

$$L_O = PL_U - 4.78(\log f)^2 + 18.33 \log f - 40.94$$

The COST-231 Hata model further extends the Hata model to cover the 1500 – 2000MHz frequency range. The range of Tx/Rx heights and link distance are identical to the Hata. Mathematically, the model is formulated as:

$$L = 46.3 + 33.9 \log f - 13.82 \log h_{Tx} - a(h_{Rx}) \\ + [44.9 - 6.55 \log h_{Tx}] \log d + C$$

where:

$$a(h_{Rx}) = (11 \log f - 0.7)h_{Rx} - 1.56 \log f + 0.8$$

$$C = \begin{cases} 0dB & \text{for medium cities and suburban areas} \\ 3dB & \text{for metropolitan areas} \end{cases}$$

The COST Hata model is fast, but the prediction it provides is generally not good enough in urban scenarios where environment factor is important. The model work best when the transmitter is above rooftop level, since any obstructions greatly reduce its accuracy.

In this section, 3 main types of propagation models are presented and their pros and cons are discussed. The following section looks at some of the widely known models in more detail.

### **2.2.5 Hybrid Models**

Hybrids of the previously mentioned class of models can also be found in the literature [39, 40]. The term hybrid refers to combining more than one propagation model of different types in order to improve the overall propagation prediction. The general strategy behind the hybrid method is to exploit the best of each model by employing them in the scenarios where they work best or are most efficient. Because of the more strict requirement imposed by this 2 stage environment, hybrid models are mostly designed for specific application. A common scenario where hybrid methods are employed is urban outdoor-to-indoor propagation prediction. This is because the propagation environment changes considerably from outdoors to indoors so appropriate models are employed for each environment. Ray based algorithms are best suited for the urban outdoor scenario and therefore used to model the outdoor part of the propagation; the result is then fed into a wave simulation algorithm, which is more accurate for indoor prediction, to model the indoor part of the propagation. An example of a more general hybrid model is the MOTIF which combines an empirical approach such as Monte-Carlo with a deterministic approach such as FDTD and is employed for indoor modelling to grammatically increase the computation speed compared pure deterministic indoor models. Other

approaches include [41], where a 3D propagation model is proposed that combines semi-empirical models, and [42], which propose a combined model for outdoor-to-indoor prediction using intelligent ray launching for the outdoor prediction and FDTD for indoor prediction. Moreover, many papers have proposed a solution of using a less accurate but faster model for simulation and a more accurate but slower model for validation.

### **2.2.6 Summary**

This chapter detailed the mechanisms affecting the radio wave propagation and explained the concept of the wireless propagation model and related intricacies. The various propagation scenarios and their differences were described, as well as different class of models adapted to different scenarios. This chapter also looked in depth the pros and cons of the most widely used propagation organised by class, as well as the concepts behind the class themselves. Finally, requirements and challenges leading to a new model are described.

## CHAPTER 3

### EMPIRICAL PATH LOSS MODEL

*The anticipated deployment of small cell wireless technology calls for propagation models that are suited for indoor-to-outdoor and residential scenarios to facilitate network planning. This chapter presents an empirical path loss model derived directly from measurements conducted in the above mentioned scenarios. The model presented here can be used in system level simulations, as well as to serve as a comparison with other models.*

### 3.1 Introduction

With the rapid growth in the demand consumption for indoor wireless services, small base stations have emerged as a key concept to keep up with the increasing need for indoor coverage and capacity of cellular services [1]. With the scarcity of the wireless spectrum, its availability for exclusive use by small cells is greatly limited. The Co-channel deployment, where the small cells use the same spectrum as the underlying macro-network, is currently the best practical approach. By reusing the spectrum, this arrangement lead to the formation of a HetNet which introduces additional challenges to network planning and operation, the most important of which is the management of cross-tier interference between the different layers of the HetNet, i.e. interference between small cell and macrocell signals [43].

Studies on interference mitigation techniques have shown a need for the propagation models that are highly adapted to the scenario of interest [44]. For cross-tier interference, which occurs at the UE on the street level, the signal that arrives from remote macrocells has very different characteristics to that from nearby small cells. As summarised in the previous chapter, macrocells provide much larger coverage areas and are usually situated on top of towers resulting in greater transmitter height. Suitable path loss models for the Macro-to-UE scenario include: COST231-Hata [28]; ITU-R [45]; and SUI [46]. Small cells, as the name suggest, provide smaller coverage areas, and are often placed inside buildings which introduce additional indoor and I2O propagation components. The literature on indoor propagation is extensive, widely used and cited indoor models include: COST231 Multi-Wall [28]; ITU Indoor Propagation [45]; Keenan-Motley [31]; and wideband indoor channel model by Kivinen et al. [47]. Indoor-to-outdoor models, in comparison, have received relatively less attention. Several findings

have been reported in the recent years, see references [48, 49, 50, 39, 51, 52]. Previous to that the literature was very scarce.

In order to study the propagation properties of the small cell signals in HetNet data representative of the related environment is required. In this chapter, the data studied comes from measuring campaign carried out in Lund, Sweden. Details relating to the measurement campaign will be given in section 3.2, this include the specification and setup of the equipment [53], the central frequency and bandwidth of the signal, the properties of the signal, as well as descriptions about the locations from which the measurements took place.

Section 3.3 will firstly describe the procedure involved in post-processing and organising the data, then carry out in-depth analysis and finally describe the steps involved in constructing a new propagation model from the results of the data analysis.

Section 3.4 provide a validation of the model using data collected from a similar environment using different equipment. The parameters extracted from the 2<sup>nd</sup> data set is compared with the parameters from the original dataset in order to give an indication of the accuracy of the proposed model.

Section 3.5 will summarise the findings in this chapter, discuss the results and draw the conclusion.

## 3.2 Channel Measurement Campaign

### 3.2.1 Theoretical Background

In wireless communication systems, propagation of radio signals to mobile stations is subject to scattering from local objects. This is especially true in urban and indoor scenarios, where surrounding buildings prevent LOS conditions. As a result, the received signal consists of multiple copies of the transmitted signal, which are characterised by different amplitudes, phases, polarisations, and angle of arrivals. These are combined at the receiver giving rise to constructive and destructive interference, which can cause large variations in the received signal envelop.

The locations of local scatterers with respect to the mobile station are continuously changing due the movements of the mobile and objects in the surrounding environment, this can cause rapid fluctuation of the received signal level is known as fast fading. Deterministic prediction of exact field strength in multipath environment is demanding as it would require exact knowledge of all scatterers. Hence, statistical models are applied for modelling a mobile radio channel.

Radio channel can be visualised as a black box that transforms the transmitted signal  $X$  into received signal  $Y$ , similar to a linear filter. It can be modelled as a linear time-variant filter that is characterised by one of four following entities:

- The *Impulse Response*,  $h(t)$ , which describes the reaction of the channel in response to an impulse as a function of time.
- The *Transfer Function*,  $H(f)$ , which is the Fourier Transform of  $h(t)$  characterising the channel response in the frequency domain.

- The *Delay Spread*, which describes of the multipath components of the channel.
- *Doppler Spread*, which captures the time variation of the channel due to motions of the scatters or antennas or both.

The channel transfer function  $H(f)$  of the frequency domain, and its *Inverse Fourier Transform*, the impulse response  $h(t)$  of the time domain, can be determined by instruments known as Vector Channel Sounding Systems. This will allow time and frequency channel characteristics to be extracted. If MIMO and dual polarised antennas are employed, spatial and polarisation characteristics can also be determined. This section describes the configuration of such a system with customised dual-polarised MIMO antenna arrays, which are used to conduct the measurement campaign used in this thesis.

### 3.2.2 Channel measurement System

The RUSK LUND [54, 55] channel sounder, shown in Figure 3-1, was designed and manufactured by Medav GmbH for the University of LUND. It is a MIMO channel sounder built on the switched array principle and can measure up to a maximum bandwidth of 240 MHz. The Sounder can be configured to operate in the 300 MHz, 2 GHz and 5 GHz bands; this flexibility has seen it used for a wide variety of channel characterisation research, including peer-to-peer MIMO communication at 300 MHz; personal and body area networks at 2 and 5 GHz; characterization of polarization properties, sensor networks, and cellular MIMO systems at 2 and 5 GHz; and studies of multiuser MIMO systems and car-to-car communication at 5 GHz [56].



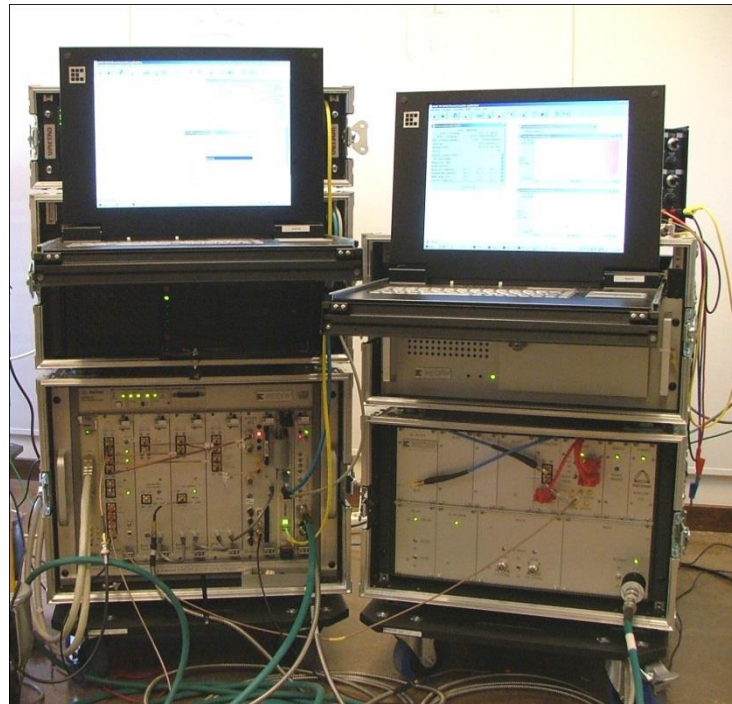


Figure 3-1: RUSK LUND Channel Sounder

### 3.2.3 Measurement set-up

The transmitting antenna (Tx) was a planar array of dual polarized patch elements. Only the middle 2 rows were used during the measurements as the elements in these rows had the same radiation patterns which were different from the elements in the top and bottom rows. This leads to 32 transmitting nodes (2 rows  $\times$  8 columns  $\times$  2 polarisations). The receiving antenna (Rx) was a cylindrical patch array with 128 receiving nodes (4 rows  $\times$  16 columns  $\times$  2 polarisations), see Figure 3-2. The Tx and Rx were placed on stands of 1.7m and 1m in height respectively.

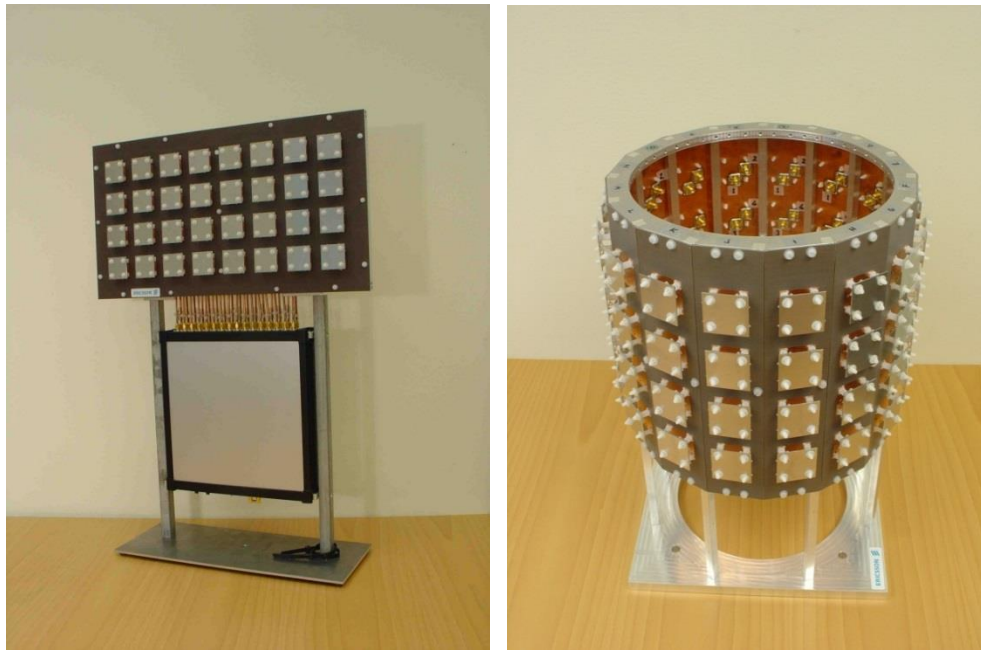


Figure 3-2: Dual polarised antenna arrays: Tx (left), Rx (right)

Measurement data was recorded with the RUSK LUND channel sounder, at a central frequency of 2.6GHz with a signal bandwidth of 50MHz. The transmit power was 40dBm in total which is made up of 27dbm Tx power and 13dB amplifier. A 20dB *Attenuator* and a 10dB *Low Noise Amplifier* (LNA) were also used at some measurement positions to ensure the received power level was within the Rx's dynamic range.

The maximum measureable delay recorded was  $1.6\mu\text{s}$ . At the receiver, the transfer function was sampled at 81 points in the frequency domain. The sampling time for one set of Multiple-Input Multiple-Output (MIMO) snapshots was 0.026s. Five consecutive snapshots form one block, with no delay between the snapshots. There was a delay of 1s between each block. During the measurements, the Tx was kept in the same location, whilst the Rx was moved to a number of measurement locations throughout the building as well as outside. Two blocks of data were recorded for indoor measurements and up to 50 blocks were measured for

outdoors. Table 3-I below gives detailed information on the setup of the RUSK channel sounder:

**Table 3-I: Measurement parameters from the measurement data file**

Central Frequency	2.60GHz
Bandwidth	50MHz
Sample Period	3.20μs
Tx power	40dBm
Snapshots per block	5
Gap	0
Trigger	'Internal time trigger'
Block Gap	1.0039s
Record Mode	'Fixed number of blocks'
Blocks	20
Sample Rate	640 MHz
Data Format	'WMT-V1'
Number of Samples	2048
Number of Channels	4128
Number of Snapshots	100

### 3.2.4 Measurement Location

The measurement campaign was designed and carried out by myself and Dr Andres Alayon Glaznov, with the help of Professor Fredrik Tufvesson, during the period of 14<sup>th</sup> – 18<sup>th</sup> June, 2010. The measurements were carried at *Faculty of Engineering, Lund University* (LTH), specifically at the E-Huset of LTH, Ole Römers väg 3, as shown in Figure 3-3.

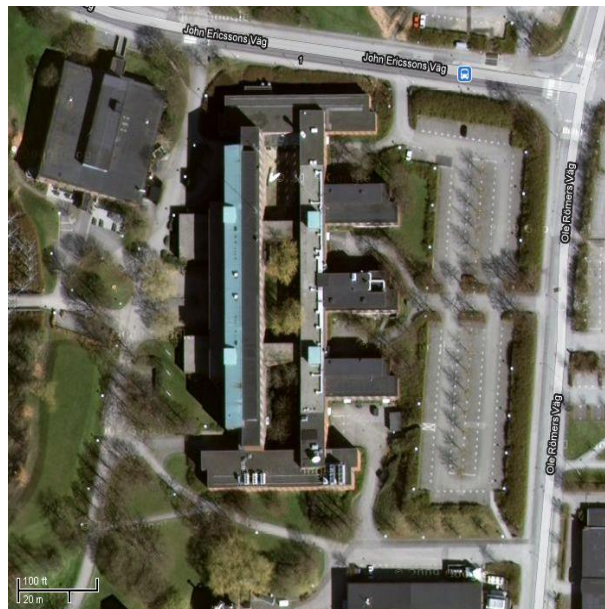


**Figure 3-3: The E-Huset building of Lund Institute of Technology and its surrounding areas**

Figure 3-4 gives an overview of the measurement positions. The dots mark the positions of the Rx, whilst the crosses mark the positions of the Tx, along with an arrow giving its array orientation. For each Rx position 4 sets of measurements were recorded, one for each of the four orientations of the Tx, hence in total there are  $123 \times 4 = 492$  sets of measurements. During the measurement, the large labs were all empty, whilst some of the small offices had people working in them.

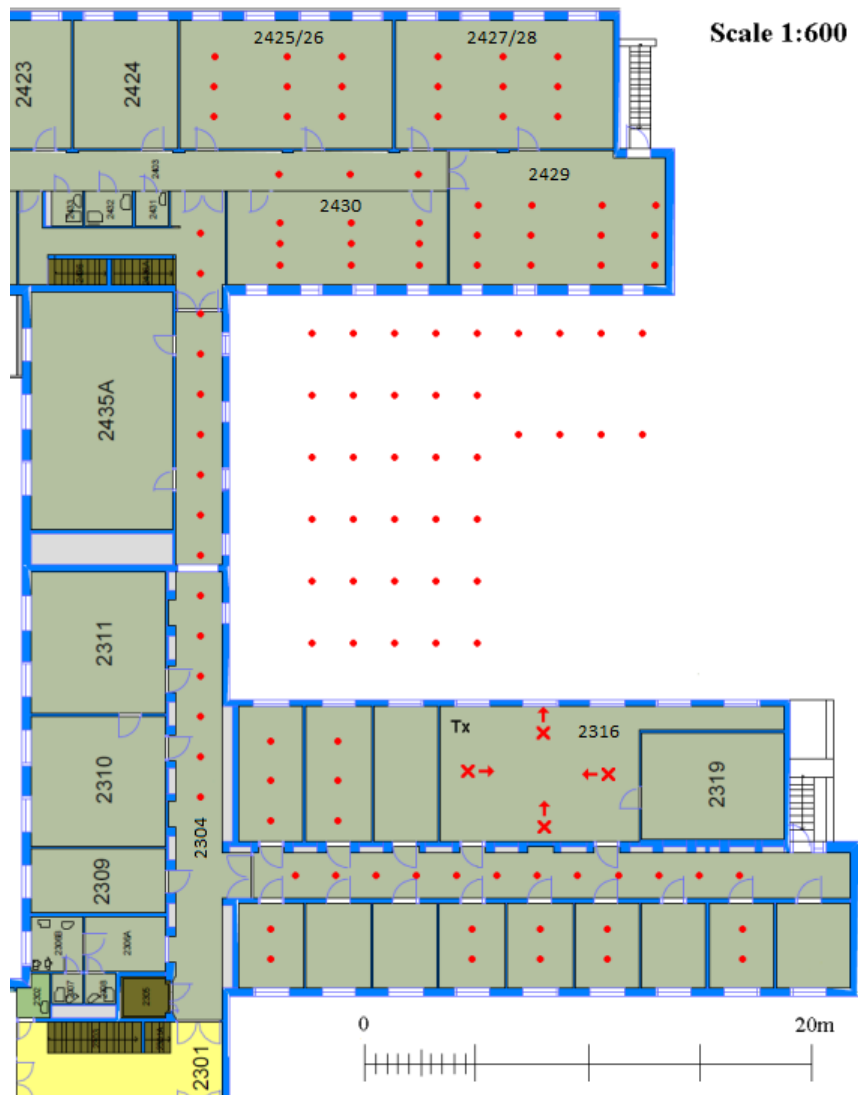


Figure 3-4: Overview of measurement positions

The Tx was placed in room 2316, on the 2<sup>nd</sup> floor, it was positioned next to the walls of this room to emulate likely femtocell installations. In total, there were 4 distinct placements, one for each wall. While the Tx was kept in room 2316 throughout, the Rx was moved between the surrounding rooms, corridors and outside of the building. To start with, the Rx was placed in the large laboratories (rooms 2425 to 2430), which are located within the northernmost block of E-

Huset, immediately across from the block containing the transmitter room. This arrangement means that the signal has to travel through the window to the outside then back into the building giving rise an IOI scenario. See Figure 3-5 for detailed information of the measurement positions.

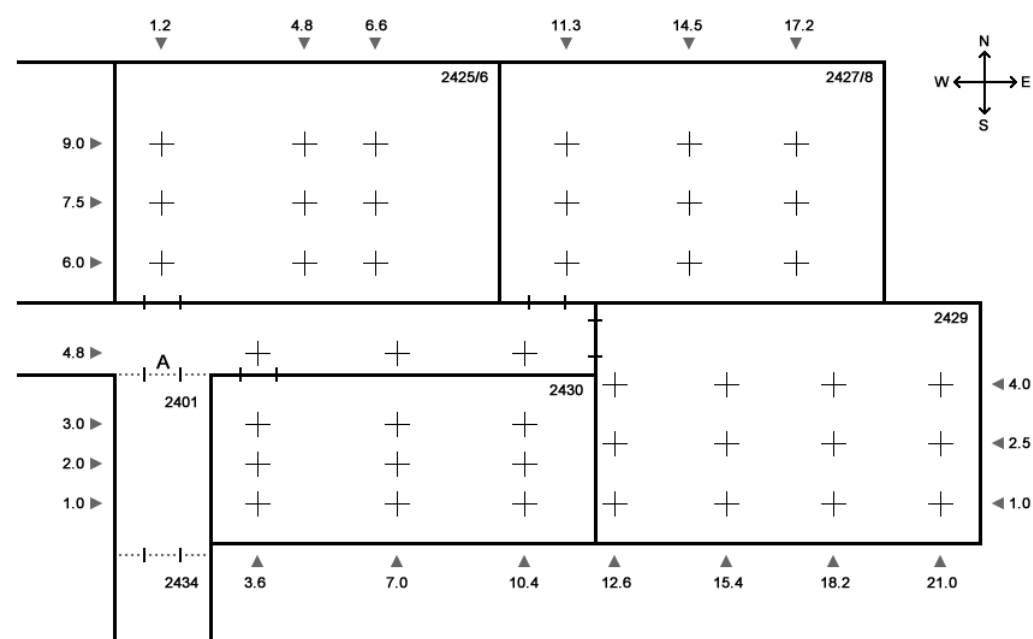


Figure 3-5: Measurement positions in rooms 2425-30

The dimensions of the 3 larger rooms are 9.7m by 6.0m while the smaller room 2430 is 9.7m by 4.2m. The crosses mark the south-west corner of the trolley table which the Rx was placed on. The orientation of the Rx was kept constant throughout all of the measurements, with the column mark by letter L facing north. To ensure the received power level was within the Rx's dynamic range the configuration of the 20 dB Attenuator 10 dB Low noise amplifier were varied throughout the measurement positions. For this part of the measurement the settings are shown as in Table 3-II:

Table 3-II Configuration of the attenuator and LNA in rooms 2325-30

Tx position	2425-2428 / corridor		2429		2430	
	Ant	LNA	Ant	LNA	Ant	LNA
N	-	√	-	-	-	-
S	-	√	-	-	√	√
E	-	√	-	√	-	-
W	-	√	-	√	-	-

√: modifier used, -: not used.

The next group of indoor Rx positions were measured in the corridor 2304. The first position was 2 meters south of door A, as labelled on Figure 3-5, and 1.3m west of the eastern corridor wall. For each subsequent position the Rx was moved 2 meters south until a total of 30 meters. The last set of indoor Rx positions was measured in the immediate surroundings of the Tx room 2316, including neighbouring offices and corridor. These rooms are smaller and more clustered, thus providing a contrasting environment to the large labs earlier. Most significantly, the signal do not propagate outdoors, so the scenario for these Rx positions is I2I, see Figure 3-6.

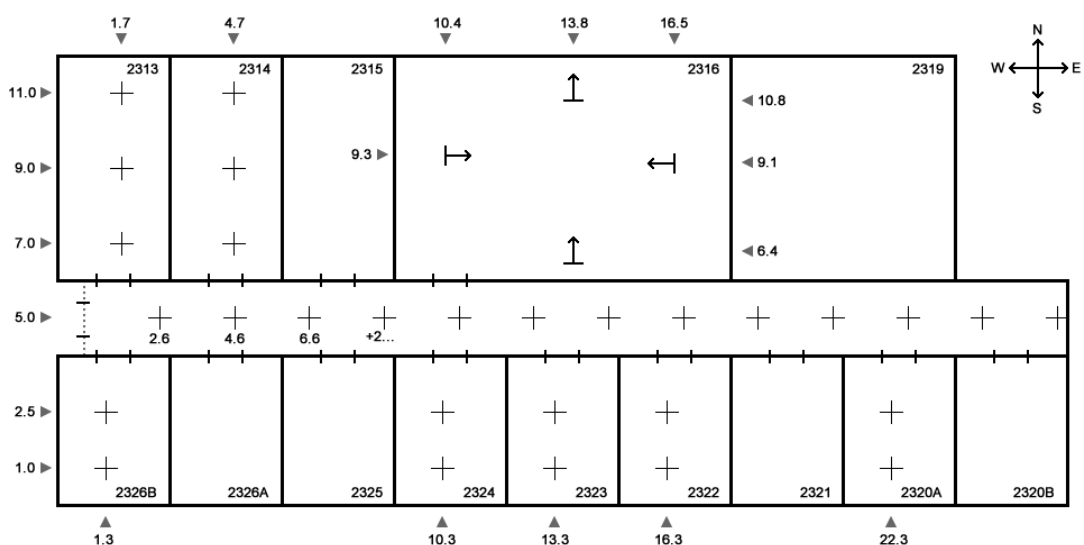


Figure 3-6: Measurements in offices immediately neighbouring the Tx.

Room 2316 is 9m by 6m, the bigger offices adjacent to it are 6m by 3m and the smaller ones to the south are 4m by 3m. This time the attenuator and the LNA were setup as shown in Table 3-III:

**Table 3-III Configuration of the attenuator and LNA in rooms 2313-26**

Tx position	2313 & 2326B		2314 & 2320-2324		Corridor 1, 11-13		Corridor 2-7		Corridor 8-10	
	Ant	LNA	Ant	LNA	Ant	LNA	Ant	LNA	Ant	LNA
N	-	✓	-	✓	✓	✓	✓	✓	✓	✓
S	-	✓	-	✓	✓	✓	✓	✓	✓	✓
E	-	✓	-	✓	✓	✓	✓	✓	✓	-
W	-	✓	-	✓	✓	✓	✓	-	✓	✓

✓: modifier used, -: not used.

The last set of measurements was done outside the building, in the enclosure between the block containing the Tx and the block to its north, where the first measurements were done, see Figure 3-4 for exact positions. The Rx positions formed several vertical lines parallel to the walls of corridor 2304, which were equidistantly separated by 2 meters. The first line was 4 meters from the corridor wall and the last line was 20 meters. Due to trees and bushes in the area not all the lines are of equal length, Table 3 provides the full details:

**Table 3-IV Details of the I2O measurement positions**

Line #	Distance from the wall (m)	Number of measurement blocks
1	4	50
2	6	50
3	8	50
4	10	50
5	12	50
6	14	15
7	16	15
8	18	15
9	20	15



### 3.3 Empirical Path Loss Model

#### 3.3.1 Data Reduction

The RUSK channel sounder records complex frequency responses, from which generates the 4 dimensional channel transfer matrices  $\mathbf{H}(t, f, i, j)$ . The variable  $t$  denotes time of the snapshots,  $f$  denotes frequency and  $i, j$  are the  $i^{\text{th}}$  Rx and  $j^{\text{th}}$  Tx antenna elements respectively. Firstly, the channel transfer matrices are transformed via the *Inverse Fourier Transform* into channel impulse response matrices  $\mathbf{h}(t, \tau, i, j)$ , where  $\tau$  denotes delay. Then we calculate the instantaneous received power  $P_r$  in Watts as [57]:

$$P_r(t, \tau, i, j) = |\mathbf{h}(t, \tau, i, j)|^2 \quad (3.1)$$

Next, the received power is averaged over antenna elements and snapshots:

$$\overline{P_r} = \frac{1}{N_s N_r N_t} \sum_{t=1}^{N_s} \sum_{i=1}^{N_r} \sum_{j=1}^{N_t} P_r(t, \tau, i, j) \quad (3.2)$$

where  $N_r = 32$  and  $N_t = 128$  are the number of Tx and Rx elements respectively and  $N_s = 10$  is the number of snapshots. Finally the path loss,  $PL$ , in dB is calculated as:

$$PL = P_t - 10 \log_{10} \overline{P_r} \quad (3.3)$$

where  $P_t = 40$  dBm is the total transmit power.  $PL$  is the path loss that is spatially averaged over antenna elements, as well as temporally averaged over snapshots.

### 3.3.2 Path Loss Formulation

Path loss is defined as the reduction in power from the Tx to the Rx and is often expressed in dB. A well-known path loss model has the form:

$$PL(d) = PL_0 + 10\gamma \log_{10} \left( \frac{d}{d_0} \right) + S \quad (3.4)$$

Where  $d$  is the T-R separation in meters,  $PL_0$  is the path loss at the reference distance  $d_0$ , and  $\gamma$  is the path loss exponent which determines the gradient of the average path loss with increasing distance.  $S$  in dB represents the shadow fading, which is modelled as a zero mean Gaussian random variable capturing the path loss deviation from its mean.  $S$  can be written as

$$S = x\sigma \quad (3.5)$$

with  $\sigma$  being the standard deviation of  $S$  and  $x$  representing a zero mean, unit variance Gaussian random variable.

### 3.3.3 Path Loss Model

First, we look at the path loss values obtained from the complete set of measurement data. Figure 3-7 shows a scatter plot of path loss versus T-R separation, along with a best fit curve of equation (3.4) using the *linear least squares* (LLS) method.

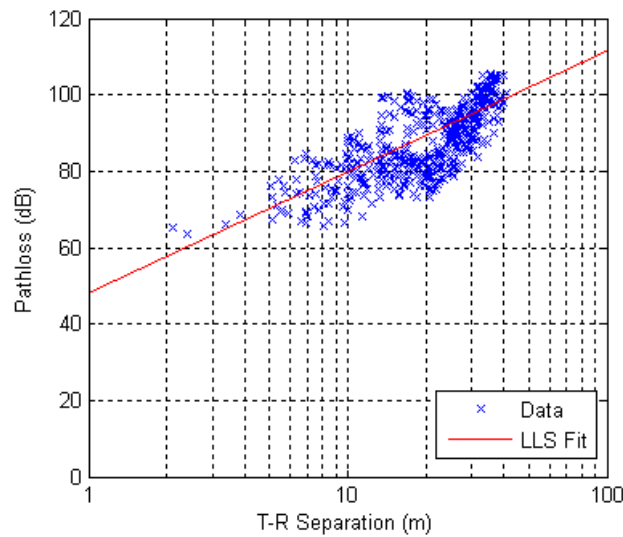


Figure 3-7: Path loss vs. T-R separation with LLS fit

With  $d_0 = 1\text{m}$  the estimate values of  $PL_0$ ,  $\gamma$  and  $\sigma$  are given in Table 3-V, which are comparable to the results reported in the references [28] and [45]. The pass loss exponent obtained by applying regression on the measurement data (3.04) is greater than the free space pass loss exponent (2), which is expected. Since the measurement environment contains walls and other obstacles.

Table 3-V: Parameter values for the complete data set

Parameter	Estimate	Std Error
$PL_0$	48.0 dB	1.23
$\gamma$	3.04	0.18
$\sigma$	5.23 dB	0.31

As mentioned in the previous section, depending on the position of the Rx, the measurement data can be grouped into 3 distinct scenarios: Indoor-to-Indoor (I2I), Indoor-to-Outdoor (I2O), and Indoor-to-Outdoor-to-Indoor (IOI). Figure 3-8 shows separate scatter plots of path loss vs propagation distance for data from each of the three groups.

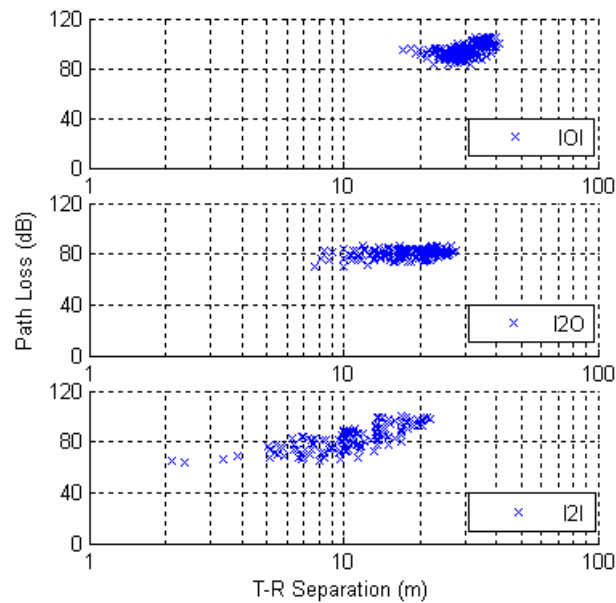


Figure 3-8: Path loss vs. T-R separation showing separate scenarios

As can be seen from Figure 3-8, the correlation between pass loss and distance differs notably between scenarios: the pass loss exponent, exhibited by the steepness of the gradient, is visibly higher in IOI and I2I scenarios. This demonstrates that environmental factors have significant influence on the parameters of a propagation model, which can be clearly seen in Table 3-VI after applying LLS to data from each group individually.

**Table 3-VI: Parameter values for each scenario**

<b>Parmater</b>	<b>IOI</b>	<b>I2O</b>	<b>I2I</b>
$PL_0$ (dB)	33.1	64.0	41.4
$\gamma$	4.17	1.31	4.03
$\sigma$ (dB)	4.38	3.08	6.20

As can be seen, the resulting parameters for different scenarios form a sharp contrast. For IOI and I2I scenarios,  $\gamma$  becomes even higher whilst  $PL_0$  is reduced. This is reasonable as in these two scenarios a large proportion of the propagation happens indoors. On the other hand, the value of  $\gamma$  for the I2O scenario is less than that of free space, which is surprising. This suggests that there must be other factors influencing the path loss besides distance. As model (3.4) considers only distance, it does not take into account environmental factors and therefore cannot differentiate between, for example, I2I and I2O scenarios within the data.

A model that considers the effects of walls and ceilings would better predict the path loss, and give more insights into the path loss behaviour between rooms, floors and the indoor/outdoor interface. Ref [46] proposes a path loss model that incorporates walls into the equation, but as it is not based on measurements it uses constant theoretical values of  $PL_0$  and  $\gamma$ . If we incorporate walls and extract the parameters from our data we can arrive at the following model:

$$PL(d) = PL_0 + 10\gamma \log_{10} \left( \frac{d}{d_0} \right) + nW + S \quad (3.6)$$

Where  $n$  is the number of walls and windows between each Tx-Rx pair; and  $W$  is the average loss of signal strength in dB through each wall or window. With this formulation the estimated value and standard errors of the parameters obtained by applying LLS are as shown in Table 3-VII. The largest p-value of the estimates was  $2.2 \times 10^{-8}$ , giving >99.9% confidence level to the estimated value of the parameters.

**Table 3-VII: Parameter values for model (3.6)**

Parameter	Estimate	Std Error
$PL_0$ (dB)	44.3	1.08
$\gamma$	2.66	0.10
$\sigma$ (dB)	3.26	0.13
$W$ (dB)	5.7	0.21

The value of  $PL_0$  is similar to the previous model, but  $\gamma$  is reduced. This is expected as a proportion of the path loss is accounted by walls, which has an attenuation factor of 5.7 dB per wall. Figure 3-9 shows the measured data drawn on a scatter plot, compared the predicted path loss of model (3.6) drawn as a function of distance and number of walls. By visual inspection, the shape of the predicted values match the measured values closely.

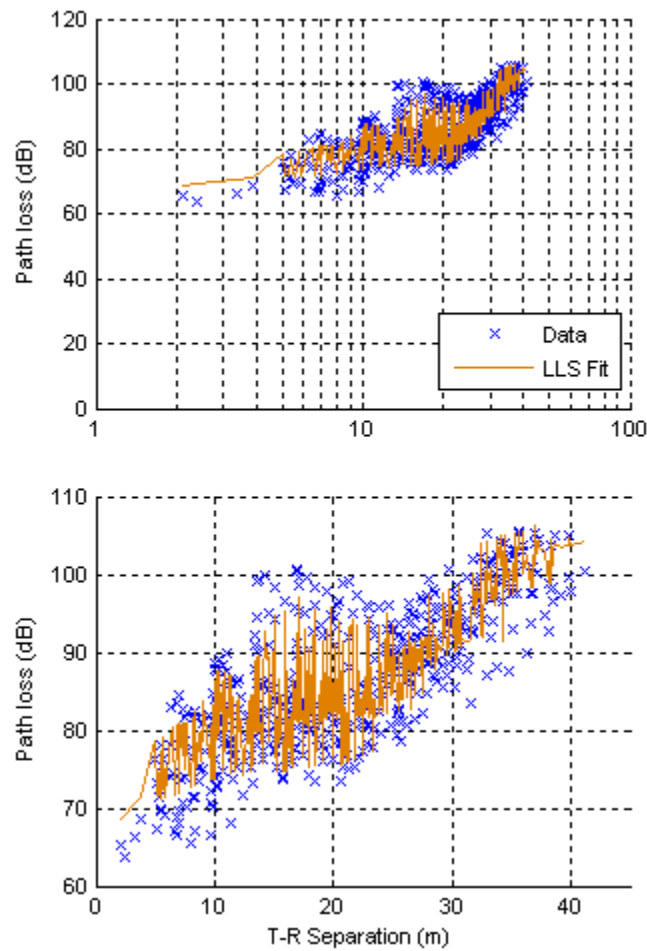


Figure 3-9: Fit of proposed path loss model against measured data

Figure 3-10 shows a scatter plot of the data colour coded by the parameter  $W$ , which represents the number of walls between Tx and Rx. The dotted lines are colour coded in the same way and each line represents the predicted path loss of model (3.6) for particular value of  $W$ . It can be seen that overall the model provides a good fit, as each coloured line is a good fit to the correspondingly coloured data points. The RMS residuals are 2.94dB, 3.33dB, 5.15dB and 4.54dB for  $w = 1, 2, 3$  and  $4$  respectively, all of which are smaller than 6.15dB for model (3.4).

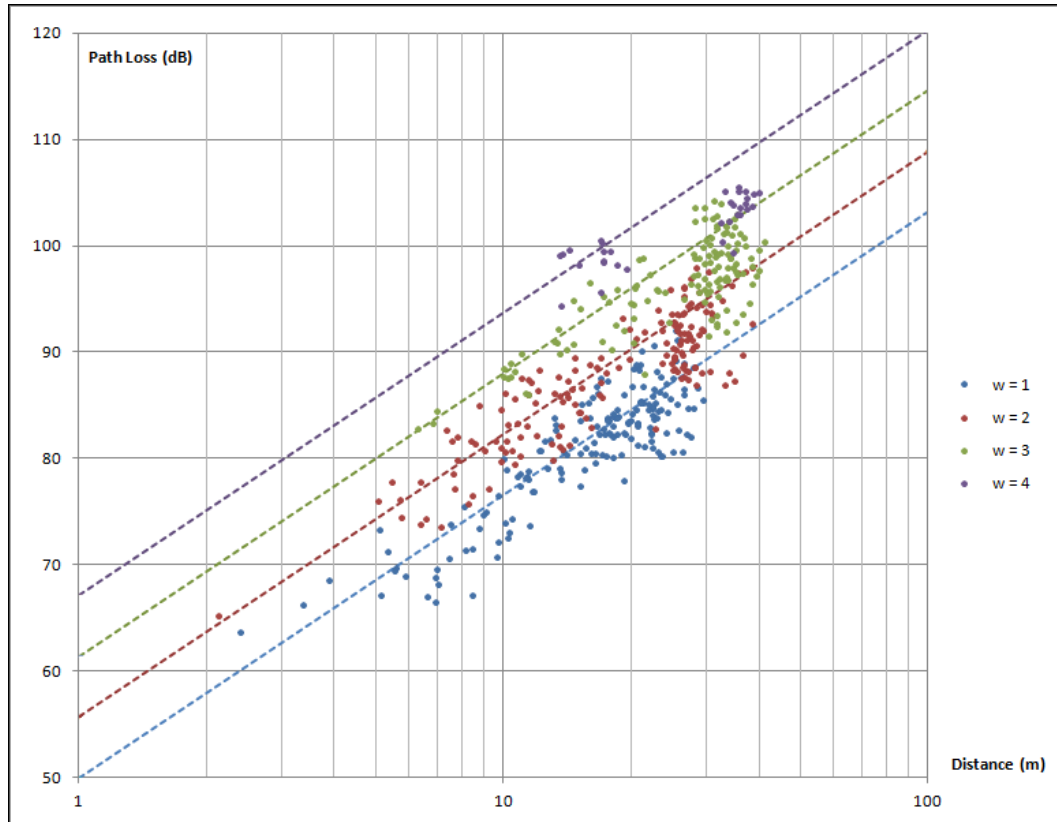


Figure 3-10: Goodness of fit of model (3.6) for different values of  $W$



Figure 3-11 shows an evaluation of the goodness of the fit of model (3.6) by plotting the value of pass loss predicated by the models against the value of pass loss calculated from actual measurement data. It can be seen that the predicated and measured value are strongly correlated in all scenarios. The RMS error of predicted path loss for model (3.6) is 3.73dB compared to 6.15dB for model (3.4). For individual scenarios the RMS errors are: 3.34dB for IOI, 2.26dB for I2O, and 4.79 dB for I2I.

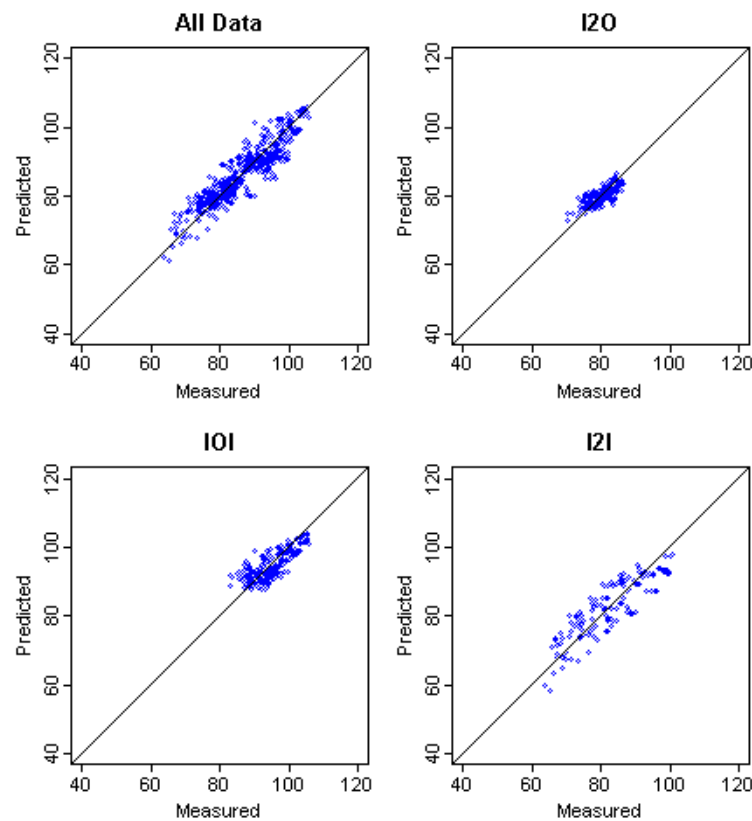


Figure 3-11: Predicted vs. Measured path loss for model (3.6)

If we apply (3.6) separately to the 3 different scenarios we obtain the parameter values shown in Table 3-VIII. The value of parameter  $W$  varies between 4dB for windowed walls (I2O scenario) to 7dB for internal walls (I2I scenario). We can also observe a correlation between the value of pass loss exponent and the amount of obstacles in the propagation environment. This is in line with expectations as obstacles tend to disperse and weaken the signal which will result in higher pass loss and pass loss exponent.

**Table 3-VIII: Parameter values of each scenario for proposed model**

Parameter	IOI	I2O	I2I
$PL_0$ (dB)	46.9	48.6	42.5
$\gamma$	2.54	2.37	2.96
$\sigma$ (dB)	3.62	2.27	4.74
$W$ (dB)	4.73	3.94	7.08

### 3.4 Model Validation

Further measurements were carried out in comparable environments in order to evaluate the proposed model. The experiments took place at the Luton campus of University of Bedfordshire, in the main campus building. Sections of the building form a three sided enclosure in a similar fashion to the “E-Huset” building of Lund Institute of Technology (see Figure 3-4), allowing both I2I and IOI measurements to be carried out. Figure 3-12 provides an overview of the measurement positions. The cross marks the position of the Tx whilst the dots mark the positions of the Rx. All of the rooms were unoccupied during the measurements.

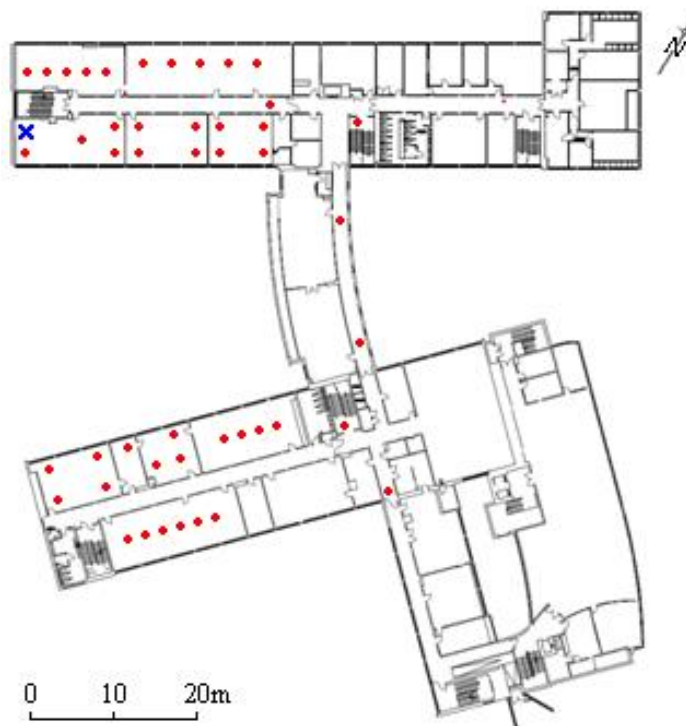


Figure 3-12: Overview of the Luton measurement campaign

Two Anritsu slim monopole antennas were used as the transmitting (Tx) and receiving (Rx) antenna, which were omnidirectional in the azimuth plane, with vertical beamwidth of  $47^\circ$  and maximum gain of  $G = 2\text{dBi}$ . The Tx was attached to the output of a Rohde & Schwarz RF signal generator, configured to 2.6GHz frequency and 19dBm output power, whilst the Rx was attached to the input of a Rohde & Schwarz Spectrum Analyzer, which was configured to a resolution bandwidth of 30 kHz across a 2MHz span, with a sweep time of 0.5s.

The peak received power was averaged over 50 sweeps to reduce the effects of fast fading. The receiving unit was moved around to various locations within the building whilst the Transmitting unit was kept in the same location. For each Rx position, the Tx was placed in 1 of 4 pre-designated positions marked out by a template. The positions were 20cm apart; this was done to reduce the effect of multipath fading by applying spatial averaging across the four readings.

### 3.4.1 Model comparison for Luton data

Figure 3-13 shows the scatter plots of path loss against propagation distance for the Luton data. The dots represents measured path loss whereas the solid line represents the predicted path loss for given propagation distance. It can be seen that the model (3.6) predicts the path loss much more accurately than model (3.4), the *Normalised root mean square error* for model is 0.043 (3.6) compared to 0.145 for model (3.4).

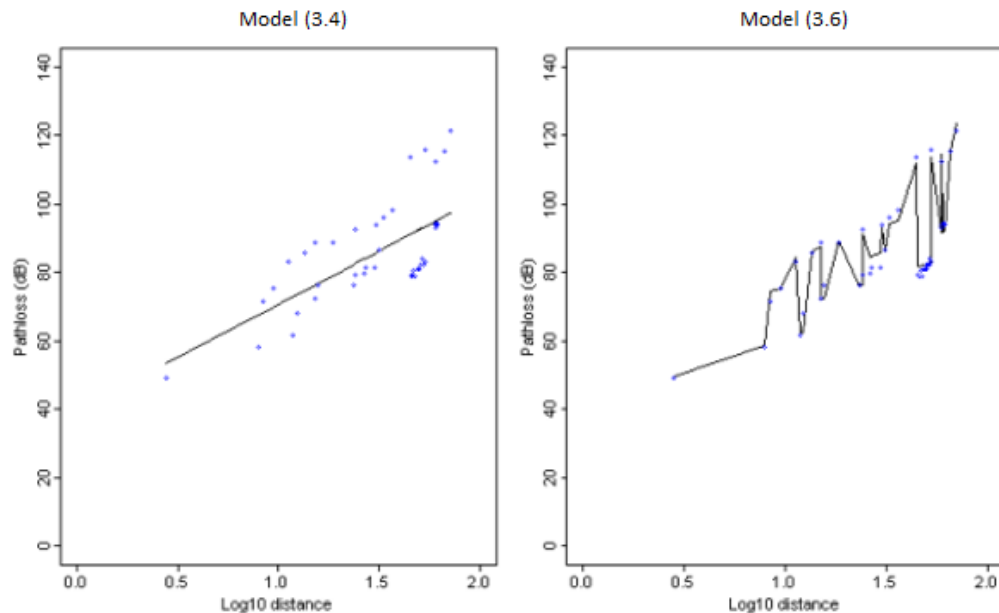


Figure 3-13: Scatter plot of the Luton data comparing the predictions made by the models

Figure 3-14 plots the predicted path loss against the measured path loss, it is evident that these two values are much more correlated in model (3.6) than model (3.4), in other words the predictions made by model (3.6) are much more accurate.

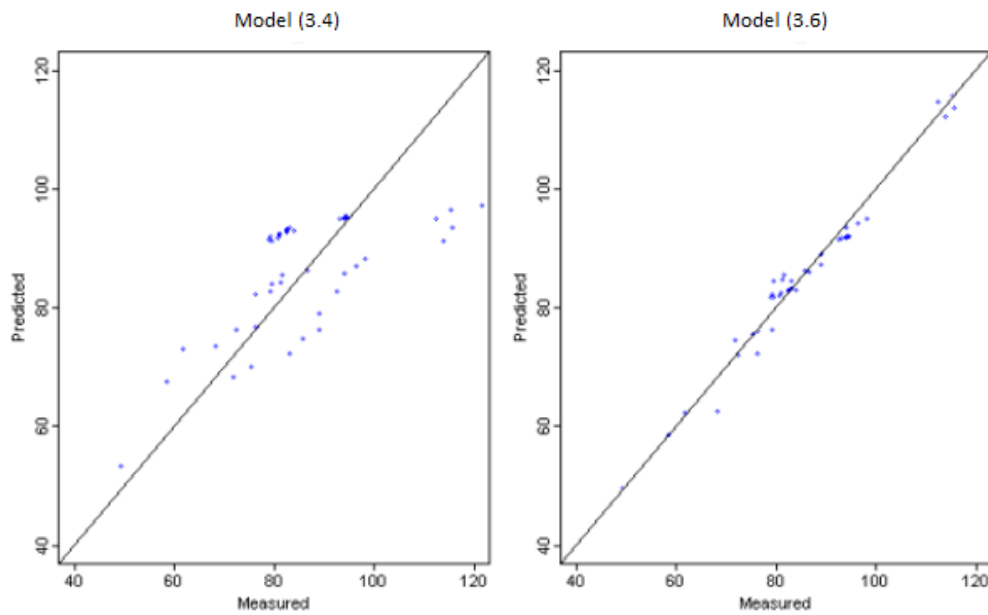


Figure 3-14: Comparison between measured and predicted path loss

### 3.4.2 Comparison between Lund and Luton datasets

Applying model (3.4) to the Luton data gives parameter values  $PL_0 = 39.4\text{dB}$ ,  $\gamma = 3.14$  and  $\sigma = 4.87\text{dB}$ , which are comparable to the parameter values from the Lund data ( $PL_0 = 48.0\text{dB}$ ,  $\gamma = 3.04$  and  $\sigma = 5.23\text{dB}$ ). This result shows that the two propagation environments measured are indeed quite similar, at least when expressed through the exponential model. The parameter values obtained from applying model (3.6) to the Luton data are shown in Table 3-IX below, these values are in good agreement with the parameters values obtained from the Lund data.

Table 3-IX: Parameter values of model (3.6) for Luton data

Parameter	Value	Std Error
$PL_0$	40.4 dB	1.23
$\gamma$	2.47	0.18
$\sigma$	3.75 dB	0.26
$W$	6.63 dB	0.39

Table 3-X shows a side by side comparison of the parameter values obtained from applying models (3.4) and (3.6) to the Lund and Luton data. Comparing the parameter values from the models reveals that the pass loss exponent  $\gamma$  is lower in model (3.6) than model (3.4) for both datasets, this is due to a portion of the pass loss in model (3.6) being taken up by the wall loss  $W$ . The parameter values between datasets for each model are similar. As model (3.4) is the standard exponential model, similar parameter values across datasets suggest similar propagation environments. With this in mind, the closeness of parameter values between Lund and Luton data for the model (3.6) becomes a validation of the consistency and accuracy of model at characterising the propagation environment under study, which is of course the small cells environment.

Table 3-X: Parameter comparison between datasets and models

Parameter	Model (3.4)		Model (3.6)	
	Lund	Luton	Lund	Luton
$PL_0$ (dB)	48.0	39.4	44.3	40.4
$\gamma$	3.04	3.14	2.66	2.47
$\sigma$	5.23	4.87	3.26	3.75
$W$ (dB)	—	—	5.74	6.63

### 3.5 Summary

This chapter reported a comprehensive MIMO measurement campaign including details of equipment, setup and measurement procedure. The data features indoor, indoor-to-outdoor and building-to-building propagation scenarios, from which the path loss were extracted. The path loss values were used to construct an empirical path loss model accounting for wall loss. This distinguishes between the different propagation scenarios and allowed relevant parameters to be extracted using proven statistical methods. The model showed good accuracy with parameters achieving statistically significant confidence values.

The model was further validated by a separate measurement campaign in a comparable environment which also featured I2I, I2O and IOI propagation scenarios. The parameters from the two datasets are in good agreement with each other, as well as with previously reported findings. Due to the relative simplicity of the formulation, the proposed model can be quickly used to characterise the path loss in small cell environments that features many buildings, it can also be implemented in system level simulations quickly without much requirements.



## CHAPTER 4

# CHANNEL PARAMETERS AND RELATED STATISTICS

*This chapter present the values of key channel characters of RMS delay spread and coherence bandwidth, along with some other channel parameters obtained through the in-depth analysis of channel data used in the previous chapter. The results of this chapter builds on from the previous chapter to give a more complete picture about the properties of the wireless channel in the small cells scenario.*

## 4.1 Introduction

Wireless channel statistics obtained from measurements within targeted deployment scenarios provide a reliable way of deriving accurate propagation models required for the design and analysis of mobile communication systems [58], [59]. Existing channel models developed by 3GPP [60], COST 2100 [61] and WINNER II [48] all have their underlying basis in the analysis of measurement data from specifically chosen scenarios.

This chapter focuses on the analysis of spatial, frequency and delay domain statistics derived from a comprehensive MIMO channel sounding campaign carried out in Lund University, Sweden [62, 63]. The data accounts for spatial diversity through MIMO antennas; temporal diversity through waveform duration; amplitude and phase information; horizontal and vertical polarisation; and contrasting indoor-to-indoor (I2I) and indoor-to-outdoor (I2O) propagation environments. Due to the extensive measurement setup and quantity of acquired data, most channel characteristics of interest can be computed and analysed in terms of their statistical distributions. Notable parameters such as delay spread, coherence bandwidth, angle-of-arrival, polarization effects, and path loss are investigated here.

## 4.2 Analysis of Channel Parameters

From the RUSK channel sounder the frequency domain complex channel transfer matrix  $\mathbf{H}(t, f, i, j)$  is provided, and the channel impulse response matrix  $h(t, \tau, i, j)$  is obtained through the Inverse Fourier Transform. The variable  $t$  represents the time of snapshots,  $f$  denotes the frequency,  $\tau$  is the delay, and  $i, j$  are the  $i^{\text{th}}$  Rx and  $j^{\text{th}}$  Tx antenna element respectively. From  $h$  the instantaneous received power can be estimated:

$$P(t, \tau, i, j) = |h(t, \tau, i, j)|^2 \quad (4.1)$$

The *Power Delay Profile* (PDP) is obtained through spatial averaging of antenna elements. As the Rx is circular, its columns are at different angles with respect to the Tx, and will exhibit different statistics in terms of frequency correlation and delay spread. Consequently, the dimension denoted by  $i$  in (4.1), which corresponds to Rx elements, is split into two dimensions  $i_r$  (corresponding to the  $N_{ir} = 4$  rows of Rx) and  $i_c$  (corresponding to the  $N_{ic} = 16$  columns of Rx), the rows  $i_r$  are averaged whilst the columns are  $i_c$  preserved. The Tx, on the other hand, is planar and both its rows and columns are averaged. This produces the matrix  $P(t, \tau, i_c)$  which contains the PDP for each snapshot  $t$  and receiver column  $i_c$ .

$$P(t, \tau, i_c) = \frac{1}{N_{ir}N_j} \sum_{i_r=1}^{N_{ir}} \sum_{j=1}^{N_j} P(t, \tau, i_r, i_c, j) \quad (4.2)$$

Collectively, the antenna elements capture latent variations in small-scale multipath interactions, thus averaging over them reduces the effects of spatial fading and yield a more indicative PDP, from which the values of several channel parameters can be determined.

### 4.2.1 RMS Delay Spread

The *root mean squared (RMS) delay spread* quantifies the RMS value of delayed energy that results from multipath propagation. It gives an indication of time dispersion effects on receiver performance as well as the nature of inter-symbol interference, which are useful for determining parameters such as maximum transmission rate and symbol period. To calculate the RMS delay spread, the  $N_s$  snapshots are averaged to reduce the effects of temporal fading.

$$\bar{P}(\tau, i_c) = \frac{1}{N_s} \sum_{t=1}^{N_s} P(t, \tau, i_c) \quad (4.3)$$

For each Rx column  $i_c$ , a threshold of  $S$  dB below the maximal peak is applied to the individual values of the averaged PDP to distinguish the multipath components from noise:

$$\bar{P}^*(\tau_k) = \begin{cases} \bar{P}(\tau_k), & \bar{P}(\tau_k) \geq \frac{\max \bar{P}(\tau)}{10^{S/10}} \\ 0, & \text{otherwise.} \end{cases} \quad \text{for } k = 1..N_\tau \quad (4.4)$$

The mean delay,  $\tau_a$ , is calculated next. Here,  $N_\tau$  denotes the number of samples of impulse response in the delay domain.

$$\tau_a = \frac{\sum_{k=1}^{N_\tau} \tau_k \cdot \bar{P}^*(\tau_k)}{\sum_{k=1}^{N_\tau} \bar{P}^*(\tau_k)} \quad (4.5)$$

From  $\tau_a$ , the RMS delay spread  $\tau_{rms}$  is computed as [64]:

$$\tau_{rms} = \sqrt{\frac{\sum_{k=1}^{N_\tau} (\tau_k - \tau_a)^2 \cdot \bar{P}^*(\tau_k)}{\sum_{k=1}^{N_\tau} \bar{P}^*(\tau_k)}} \quad (4.6)$$

Consideration needs to be given to the value of  $S$ , as it directly affects the value of  $\tau_{rms}$ . Commonly used values of  $S$  seen in the literature include 10dB, 15dB and 20dB [65]; which set the threshold to 6 - 33dB above the noise floor depending on the measurement position. After some initial analysis and testing, the value of 20dB was chosen because it is large enough to filter out the noise whilst still keep most of the weaker multipath components. When smaller thresholds were tested, a significant portion of weak multipath components were removed alongside noise.

Figure 4-1 shows the normalised histograms of  $\tau_{rms}$  for different situations, which provides an estimation for the *probability density function* (PDF) of the underlying variable. The figures on the top row are for I2I; the figures on the bottom row are for I2O; the left two are for Rc (receiver column) facing Tx; the right two are for Rc opposite Tx. The abscissa represents the RMS delay of a channel in  $\mu s$ , this is a discrete scale with resolution of 5ns. The ordinate is the probability that the RMS delay of a channel falls within the 5ns sized bins.

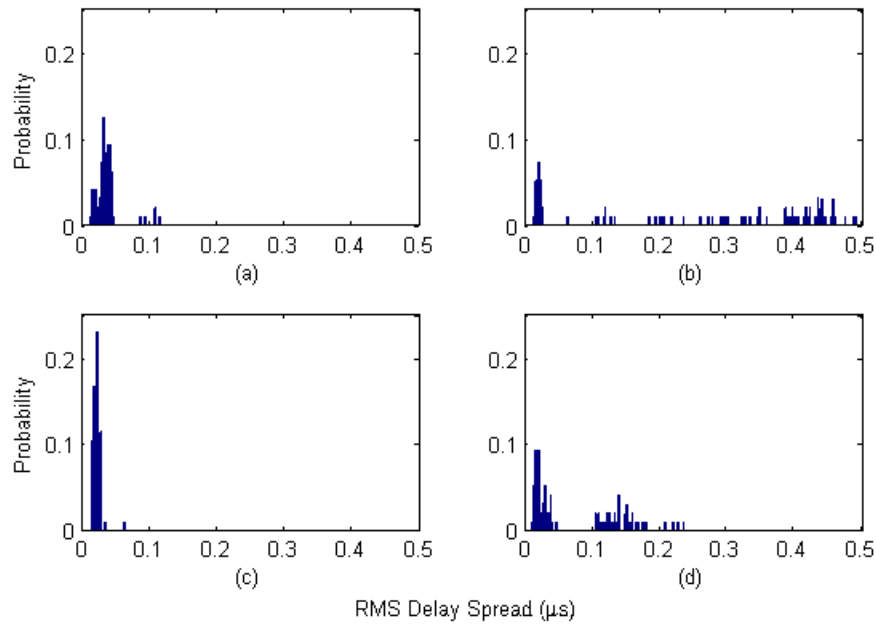


Figure 4-1: RMS delay spread PDF: I2I (top), I2O (bottom), Rc facing Tx (left), Rx opposite Tx (right)

Looking at the delay spread, we observe higher delay values and greater spread for the I2I scenario on top row compared with corresponding I2O scenario on the bottom row. This matches with expectation as the I2I scenario contains more obstacles which can introduce greater delays between multipath components. Comparing the columns, we also see higher delay and spread for Rc opposite Tx than corresponding Rc facing Tx, this is also rational since in the former case the signal have to reflect off a surface before reaching the receiver elements that are in the opposite direction as the transmitter.

In the specific case of I2O and Rc facing Tx (bottom left), there are not many obstacles obstructing the direct path from Tx to Rx so we see that the delay are almost all concentrated between  $0.01\mu\text{s}$  to  $0.03\mu\text{s}$ . In contrast, for I2I and Rc opposite Tx case (top right) the delays are much more uniformly spread from  $0.1\mu\text{s}$  to  $0.5\mu\text{s}$ .

Figure 4-2 shows the *cumulative distribution function* (CDF) of the same data, in all cases the 99<sup>th</sup> percentile for  $\tau_{rms}$  is less than  $0.6\mu\text{s}$ , giving a reliable indication of the upper bound.

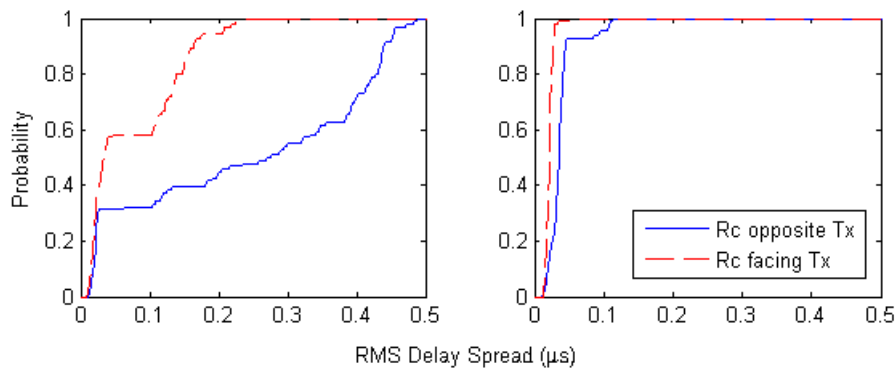


Figure 4-2: RMS Delay spread CDF Comparison: I2I (left), I2O (right)

The values of  $\tau_{rms}$  for selected Rc are shown in TABLE 4-I. Rc1 is directly facing the Tx and the column number increases clockwise around the antenna. The table includes cumulative values for the 50, 75 and 90 percentiles. As can be seen, the Rx column that directly faces the Tx (Rc1) has the least  $\tau_{rms}$  whilst the column that is opposite of the Tx (Rc9) has the greatest  $\tau_{rms}$ , the other two columns that faces perpendicularly to the Tx are in-between. Furthermore, for a given Rc and percentile, the value of  $\tau_{rms}$  for I2O is smaller than the corresponding value for I2I for all 12 cases.

**TABLE 4-I: RMS DELAY SPREAD FOR SELECTED  $R_x$  COLUMNS**

Scenario	Percentile	$\tau_{rms}$ ( $\mu s$ )			
		Rc1	Rc5	Rc9	Rc13
I2I	50	0.035	0.142	0.291	0.153
	75	0.137	0.238	0.413	0.249
	90	0.182	0.376	0.452	0.363
I2O	50	0.020	0.031	0.039	0.027
	75	0.024	0.038	0.046	0.038
	90	0.029	0.043	0.051	0.041

### 4.2.2 Coherence Bandwidth

The Coherence Bandwidth,  $B_c$ , describes the maximum frequency interval in which signals experience correlated fading. Related to the  $\tau_{rms}$ ,  $B_c$  is superior at predicting some aspects of system performance such as measuring time dispersion.  $B_c$  can be estimated directly from the channel transfer matrix  $\mathbf{H}(t, f, i, j)$ . For each antenna pair  $i, j$ , the correlation coefficient,  $\rho_{xyij}$ , between frequency response samples  $x_{ij} = H(t, f_x, i, j)$  and  $y_{ij} = H(t, f_y, i, j)$  is estimated, and the process is repeated for all frequency pairs  $f_x, f_y$  [66]:

$$\rho_{xyij} = \frac{R_{xyij}}{\sigma_{xij}\sigma_{yij}} \quad (4.7)$$

where  $R_{xyij}$  is the normalised zero-lag cross-correlation between  $x_{ij}$  and  $y_{ij}$ , whilst  $\sigma_{xij}$  and  $\sigma_{yij}$  are the respective standard deviations. Arranging  $\rho_{xyij}$  in matrix form with  $x$  and  $y$  as indices produces the symmetric correlation coefficient matrix,  $\rho_{ij}$ . Each row,  $x$ , of  $\rho_{ij}$  contains the correlation of frequency  $f_x$  with all 81 frequencies including itself, and similarly for each column  $y$ . Hence the main diagonal of  $\rho_{ij}$  is the autocorrelation, and the frequency offset between  $f_x$  and  $f_y$  increases with each sub-diagonal. Averaging over the diagonals gives the correlation profile as a function of the frequency offset.

$B_c$  is derived from the interaction of the correlation profile with a predetermined threshold,  $T$ , normally set at 0.5, 0.7 or 0.9 [67]. The first frequency offset at which the profile falls below the threshold gives the value of  $B_c$  for that threshold.



Figure 4-3 shows the PDF of  $B_c$  of the 3 thresholds for I2O measurement data compared to I2I measurement data. It can be observed that the coherence bandwidth becomes smaller as the threshold gets higher, this is because the correlation generally decrease as the frequency offset increases. Furthermore, for a given threshold, the value of  $B_c$  for the I2I scenario is lower than that of the I2O scenario for all thresholds. This result further validates the data since  $B_c$  and  $\tau_{rms}$  are reciprocally related. The previous section has shown that  $\tau_{rms}$  is larger for the I2I scenario, hence it is expected that the  $B_c$  would be smaller for the I2I scenario.

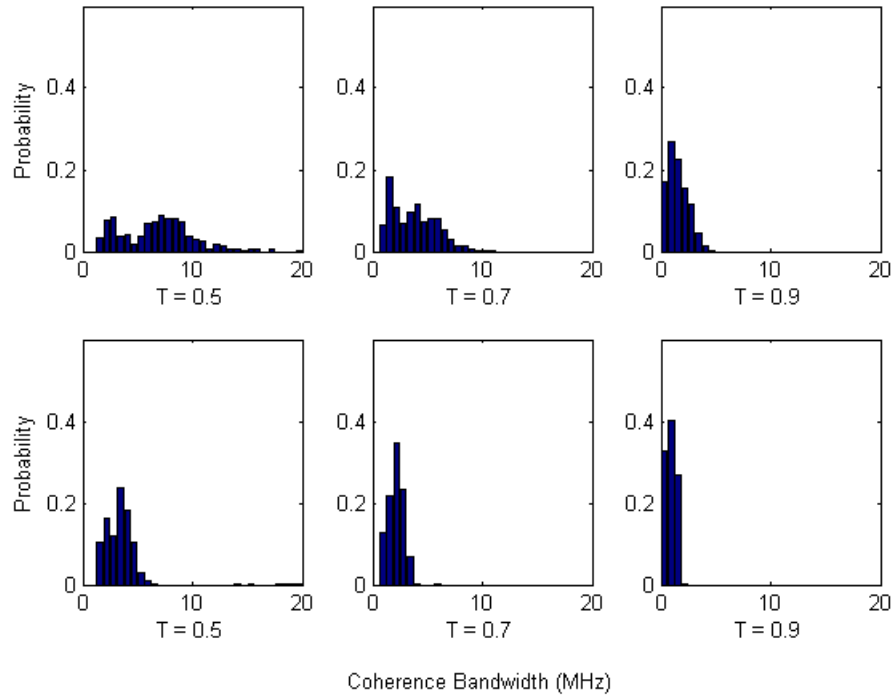


Figure 4-3: Coherence bandwidth PDF for I2O (top) and I2I (bottom)

Figure 4-4 shows the corresponding CDFs for the Coherence Bandwidth. Again, it is clear that the mean and expectation of the  $B_c$  is smaller for the I2I scenario.

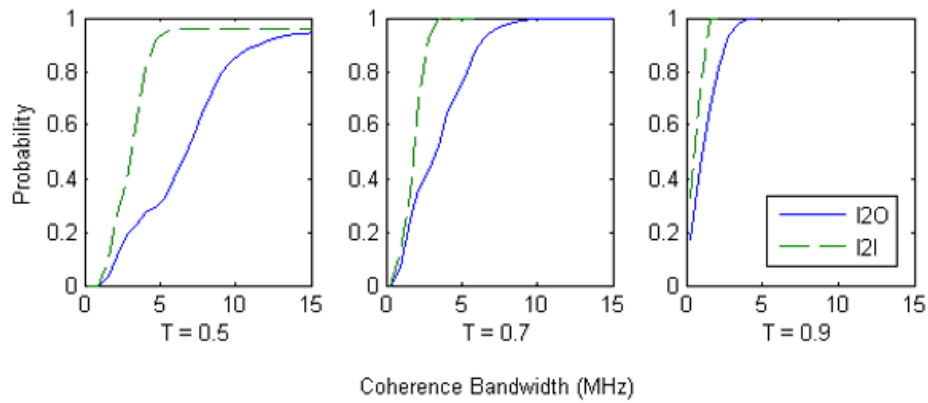


Figure 4-4: Coherence bandwidth CDF Comparison

TABLE 4-II provides more detailed results on the characteristics of coherence bandwidth.

TABLE 4-II: COHERENCE BANDWIDTH

Scenario	Percentile	B <sub>c</sub> (MHz)		
		T = 0.5	T = 0.7	T = 0.9
I2I	50	3.75	2.50	1.25
	75	4.38	3.13	1.88
	90	5.00	3.75	1.88
I2O	50	7.50	3.75	1.88
	75	9.38	5.63	2.50
	90	12.50	6.88	3.13

### 4.2.3 RMS Angular Spread

RMS Angular spread is a parameter that is useful for the successful design of MIMO and smart antenna systems [68]. It can be estimated from the data obtained with the cylindrical patch array at the Rx. The instantaneous received power is averaged for each column of the Rx, producing the *power azimuth spectrum* (PAS) with  $22.5^\circ$  angular resolution as shown in Figure 4-5. This is fine enough to give a useful indication of the angular spread. Specialized spatial processing techniques such as ESPRIT [69] can be used to achieve higher resolution, which will be investigated in further work but currently beyond the scope of this thesis.

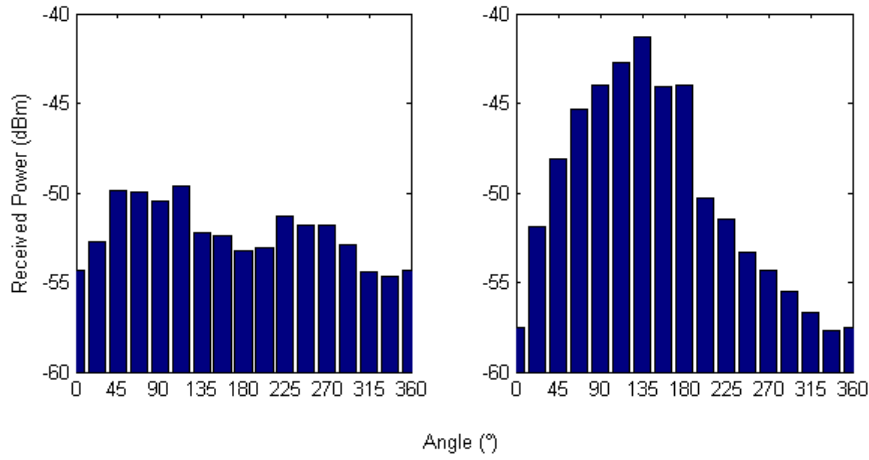


Figure 4-5: PDF of angle of maximal received power

From here we can calculate the RMS angular spread in a similar manner to the RMS delay spread [64].

$$\theta_{rms} = \sqrt{\frac{\sum_{k=1}^{N_\theta} (\theta_k - \theta_a)^2 \cdot P(\theta_k)}{\sum_{k=1}^{N_\theta} P(\theta_k)}} \quad (4.8)$$

where  $P(\theta_k)$  is the received power at angle  $\theta_k$ , and  $\theta_a$  is the mean angle-of-arrival.

$$\theta_a = \frac{\sum_{k=1}^{N_\theta} \theta_k \cdot P(\theta_k)}{\sum_{k=1}^{N_\theta} P(\theta_k)} \quad (4.9)$$

Once  $\theta_{rms}$  has been computed for each measure position, the normalised histogram of the angular spread can be obtained, as shown in Figure 4-6

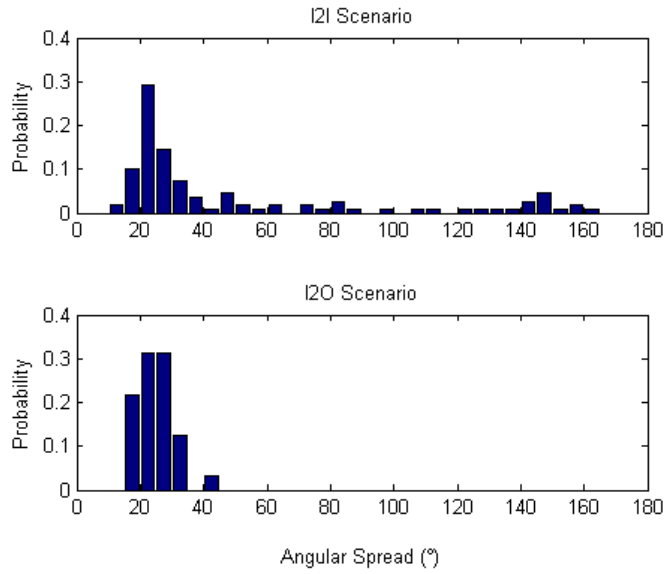


**Figure 4-6: PDF of RMS Angular Spread**

The median  $\theta_{rms}$  values are similar (I2I: 27.5°, I2O: 23.9°); the mean  $\theta_{rms}$  value for the I2I scenario is considerably higher, as is the variance. (I2I:  $\mu = 50.4^\circ$ ,  $\sigma = 44.0^\circ$ ; I2O:  $\mu = 25.1^\circ$ ,  $\sigma = 5.8^\circ$ ). Both result from the presence of a significant number of data points with higher values of  $\theta_{rms}$ . This is expected as the I2I environment is more multipath rich and interactions with disperse obstacles results in multipath components that arrive at a wider range of angles.

### 4.3 Summary

This chapter builds upon the previous one by analysing and extracting the key channel parameters for the typical propagation scenarios found in small cell environments. The RMS delay spread, coherence bandwidth and RMS angular spread were derived for the I2I and I2O scenarios; and comparisons were made between them where the differences were analysed and discussed.

The results are useful for a range of applications.  $\tau_{rms}$  is required for several system design applications as it can determine the maximum transmission rate and symbol period;  $B_c$  helps with waveform design because it allows the choosing of bandwidths large enough to sustain reliable reception in spite of fading; finally  $\theta_{rms}$  is a useful statistic in MIMO diversity and antenna design as both involve considerations of spatial geometry, can thus make use of the spatial nature of the angular spread. TABLE 4-III provides a complete summary of the parameters presented in this paper.

TABLE 4-III: SUMMARY OF THE CHANNEL PARAMETERS

Scenario	$\tau_{rms}$ ( $\mu s$ )			$B_c$ (MHz)			$\theta_{rms}$ ( $^\circ$ )		
	Min	Med	Max	Min	Med	Max	Min	Med	Max
I2I	0.01	0.26	0.80	0.63	3.75	26.3	11.2	27.5	160
I2O	0.01	0.04	0.32	1.88	7.50	30.6	16.9	23.9	42.5

## CHAPTER 5

# ANTENNA POLARISATION EFFECTS ON RECEIVED SIGNAL

*Antennas do not perform uniformly across the azimuth or elevation planes: any change in the angle between a transmitter and receiver will introduce variations in the resulting signal level. In dual-polarised MIMO channels, this happens often and introduces depolarisation or cross-coupling. However, the statistical description of these polarisation effects on sub-channel power and correlation are rarely seen from a data oriented perspective. In this chapter, the term ‘polarisation effects’ is used to describe such kind of signal variations from a statistical point of view. A novel approach is used to investigate these variations with respect to frequency and receiver orientation, and the results obtained on sub-channel power and correlation are used to construct a new polarisation diversity scheme. The tools, methods and analytical of results of spatial and polarisation effects are the contents of this chapter.*

## 5.1 Introduction

In radio communications, polarisation is a basic characteristic of antennas which has profound effects on the reception of signals. Handling these effects appropriately leads to better system performance but the literature on the potential exploits of polarisation is scarce, especially for indoor environments. The most often cited work that relates to polarised channel models are those of [70, 71, 72], but these works assume the classic outdoor macro-cell scenario. The data used in this work were measured using antenna arrays consisting of dual polarised elements, both in the Tx and Rx. This gives rise to 4 potential combinations of Tx-Rx polarisation settings, providing an opportunity to conduct a systematic empirical study on the effects of polarisation in indoor environments. Such study will build on the work of the previous chapters by incorporating the effects of polarisation alongside that of T-R separation, antenna properties, and environmental factors to form a more complete system of propagation prediction.

Antennas are typically either horizontally polarised (H for short in the following text), where the electric field of the antenna varies in amplitude along a horizontal plane, see Figure 5-1; or vertically polarised (V for short in the following text), where its electric field varies in amplitude along a vertical plane. Naturally, H and V polarisations are orthogonal to each other; both are linear and have signals with fixed polarisation direction. Slant polarized antennas [73], where planes of vibration are not perpendicular or parallel to the ground, works on the same principle: linear with fixed direction. They are usually combined in orthogonal pairs, e.g.  $\pm 45^\circ$  [74], for diversity schemes. Since orthogonally polarised slant pairs can be related to HV cross polarisation, any findings on HV pairs will have relevance to orthogonal slant pairs. Finally, circular polarisation, where the direction of the polarisation rotates about the wave's propagation axis, also exists and works differently in principle to the previously mentioned polarisations.

However, due to the lack of data and their relative rarity, they will not be considered in this work.

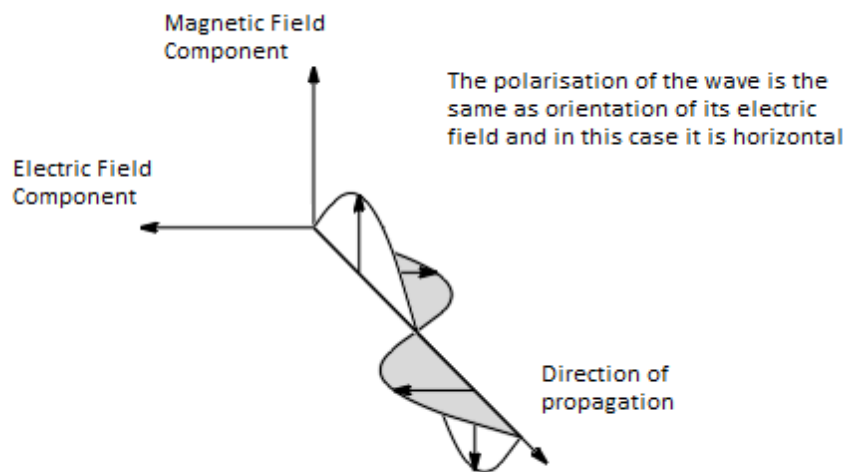


Figure 5-1: Propagation of a radio wave

Antennas will transmit signals with polarisations matching their own, and have best reception for signals of the same polarisations, thus the effects of polarisation can be seen in both sides of the link. On the transmitting side, the signal power distributes on the surface of a sphere with the transmitting antenna at the centre, the strength is related to the direction of lines that are normal to the sphere. On the receiving side, the received power will be related to both the strength and the polarisation of the arriving signal. Theoretically, if everything is aligned perfectly such that the polarisation of an arriving signal is orthogonal to the receiving antenna, then the receiver will not pick up anything from that signal. In practice, a polarisation difference of  $90^\circ$  will result in an attenuation factor of 10 to 30 dB.



Radio waves travelling in free-space tend to maintain the polarisation it had at launch. However, if a signal undergoes attenuation due to the existence of obstacles along the propagation path, as happens frequently in indoor propagation, the polarisation may shift away from the original direction. This added complexity makes the received signal strength more difficult to predict, but if the effects can be isolated and studied any findings may prove significant. The Lund measurement data presents such an opportunity to isolate the effects of polarisation and since the data was obtained empirically, an empirical approach into the investigation is the most sensible choice.

This section presents the background on antenna polarisation, their impacts on signal propagation, and a potential opportunity to investigate this impact. The remaining parts of this chapter will present the theoretical and empirical aspects of the investigation and related findings. Firstly, in section 5.2, the basic considerations and the methodologies will be detailed and explored. This is followed by sections 5.3 and 5.4 which present the main findings of the investigation in regard to polarisation effect on received signal. Section 5.5 explores the potential implications of the finds in terms of polarisation diversity. Finally section 5.6 provides a summary for the works presented in this chapter, in which further discussions and conclusions are made.

## 5.2 Considerations and Methodologies

The basic consideration of this chapter is that spatial orientation and polarisation may have systematic influences on measured signal value which could be detected statistically given sufficient sample size. The data used in this study contains, at each measurement point, a channel transfer matrix of dimension  $10 \times 81 \times 4096$ ; where the dimensions represent temporal snapshots, frequency samples, and MIMO channels respectively. Each one of the 4096 channels can have 1 of 4 possible polarisation settings: VV, VH, HV and HH, where the letters specifies the polarisation of the receiver element and transmitter element respectively. For example, HV represents a channel with horizontally polarised receiver element and vertically polarised transmitter element. All 4 polarisation settings contain exactly 1028 channels so the data can be split accordingly into 4 matrices of dimension  $10 \times 81 \times 1028$ .

Furthermore, it is unclear how the effects of frequency and antenna orientation will interact with that of polarisation. Taking this into consideration, two further classifications of the data were conducted in an effort to isolate polarisation. Each of the 4 polarisation matrices was rearranged: firstly according to the 81 frequency sample points, and secondly corresponding to the 16 columns on the receiver array. Under the first classification, with frequency separated, the sample size that remains for each subset is  $10 \times 1024 = 10240$ , all of which are data collected under the same frequency and polarisation setting. For the second classification, with receiver antenna orientation fixed, the  $16 \times 64$  MIMO channels reduces to  $16 \times 4$  for each orientation. This, along with 10 snapshots and 81 frequencies, gives each sample a size of  $10 \times 81 \times 16 \times 4 = 51840$ . In both cases, the sample size is large enough to obtain reliable statistical results.

With this in mind, from a single channel matrix, a total of 8 rearranged matrices are produced. The 4 matrices of size  $10240 \times 81$  related to frequency are denoted

by  $\mathbf{v}\mathbf{v}\mathbf{X}$ ,  $\mathbf{v}\mathbf{h}\mathbf{X}$ ,  $\mathbf{h}\mathbf{h}\mathbf{X}$  and  $\mathbf{h}\mathbf{v}\mathbf{X}$  corresponding to their polarisation setting while the other 4 matrices of size 51840 x 16 related to Rx orientation are denoted by  $\mathbf{v}\mathbf{v}\mathbf{Y}$ ,  $\mathbf{v}\mathbf{h}\mathbf{Y}$ ,  $\mathbf{h}\mathbf{h}\mathbf{Y}$ ,  $\mathbf{h}\mathbf{v}\mathbf{Y}$  similarly. Furthermore, these matrices contain the complex signal values from which the amplitude and phase can be separated. Since both have clear meanings in Physics, there is an opportunity to investigate them individually which may produce deeper insight into the effects of polarisation. In following text,  $\mathbf{v}\mathbf{v}\mathbf{A}_x$ ,  $\mathbf{v}\mathbf{h}\mathbf{A}_x$ ,  $\mathbf{h}\mathbf{h}\mathbf{A}_x$ ,  $\mathbf{h}\mathbf{v}\mathbf{A}_x$  denotes the amplitude matrices derived from  $\mathbf{v}\mathbf{v}\mathbf{X}$ ,  $\mathbf{v}\mathbf{h}\mathbf{X}$ ,  $\mathbf{h}\mathbf{h}\mathbf{X}$ ,  $\mathbf{h}\mathbf{v}\mathbf{X}$ ; Similarly,  $\mathbf{v}\mathbf{v}\mathbf{B}_x$ ,  $\mathbf{v}\mathbf{h}\mathbf{B}_x$ ,  $\mathbf{h}\mathbf{h}\mathbf{B}_x$ ,  $\mathbf{h}\mathbf{v}\mathbf{B}_x$  denotes the phase matrices. There also are amplitude matrices  $\mathbf{v}\mathbf{v}\mathbf{A}_y$ ,  $\mathbf{v}\mathbf{h}\mathbf{A}_y$ ,  $\mathbf{h}\mathbf{h}\mathbf{A}_y$ ,  $\mathbf{h}\mathbf{v}\mathbf{A}_y$  derived from  $\mathbf{v}\mathbf{v}\mathbf{Y}$ ,  $\mathbf{v}\mathbf{h}\mathbf{Y}$ ,  $\mathbf{h}\mathbf{h}\mathbf{Y}$ ,  $\mathbf{h}\mathbf{v}\mathbf{Y}$  and corresponding phase matrices  $\mathbf{v}\mathbf{v}\mathbf{B}_y$ ,  $\mathbf{v}\mathbf{h}\mathbf{B}_y$ ,  $\mathbf{h}\mathbf{h}\mathbf{B}_y$ ,  $\mathbf{h}\mathbf{v}\mathbf{B}_y$ .

In terms of methodology, statistical analysis is a powerful tool to search for various statistics related to the effects of polarisations. To detect and quantify these effects, two separate perspectives were employed, namely ***distribution analysis*** and ***correlation analysis***. The distribution study focuses on the how the various properties of the amplitude and phase distributions are affected by changes in antenna polarisation, and whether any underlying patterns exist. The main points of comparison will be the centre, shape, and statistics such as the mean, median and variance of the distributions. A shortfall of this approach is that statistics such as the mean, median and variance depends only on elements in a collection and not their order, whilst the data in this study are ordered in matrices. For example, an individual column of  $\mathbf{v}\mathbf{v}\mathbf{A}_x$  contains the amplitudes derived from measured signals of a particular frequency and polarisation across all the different positions; from this sample, the distribution of the amplitudes and associated statistics can be drawn. However, two separate distributions drawn from different columns of  $\mathbf{v}\mathbf{v}\mathbf{A}_x$  could numerically have the same mean and variance. Thus, a different approach is needed when comparing properties of data where their elements need to be viewed in order. This is why a second perspective, namely the correlation analysis, is also employed to study the data. Details related to the

correlation analysis will be outlined later; first, the issues relating to the distribution study is described.

### **5.2.1 Methodological issues relating to Distribution Analysis**

For this particular study, the procedure of analysis involves the following steps:

- Evaluating the data distributions column-wise for amplitude and phase matrices;
- Looking at the statistical median, 1<sup>st</sup> / 3<sup>rd</sup> quartiles, and 5% / 95% percentiles;
- Comparing and displaying all the distribution parameters using statistical tools;
- Testing column mean statistic of each data matrix against the overall matrix mean;
- Testing the amplitude and phase column distributions using selected statistical tools.
- Contrasting the results corresponding to the 4 different polarisation settings;
- Summarising the test results.

One of the statistical tools mentioned in the bullet points is Boxplot [75, 76], which presents data distributions in a simplified manner and illustrates a number of distributions in a single plot, including the median, 1<sup>st</sup>/ 3<sup>rd</sup> quartiles, and 5% / 95% percentiles. Other methods used in this section include Q–Q plot [77, 78] and Shewhart control chart [79, 80].

When testing column means against the associated matrix mean, the Central Limit Theorem can be fully utilised, because the number of matrix rows is sufficient large

(10240 for frequency data matrices and 51840 for receiver orientation data matrices). Take matrix  ${}_{vv}A_x$  for example, let:

$C_i$  ( $i= 1,2,...,81$ ) denote the  $i^{\text{th}}$  column vector of  ${}_{vv}A_x$ ;

$\overline{C}_i$  ( $i= 1,2,...,81$ ) denote the  $i^{\text{th}}$  column mean of  ${}_{vv}A_x$ ;

$\overline{\overline{C}}$  denote the  ${}_{vv}A_x$  matrix mean;

Let  $m = 10240$  and  $n = 81$ , based on the central limit theorem,  $\overline{C}_i \sim N(\overline{\overline{C}}, \sigma_c^2)$ , where  $\sigma_c^2$  is formulated as equation [5.1]

$$\sigma_c^2 = \frac{\sum_{i=1}^n \sum_{j=1}^m (C_{i,j} - \overline{C}_i)^2}{(m \times n - n - 1) \times m} \quad [5.1]$$

By introducing the formulation  $z_i = \frac{(\overline{C}_i - \overline{\overline{C}})}{\sigma_c}$ ,  $z_i \sim N(0,1)$  can be derived, the classical standard normal test can be applied. The null hypothesis  $H_0$  is that the mean of a given column is the same as the mean of the matrix, whereas the alterative hypothesis  $H_1$  is that the mean of a column are different from the mean of the matrix.

In order to summarise the effects of different polarisations and their associated interactions with frequency, the test results from all 4 polarisation matrices are shown together in the same process control chart [81, 82]. Here, the x-axis denotes the frequency index while the y-axis displays the corresponding values of  $\overline{C}_i$  and  $\overline{\overline{C}}$ . Based on the matrix mean  $\overline{\overline{C}}$  and variance  $\sigma_c^2$ , three horizontal lines are placed at:

$$y = \overline{\overline{C}}, \quad y = \overline{\overline{C}} + 3 \sigma_c, \quad y = \overline{\overline{C}} - 3 \sigma_c$$

The first line is called the central control line (CLC), while the other two lines are called the upper (UCL) and lower control lines (LCL) respectively. The values of the column means  $\overline{C_i}$  ( $i= 1,2,...,81$ ) will be presented as data points on the chart. Making use of such a control chart, any significant differences that arise due to polarisations can be easily spotted by the presence of outliers which are the data points located outside of the upper and lower control lines. Figure 5-2 shows an example illustration of a control chart that has 2 clear outliers.

A further methodological detail is that in distribution test, the amplitude matrices and phase matrices are processed using different methods. This is mainly due to the difference between the amplitude and phase distributions. The signal phase at the Tx generally follows an uniform distribution  $U(-\pi, \pi)$ , and changes in the distribution form at the Rx due to propagation factors can be detected by applying the empirical Kolmogorov-Smirnov test [83, 84, 85] on the columns of the phase matrices to highlight any potential effects of polarisation. In contrast, the amplitude distribution is far more diverse, it is not practical to test each of these distributions against the data one by one. A better approach would be to test side by side the corresponding columns from two different polarisation matrices; this gives a direct way to reveal any consequences of different polarisation settings. For this purpose, the non-parametric Wilcoxon signed rank test [86, 87] is a suitable candidate.

The Wilcoxon signed rank test will show whether sampling signal amplitudes from two different polarisation settings are equivalent to sampling from two different distributions. The Kolmogorov-Smirnov test will reveal whether polarisation setting would have a statically significant effect on the phase distributions inherent within the data. With this last detail, the methodological issues related to the distribution study have been outlined. The next subsection will discuss the details of the correlation study.

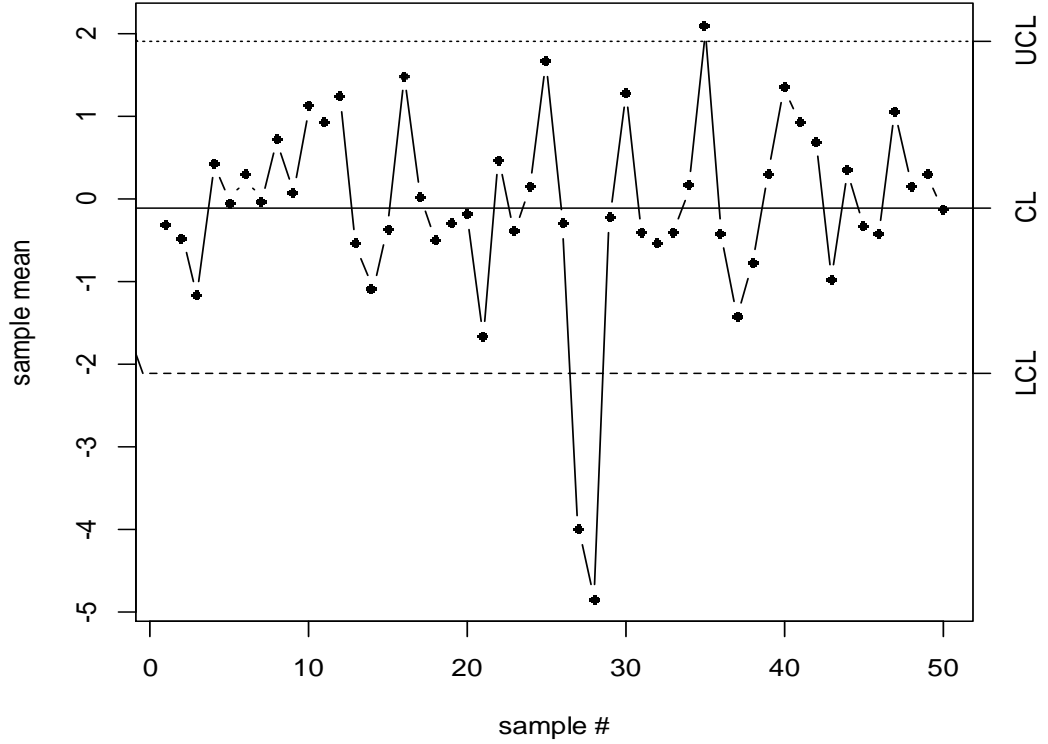


Figure 5-2: An illustration of the control chart.

### 5.2.2 Methodological Issues Relating to Correlation Analysis

As revealed at the beginning of in section 5.2, separate amplitude and phase matrices have been constructed for each polarisation. Unlike the original signal matrices, the elements of amplitude and phase matrices are non-complex values, meaning that the correlation of two data vectors can be evaluated by the Pearson product-moment correlation coefficient [88, 89]. That is, if  $\mathbf{U}$  and  $\mathbf{V}$  denote the two length  $l$  sample data vectors, and  $r$  the correlation coefficient of  $\mathbf{U}$  and  $\mathbf{V}$ , then we have:

$$r = \frac{\sum_{i=1}^l (u_i - \bar{u})(v_i - \bar{v})}{\sqrt{\sum_{i=1}^l (u_i - \bar{u})^2 \sum_{i=1}^l (v_i - \bar{v})^2}} \quad [5.2]$$

For the study in this chapter, columns of polarisation matrices are evaluated against each other in pairs. The pair of columns can be drawn from the same polarisation matrix, or 1 of the 3 differently polarised matrices, thus a total of 10 combinations of pairs of polarisation settings is possible. A correlation matrix can be computed for each pair of polarisation settings resulting in 10 different correlation matrices. 4 of these matrices are generated from evaluating pair-wisely the columns of the same polarisation matrix and will thus be symmetrical. The other 6 correlation matrices are calculated from comparing columns of different polarisation matrices, and will unlikely to be symmetrical.

The correlation matrices will indicate the degree of correlation between the columns, each column contains the complete collection of sample data of a particular frequency, polarisation and receiver orientation. If the columns are unrelated, the data will be random with respect to each other and the correlation matrix will show a random collection of values close to zero, with no observable patterns. However, if the columns are in fact related, for example, by certain underlying physical principles, a pattern would be observed. Therefore, observing and comparing data collected from the same measurement position is a simple and direct way to reveal and evaluate any polarisation effects there might be. In addition, comparing the correlation patterns observed between data from different measurement positions is a way to gain a perspective on any existing polarisation effects that are consistent across different measurement positions. A sensible approach for undertaking these comparisons is to look at the statistics which may be termed as the correlation of correlation patterns. This can be more explicitly stated as the operation that firstly reshapes a correlation matrix into a vector by concatenating its columns, and then compute the correlation coefficients between two such concatenated vectors of data measured at different positions.



Finally, an important point in correlation analysis is that correlation coefficients are statistics estimated from sampling data; their significance needs to be evaluated prior to any statistical deductions. Without proper testing, any conclusions drawn from correlation coefficients are not meaningful. For this reason, the correlation coefficients estimated are also tested by the  $t$ -test [90, 91, 92], which requires the assumption that the data distributions are approximately Normal. Since the distribution of signal power in Watts is approximately Lognormal, it is reasonable to assume the distribution in dBm is approximately Normal. A brief description of the  $t$ -test method is as follows: let  $r$  denote the correlation coefficient estimated from two length  $n$  vectors, the corresponding  $t$  statistic can be constructed from  $r$  as shown in formula [5.3]. Here  $t$  follows a degree  $n-2$  freedom student  $t$ -distribution [93, 94], and the significance of  $r$  is also evaluated based on this distribution.

$$t = r \cdot \sqrt{\frac{n-2}{1-r^2}} \quad [5.3]$$

This section discussed the issues relating to the methodologies that will be employed in the studies carried out in the rest of this chapter. The two main angles of approach will be distribution analysis and correlation analysis. The next section presents the findings of distribution analysis.

### 5.3 Polarisation Effects on Signal Distribution

In the previous section, the methodology for exploring the effects of polarisation was outlined; this section presents the findings of the distribution analysis. This part of the study focuses on looking at the amplitude and phase distributions of the measured signal across 81 frequencies and 16 receiver orientations, for each of the 4 polarisation settings, to see if any observable patterns are present. The 50MHz bandwidth is evenly divided into 80 subcarrier bands of 625 kHz. Since the antennas were either in fixed positions or moving slowly during the measurements it is assumed that the subcarrier bandwidth is much greater than the Doppler spread  $f_D$ , as well as the reciprocal of the coherence time  $T_C$ . The next subsection presents the results of polarisation effects on amplitude distribution in association with frequency.

#### 5.3.1 Polarisation effects on amplitude distribution in relation to frequency

As mentioned in section 5.2, from each measurement position the data contained in the channel transfer matrix is reorganised to produce 4 amplitude matrices  $_{vv}A_x$ ,  $_{vh}A_x$ ,  $_{hh}A_x$ ,  $_{hv}A_x$ , and 4 phase matrices  $_{vv}B_x$ ,  $_{vh}B_x$ ,  $_{hh}B_x$ ,  $_{hv}B_x$ , all with dimensions of  $10240 \times 81$ . The rows of these matrices correspond to sample obtained from different channels at various times, whilst the columns corresponds to 81 frequency samples evenly distributed in a 50 MHz bandwidth around 2.6GHz. For any given column, the 10240 data points represent the complete sample of data obtained from a position with a particular polarisation and frequency, i.e. it contains data from all channels and time points. For 120 measurements where the Rx was moving, the 10240 data points are chosen from fixed time slices within the data sequence.

First, let's focus on  $vv\mathbf{A}_x$ ,  $vh\mathbf{A}_x$ ,  $hh\mathbf{A}_x$  and  $hv\mathbf{A}_x$  to see what polarisation effects show up in the amplitude distributions. Figure 5-3 shows the boxplot drawn based on amplitude matrices measured from position number 5 in corridor 2. The plot has 4 panels corresponding to the 4 polarisation settings and on each panel 81 vertical 'boxes' display statistics of the amplitude distributions across the frequencies domain.

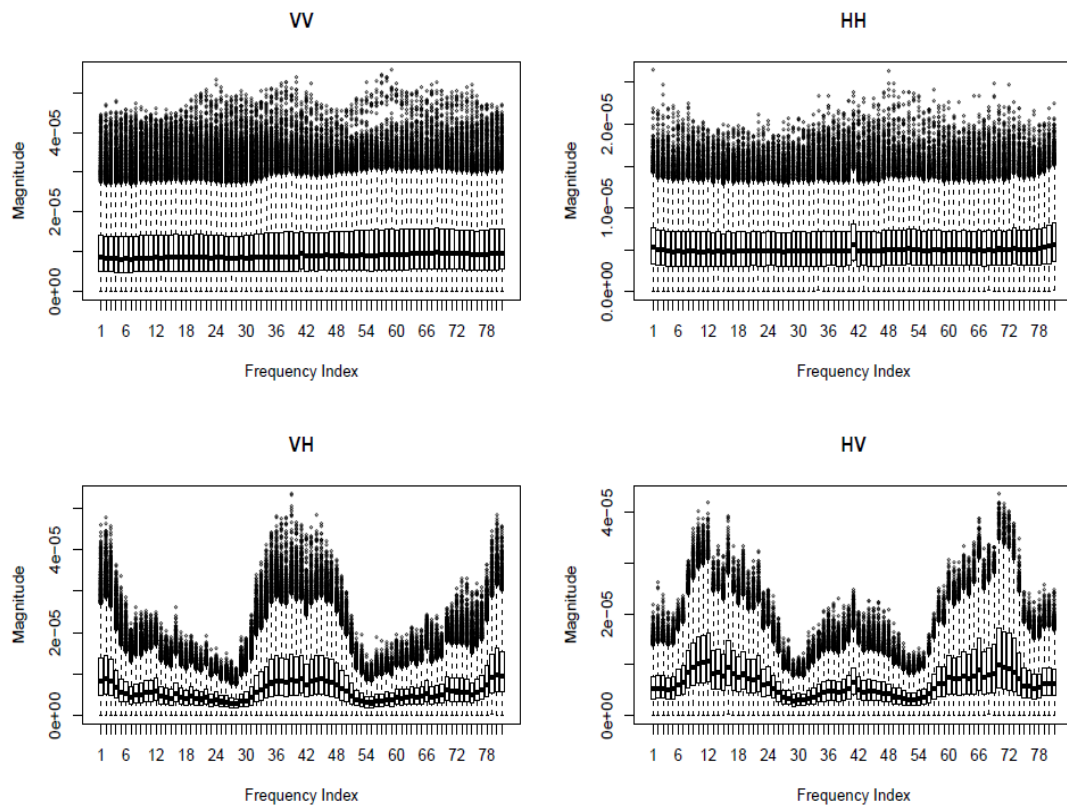


Figure 5-3: Amplitude distribution of the 4 polarisation settings across 81 frequencies

The presence of polarisation effects can be clearly seen. Firstly, for VV and HH settings the centres of amplitude distributions across the frequency domain form almost a flat line: indicating that the amplitudes, and in turn the received signal strength, do not vary greatly across the frequency domain. In contrast, the mean received signal strength for VH and HV settings varies by as much as 12 dB across the frequency domain, with the variation pattern somewhat periodic. This periodic variation is the results of *Polarisation Fading*, which is caused by changes in the polarisation during the propagation of cross-polarised EM waves [95].

The co-polarised channels also show very consistent quartiles; whereas the quartiles for cross-polarised channels are really narrow at certain frequencies and wide at other frequencies. Hence, the effects of polarisation is profound on the amplitude distribution of received signal. The consistency of co-polarised channels is great for prediction and planning. The periodic variations of signal strength in cross-polarised channels can also be utilised in beneficial ways by employing the appropriate polarisation diversity schemes, for example, sub-channels with central frequencies located around distinct peaks can be picked out and will have good reception and experience less interference than normal around the intervening frequencies. More detailed exploration of polarisation diversity schemes will be presented later in the chapter.

Although boxplot shows that the amplitude distributions are skewed, it does not offer more detailed information about the probability density. Figure 5-4 shows the density histogram of the amplitude distribution for HH polarisation at 2.575 GHz. The three fitted PDF curves representing the Lognormal ( $\mu$ : -12.21,  $\sigma$ : 0.6279) Weibull ( $\lambda$ : 6.570e6,  $k$ : 2.0426) and Rayleigh distributions ( $\sigma$ : 4.702e-6) are added to the histogram. The Weibull distribution appears to fit the data better than the other two distributions, which is not surprising as it is able to supply more optional parameters by combining scale and shape two distribution parameters.

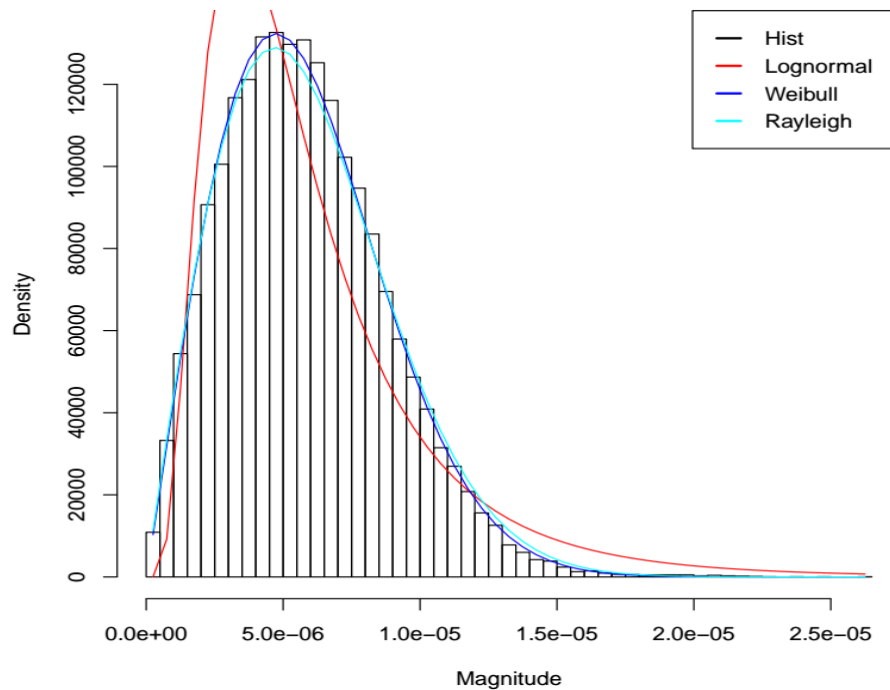


Figure 5-4: Histogram of signal amplitude and fittings to three distributions

Figure 5-5 shows a control chart for identifying the existence of significant polarisation effects. The data points are the mean amplitudes across the frequency domain. The horizontal lines are control lines: solid lines mark the central control lines, dotted lines mark the upper control lines and dashed lines mark the lower control lines. The 4 colours correspond to the different polarisation settings: red for VV, green for VH, orange for HH and black for HV. For given a polarisation, if the dispersion of the amplitude data is purely random, the corresponding sample means should scatter between the upper and lower control lines. If any data points lay outside these boundaries, frequency associated dispersion will most likely be the cause.

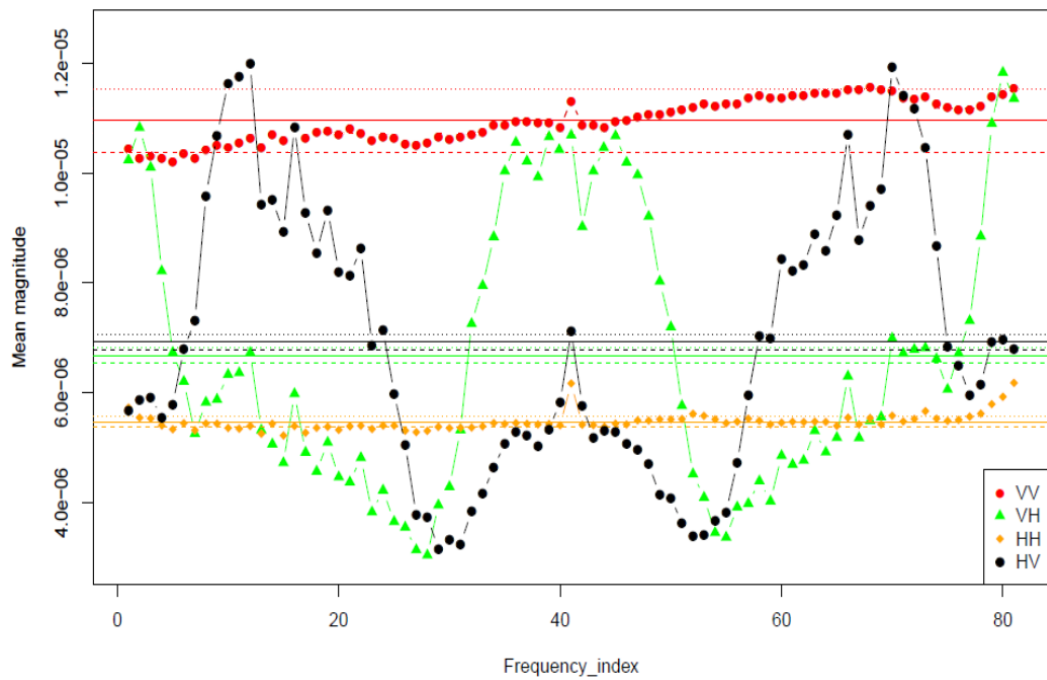


Figure 5-5: Variation of amplitude mean across the frequency domain.

The chart provides an informative picture about relationships between the amplitude distribution and frequency, especially given different polarisation settings:

- The co-polarised channels do not suffer from frequency selective polarisation fading, thus the amplitude of co-polarised signals (HH and VV) are largely unaffected by frequency.
- The amplitudes of cross-polarised signal (HV and VH) varies much more with frequency, this is most likely caused by polarisation fading, which is typically associated with cross polarised waves [95].
- Due to the polarisation fading, the peak signal strength for the cross-polarised channels are higher than that co-polarised channels. This can be exploited by polarisation diversity which will be explored in later section.
- Overall, the mean signal strength is the highest for VV setting and lowest for HH, with a difference of around 6 dB between the two. This is most likely caused by a combination of low antenna heights, which typically results in stronger vertically polarised signals for the indoor environment [96], and Brewster's angle phenomenon affecting the propagation of horizontally polarised waves in indoor environments [97].
- The mean signal strength for the HV and VH settings are very close, in fact within 0.1 dB of each other, although their values differ by more than 3 db at over 75% of the frequency points. This is due to the periodical nature of the cross polarisation fading particular to the system. The HV and VH signals exhibit constructive and destructive interference and are out of phase with each other.

### 5.3.2 Polarisation effects on phase distribution in relation to frequency

The investigation into phase matrices  $_{vv}\mathbf{B}_x$ ,  $_{vh}\mathbf{B}_x$ ,  $_{hh}\mathbf{B}_x$  and  $_{hv}\mathbf{B}_x$  was conducted in a similar way as the previous subsection. First, boxplot is used to contrast the effects of the polarisation settings on data distribution. Figure 5-6 show clearly that polarisation does not affect the phase distribution in the same way it affects the amplitude distribution, as the phase distributions are virtually identical across the 4 different polarisations. The central black line in each sub figure shows the mean signal phase, it can be seen that in all cases the phase distributions are symmetrical around a mean of zero. In addition, the figure also show that the 1<sup>st</sup> quartiles, represented by the vertical bars, are at  $\pm 1.5$  radians for all polarisations.

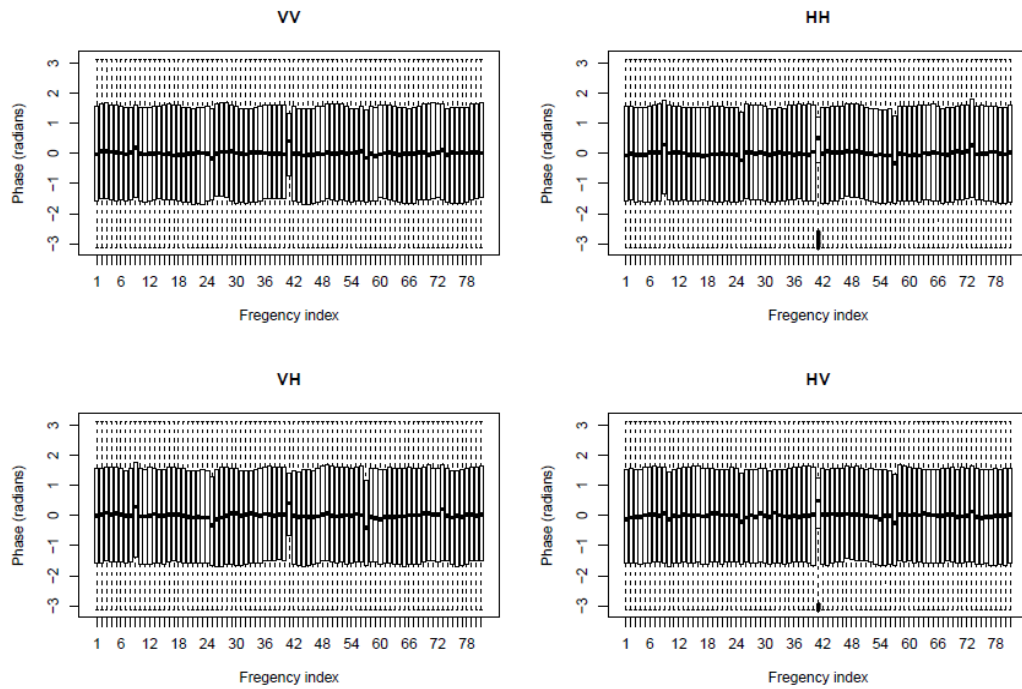


Figure 5-6: Phase distribution of the 4 polarisation settings across 81 frequencies



Further observations reveals that at most frequency points the phase distribution is not only symmetrical but uniform between  $-\pi$  and  $\pi$ , which suggests that the signal came from a complex Gaussian process. The fact is, if  $Z = X + jY$  is a complex Gaussian process with zero mean ( $\mu = 0$ ) and zero relation matrix ( $C = 0$ ), then the variable  $\frac{Y}{X}$  follows a Cauchy distribution, and furthermore, if  $\varphi$  represents the phase variable associated with  $Z$ , i.e.  $\tan \varphi = \frac{Y}{X}$ , then  $\varphi$  follows a uniform distribution [98]. Actually, In the case of  $\mu = E[Z] = 0$ , and  $C = E[(Z - \mu)(Z - \mu')^*] = 0$ ,  $Z$  is known as “circularly symmetric” [99], and its density function depends only on its magnitude  $|Z|$  and not its argument. As such, the magnitude will have a Rayleigh distribution whereas the argument will have the uniform distribution  $U(-\pi, \pi)$  [100]. The phase data at 5 particular frequency points show obvious shift of distribution centre away from zero, and the intervals between the 5 frequencies are all exactly the same, namely 10MHz. As it happens, the central frequency point 2.6 GHz is one of the five frequencies. The other four frequencies are 2.58, 2.59, 2.61 and 2.62 GHz. The signal phase distribution at these 5 special cases may be related to certain nature of signal propagation observed in this study, or it might be caused by the equipment.

The most likely cause of these outliers at the 5 particular frequency is from to errors introduced during calibration of the antenna arrays. According to chapter 2 of [101], due to the inherent limitations of the calibration procedure, a number of assumptions about the beam patterns are made in order to reduce the computation complexity of the estimation process. However, in practice, violation of one or more of the assumptions is nearly always the case with practical arrays.

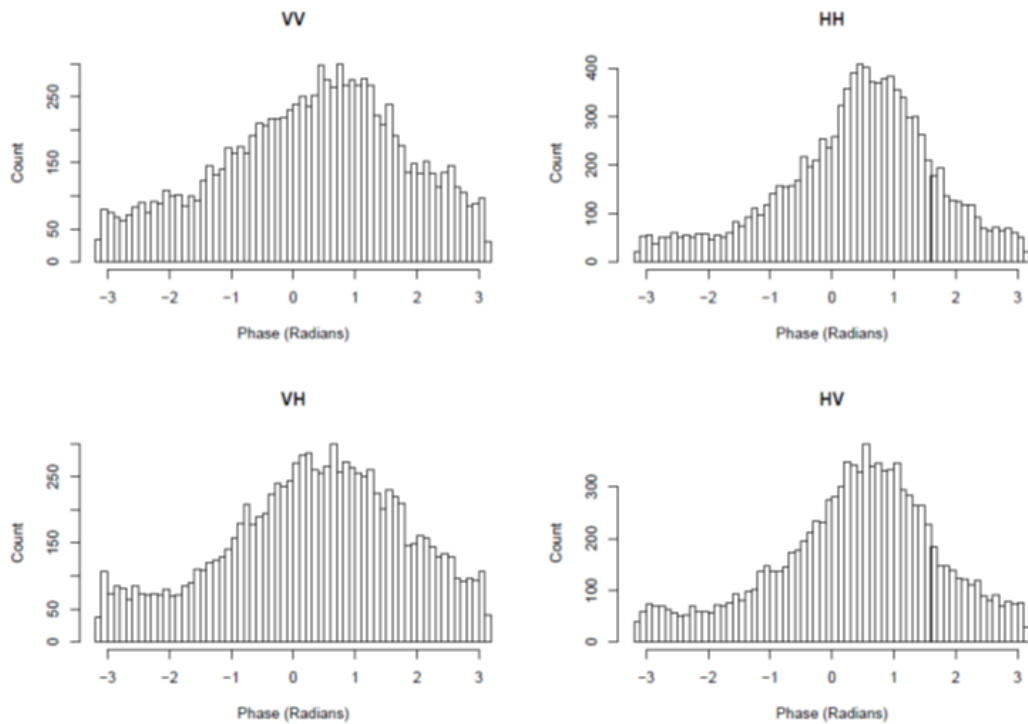


Figure 5-7: Histogram of phase distribution at 2.6 GHz, showing a non-uniform distribution

As can be seen in Figure 5-7, the phase distributions at the 5 special case frequencies are non-uniform. A possible reason of the non-uniform phase distribution is that the data were drawn from a complex Gaussian process with non-zero mean. In order to demonstrate the validity of this explanation, a simulation is conducted where a million values are randomly drawn from a complex normal distribution with non-zero mean. The result of the simulation, shown in Figure 5-8, bears strong resemblance to the phase distributions shown in Figure 5-7. However, it is difficult to explain the periodical appearance special frequency points in such discrete and regular patterns. It would be interesting to know what physical mechanisms might be behind such phenomena and what consequence will emerge. Though no complete answer is given, this study does reveal certain relationships between the phase and magnitude distributions and correlation between signals of different frequencies. These will be presented later in this chapter.

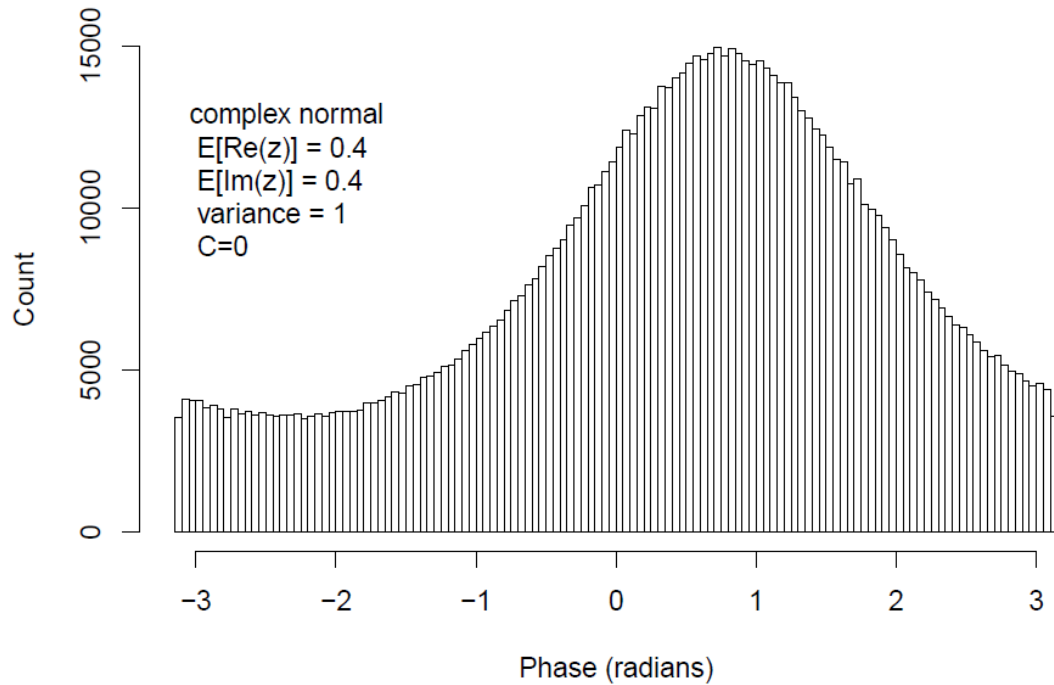
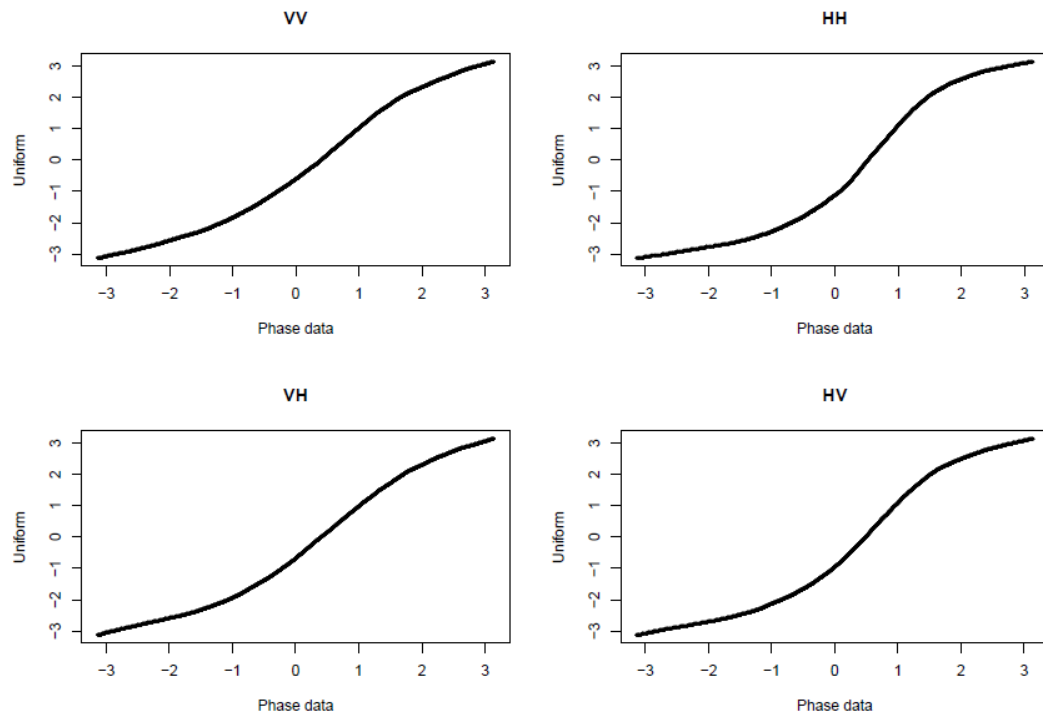


Figure 5-8: Simulated phase distribution with non-zero mean

The non-uniformity of the signal phase distribution at specific frequency can also be visualised by q-q plot, on which the quartile of phase data is contrasted against the CDF of the uniform distribution  $U(-\pi, \pi)$ . On the q-q plot, if the data points forms an approximate straight diagonal line, it means the data is uniform distributed, otherwise the data distribution is not uniform. Figure 5-9 shows the q-q plot of the uniform distribution  $U(-\pi, \pi)$  contrasted against the distribution of phase data used to generate Figure 5-7. The plot shows an italic S-shaped curve confirming the non-uniformity of the phase distribution.



**Figure 5-9: q-q plot of signal phase data at frequency 2.6 GHz and uniform CDF**

In order to draw a whole picture about the relationship between the phase distribution and signal frequency, the control chart approach was applied to the phase data, see Figure 5-10. In this figure, the data points are colourized as red, green, black and orange to represent four polarisation settings: VV, VH, HH and HV. According to this chart, the four polarisations do not show significant difference.

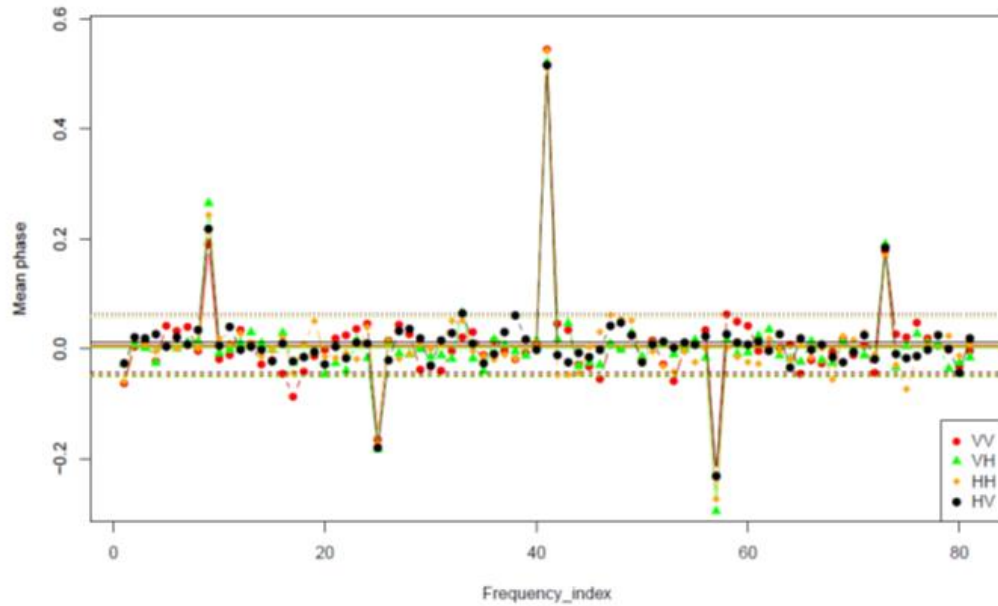


Figure 5-10: Variation of phase mean across the frequency domain.

From the figure, artefacts at 5 particular frequencies are clearly noticeable, this is most likely to be caused by errors introduced during the calibration of the antenna arrays. According to chapter 2 of [101], due to the inherent limitations of the calibration procedure, a number of assumptions about the beam patterns are made in order to reduce the computation complexity of the estimation process. However, in practice, violation of one or more of the assumptions is nearly always the case with practical arrays.

To investigate the outliers further, the Kolmogorov–Smirnov test is applied to the signal phase across all the measurement positions and focuses on the 5 frequencies which correspond to outliers in Figure 5-10. The phase data is tested against the uniform distribution  $U(-\pi, \pi)$  and produces rates of non-uniformity of the phase distribution at the five specific frequencies as follows: 98.7% for VV setting, 100% for VH setting, 98.7% for HH setting and 99% for HV setting.

### 5.3.3 Polarisation effects on amplitude distribution in relation to Rx orientation

This section studies the amplitude matrices  $_{vv}A_y$ ,  $_{vh}A_y$ ,  $_{hh}A_y$ ,  $_{hv}A_y$ , and the phase matrices  $_{vv}B_y$ ,  $_{vh}B_y$ ,  $_{hh}B_y$ ,  $_{hv}B_y$ , associated with receiver orientation. Each one of these matrices has dimensions of  $51840 \times 16$ . The rows of these matrices correspond to sample obtained from different channels at various frequency and time points, whilst the columns correspond to 16 receiver orientations.

Figure 5-11 shows the amplitude distribution of the 4 polarisation settings across 16 receiver orientations. In all polarisation settings, the received signal strength traces a curve similar to a sine wave across the receiver orientations. This can be expected as the antenna elements of the 16 receiver orientations are arranged evenly on a ring, making a complete  $360^\circ$  circle. The variation in signal strength is most pronounced in VV polarisation and the shape shows greatest resemblance to the sine wave across a  $2\pi$  domain.

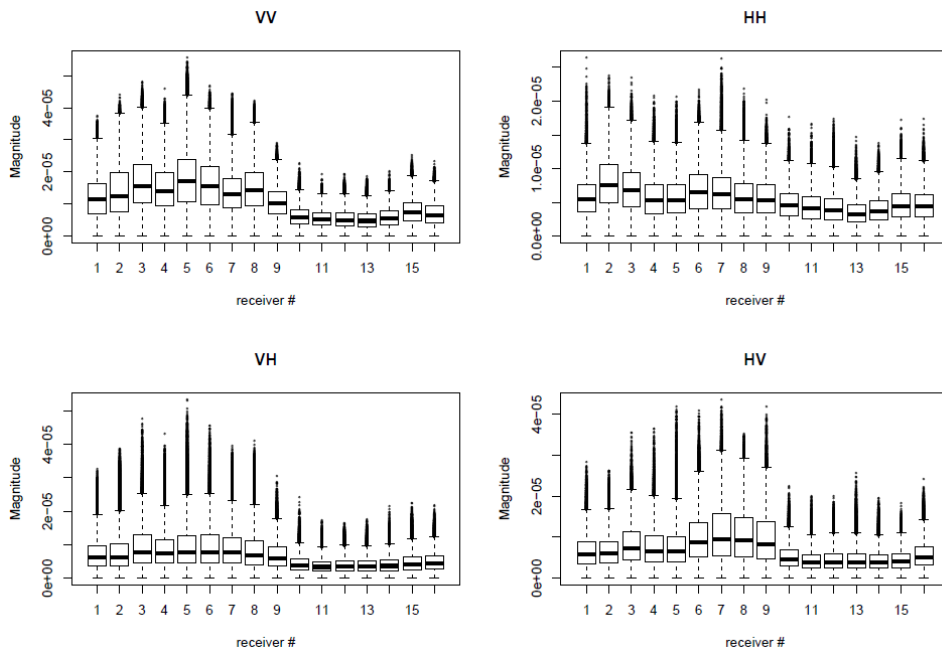


Figure 5-11: Amplitude distribution of the 4 polarisation settings across 16 Rx orientations

More detailed information about the amplitude distribution for a specific polarisation and receiver orientation can be provided by histogram and fitted density curves. Figure 5-12 shows an example of such a histogram. In this case, fit to Weibull distribution provides the best fit.

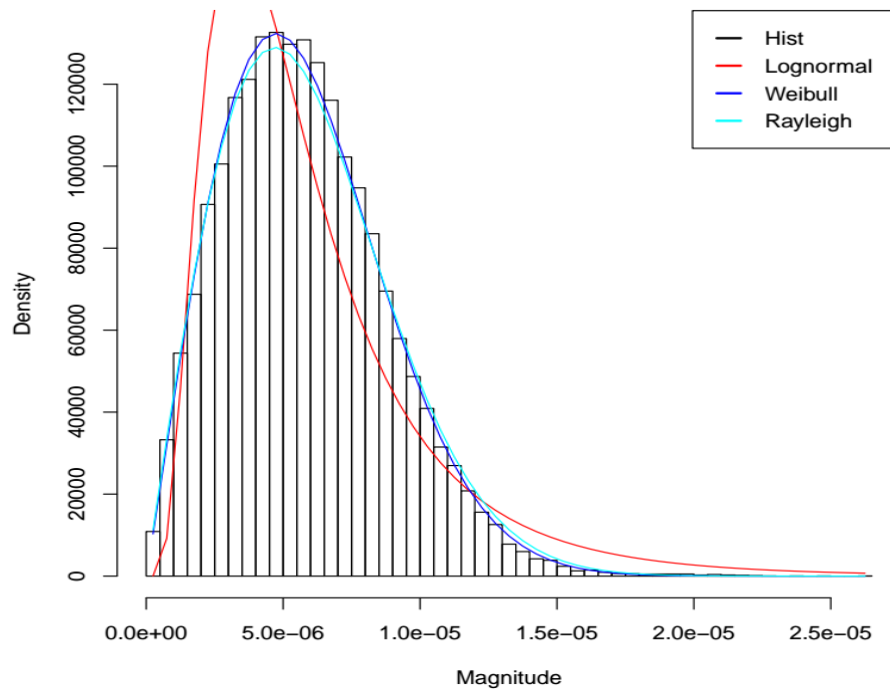
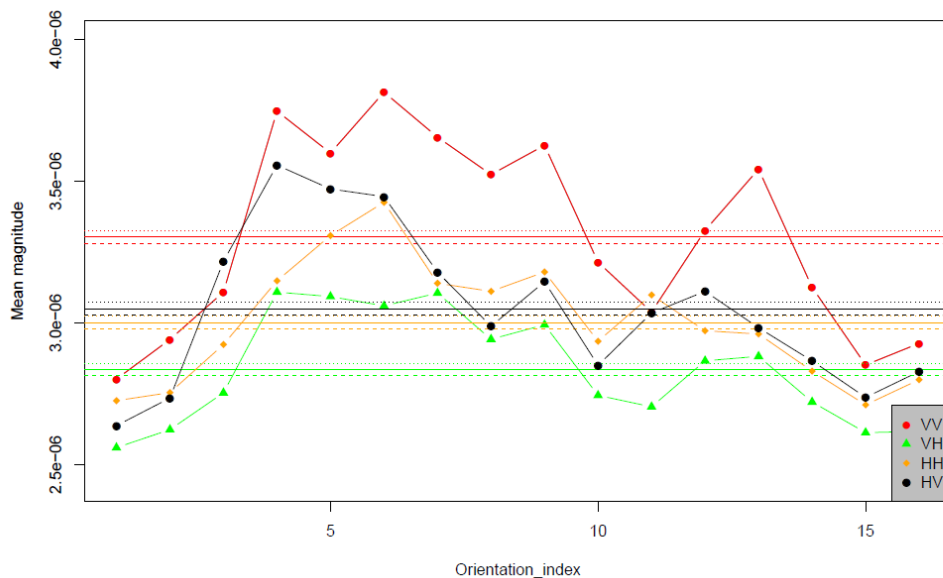


Figure 5-12: Histogram of signal amplitude and fittings to three distribution densities

Figure 5-13 provides an informative picture about the impact that the receiver orientation has on the amplitude distribution of the received signal across the 4 polarisation settings. The patterns of variation in the mean of amplitude distributions are similar for all 4 polarisation settings. The magnitude of variation is at least one order of magnitude greater than width of the control zone; this is another universal character across the different polarisations.



**Figure 5-13: Variation of amplitude mean across the 16 receiver orientations.**

The chart also agrees with Figure 5-5 about the relative signal strength across the different polarisation settings: VV having the highest average received signal strength, HH having the lowest while VH and HV are very close to each other. This is because sub-channels of dual-polarised MIMO channel are not identically distributed. They differ on many aspects including received power, correlation and cross polarisation discrimination. Phenomena such as depolarisation of the wave through reflections and scattering from indoor obstacles and polarisation fading of cross-polarised waves are the main causes of this.



### 5.3.4 Polarisation effects on phase distribution in relation to Rx orientation

The effects polarisation and receiver orientation on phase matrices  ${}_{vv}\mathbf{B}_y$ ,  ${}_{vh}\mathbf{B}_y$ ,  ${}_{hh}\mathbf{B}_y$  and  ${}_{hv}\mathbf{B}_y$  were analysed. The results indicate that neither receiver orientation nor polarisation affect the phase distribution of received signal. The Figure 5-14 shows the boxplot of the phase distribution for all 4 polarisation settings across 16 receiver orientations. It is clear to see that the 64 sample phase distributions are almost all identical and follows the uniform distribution  $U(-\pi, \pi)$ .

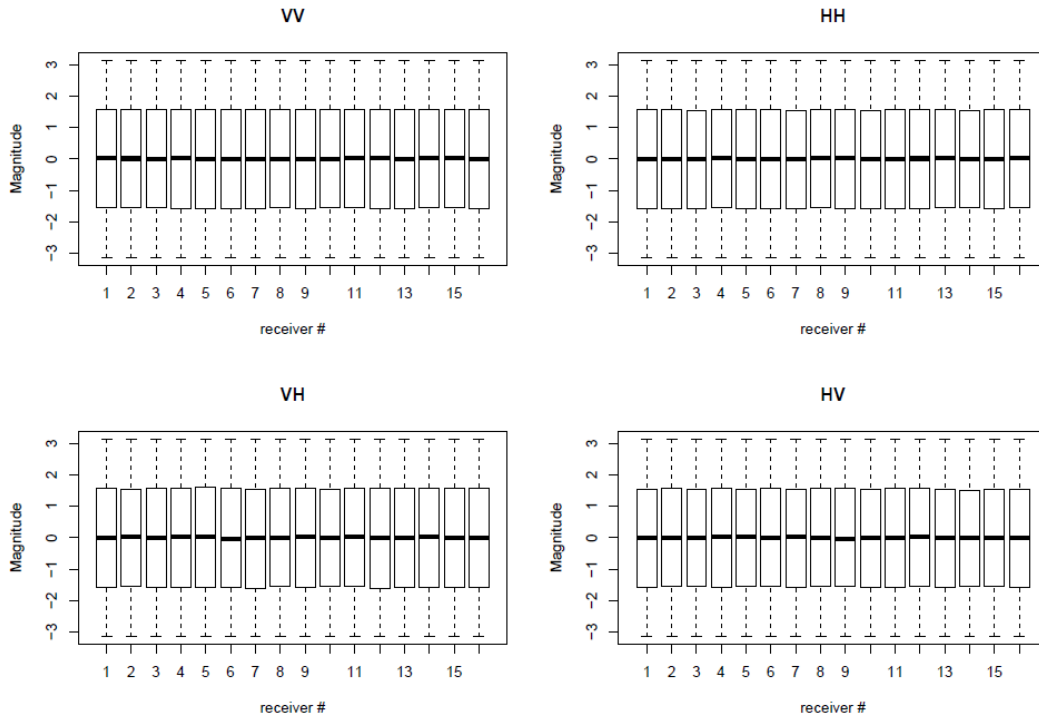
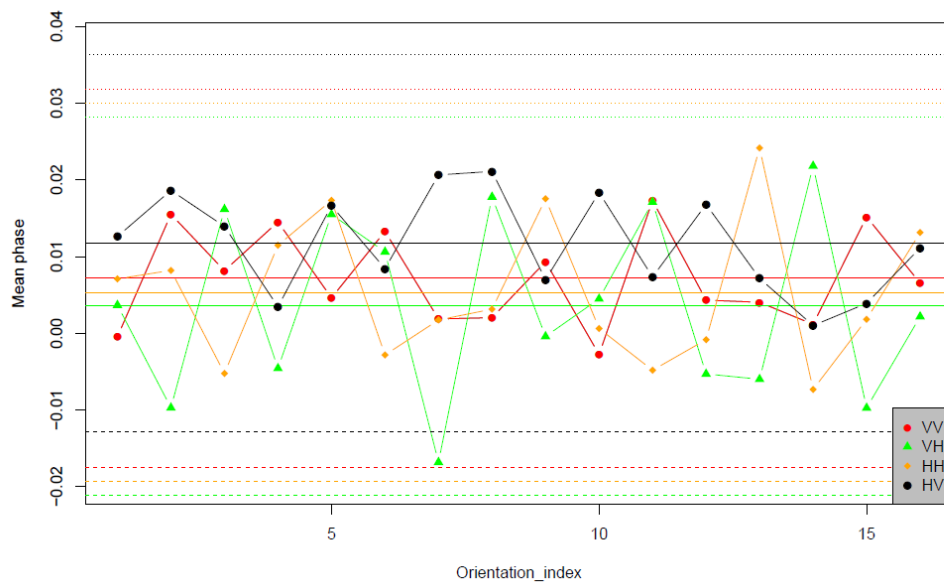


Figure 5-14: Phase distribution of the 4 polarisation settings across 16 Rx orientations

Furthermore, the control chart Figure 5-15 shows that all data points lie within the control zone, which confirms that no significant difference can be observed between the signal phase distributions with respect to different polarisation and receiver orientation settings.



**Figure 5-15: Variation of phase mean across the 16 receiver orientations.**

## 5.4 Polarisation Effects on Signal Correlation

In the previous section, the findings of the distribution analysis were presented. This section explores the effects of polarisation on signal correlation, focusing on the correlation between signals of different frequencies and the correlation between signals of different receiver orientations. As with the previous section, the amplitude matrices  $\mathbf{v_vA_x}$ ,  $\mathbf{v_hA_x}$ ,  $\mathbf{h_hA_x}$ ,  $\mathbf{h_vA_x}$  and phase matrices  $\mathbf{v_vB_x}$ ,  $\mathbf{v_hB_x}$ ,  $\mathbf{h_hB_x}$ ,  $\mathbf{h_vB_x}$ , will be looked at separately, in addition, the signal matrices  $\mathbf{v_vX}$ ,  $\mathbf{v_hX}$ ,  $\mathbf{h_hX}$  and  $\mathbf{h_vX}$  will also be investigated. The effects of polarisation relative to both frequency and receiver orientation will be studied. Each study begins with 4 data matrices of different polarisation settings, which can be grouped into 10 distinct pairs, i.e.

(VV, VV), (VV, VH), (VV, HV), (VV, HH),

(VH, VH), (VH, HV), (VH, HH),

(HV, HV), (HV, HH),

(HH, HH)

A correlation matrix can be constructed for each pairing, assuming the data matrices are of dimension  $m \times n$ , the process is as follows:

1. Choose a column from each matrix, resulting in 2 column vectors of length  $m$ .
2. Compute the correlation coefficient between the  $1 \times m$  vectors.
3. Repeat steps 1 and 2 for all possible pairings of columns, including duplicate pairings;
4. Arrange the correlation coefficients into a  $n \times n$  matrix

The resulting matrix in step 4 is the correlation matrix. More explicitly,

**Let**

$A, B$  denote the 2 matrices in the pairing, both of dimension  $m \times n$

$A(k)$  denote the  $k^{\text{th}}$  column of  $A$ , of dimension  $m \times 1$

$\text{Cor}[u, v]$  denote the correlation coefficient between vectors  $u$  and  $v$ , see [5.2]

$C$  denote the correlation matrix

$C(x, y)$  denote the element corresponding to row  $x$ , column  $y$  of  $C$

The correlation matrix  $C$  can be constructed with the following loop:

**For**  $i = 1$  to  $n$

**For**  $j = 1$  to  $n$

$$C(i, j) = \text{cor}[A(i), B(j)]$$

**End**

**End**

The correlation coefficient between 2 vectors gives an indication of the degree to which they are correlated, that is the extent to which variations in one vector indicates similar variations in the other. In this study, the vectors correspond to data samples of different polarisation, frequency, or Rx orientation; thus comparing the patterns formed by the 10 distinct correlation matrices provides the means to identify the effects of polarisation in relation to receiver orientation or frequency.

The following subsections presented the findings of the investigations. The correlation heatmaps shown in these subsections provide a visual representation of the correlation matrices, whose entries are real numbers between 0 and 1. Values close to 0 corresponding to low levels of correlation are shown in dark blue; conversely, values close to 1 indicating high levels of correlation are shown in dark red. Note that the correlation coefficient between a vector and a copy of itself is always 1, and the operation that computes the correlation coefficient between two vectors is commutative. The consequence of this is that the correlation matrix computed from a matrix and its copy will be symmetrical. This can be seen in 4 of the 10 correlation matrices, specifically those computed from the polarisation pairings (VV, VV), (VH, VH), (HV, HV), and (HH, HH).

#### **5.4.1 Polarisation effects on amplitude correlation in relation to frequency**

In this subsection, the heatmaps are generated from the amplitude matrices  $\mathbf{v}\mathbf{v}\mathbf{A}_x$ ,  $\mathbf{v}\mathbf{h}\mathbf{A}_x$ ,  $\mathbf{h}\mathbf{h}\mathbf{A}_x$  and  $\mathbf{h}\mathbf{v}\mathbf{A}_x$ . Figure 5-16 shows the 4 heatmaps generated from the pairings containing the same amplitude data matrix; the observed patterns are symmetrical as expected. There is a stark contrast between the patterns of co-polarised (VV, VV), (HH, HH) and cross-polarised (VH, VH), (HV, HV) settings, with several points of interest:

For co-polarised settings:

- The strength of the correlation is relative to the perpendicular distance from the diagonal.
- Stripes parallel to the diagonal are of uniform 'potential' i.e. they contain correlation coefficients with very similar values. The value gradually decreases as the focus of observation moves away from the diagonal.
- While both are co-polarised, the VV setting shows significantly stronger correlation than HH in the regions near the diagonal. This implies that VV polarisation setting would have wider coherence bandwidth.

For cross-polarised settings:

- The correlation heatmaps show a chequered pattern. This is due to frequency selective polarisation fading of cross polarised waves.
- There are elements right next to the diagonal which are calculated from samples with only a 0.625 MHz frequency offset but the correlation coefficient is close to 0. This is due to the particular nature of the polarisation fading in this scenario.
- The correlation pattern for VH appears to match those of HV after a diagonal shift of roughly 20 frequency offsets and vice versa, which equates to 12.5 MHz. This results from the periodic fading pattern of cross polarised waves seen earlier in the chapter.

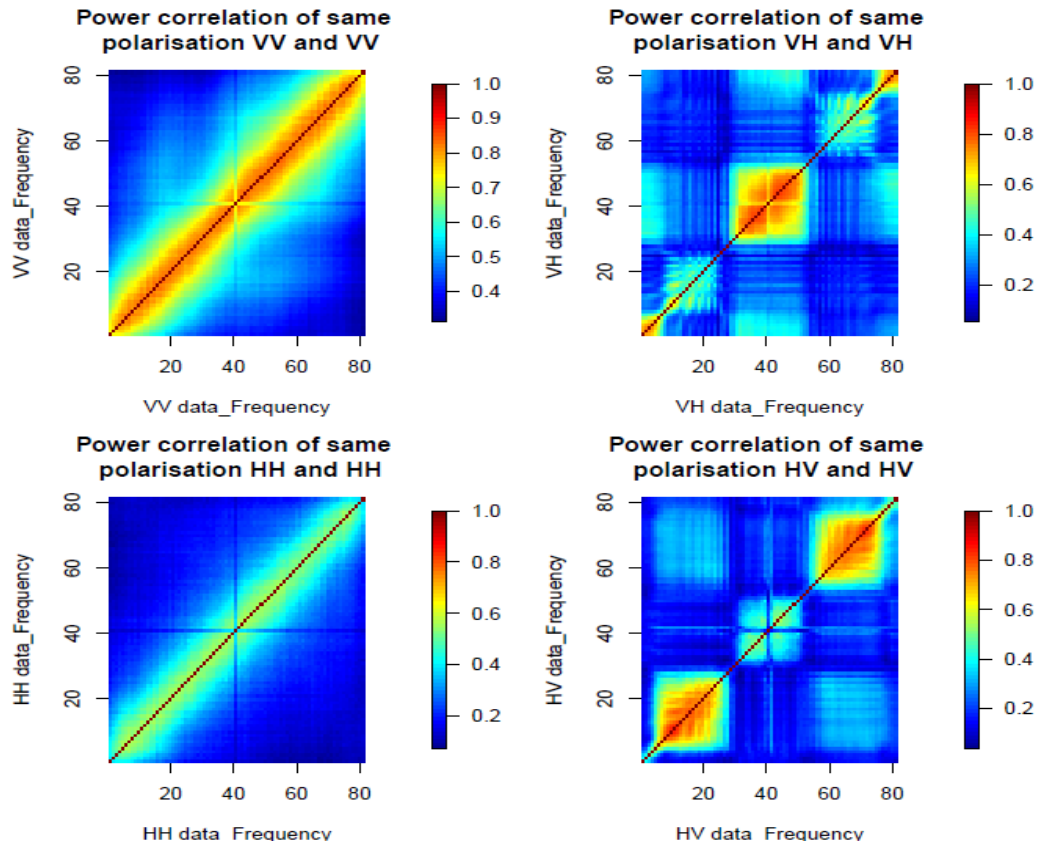
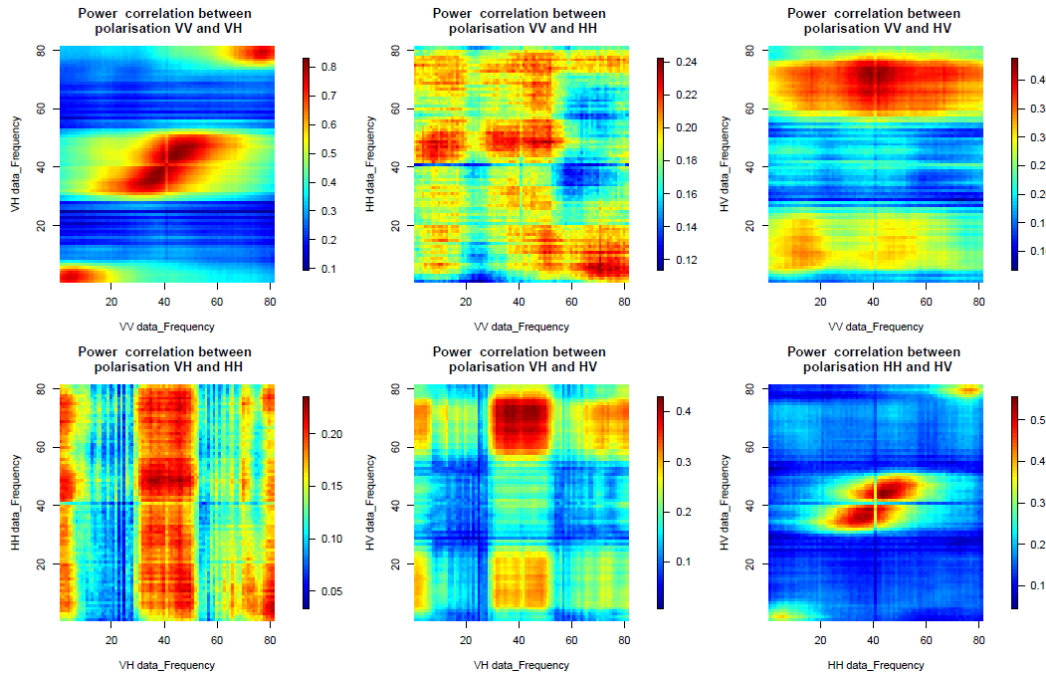


Figure 5-16: Heatmap of amplitude correlation between same polarisation settings

The patterns for co-polarised settings is as expected, where the correlation is strong near the diagonal when the frequency offset is small, and gradually gets weaker as the frequency offset increases. The chequered correlation pattern for cross-polarised settings is of great interest as it appears to be a regular, periodic and predictable pattern. The fact that data from frequency samples so close to each other can have correlation close to 0 is also surprising. This discreet pattern of correlation is readily exploitable as signals from certain far apart frequency bands are highly correlated, thus reducing the requirement on the SINR threshold to maintain a wide channel; whilst in other more closely packed bands the signals do not correlated at all, which naturally helps with interference. Knowing these patterns will greatly help improving the channel efficiency.



**Figure 5-17: Heatmap of amplitude correlation between different polarisation settings**

Figure 5-17 shows the amplitude correlation heatmap for the six remaining polarisation pairings. These can be split into 3 groups:

1. Those with the same Tx setting but different Rx setting:  
(VV, HV) and (VH, HH)
2. Those with the same Rx setting but different Tx setting:  
(VV, VH) and (HV, HH)
3. Those where both Tx and Rx settings are different:  
(VV, HH) and (VH, HV)

The 2 correlation patterns within group 1 are very similar, and provide a validation to each other. In contrast, the correlations within group 2 are nearly complementary to each other, that is to say their sum would be a matrix with all values close to 1. This has the consequence of making the 2 patterns look like “photo negatives” of each other, i.e. reversing the colour scale will transform one into the other. This phenomenon is closely related to the identity  $\sin^2 x +$



$\cos^2 x = 1$ , which also relates to the patterns' periodic nature with respect to the cross-polarised axis. In fact, shifting one pattern 20 frequency offsets along the co-polarised axis will make it overlap with the other, the frequency offset coincides with the width of the chequered box shown in Figure 5-16, which maybe of significance. It would be an interesting topic to have an in-depth discussion on the interpretation of this phenomenon.

### 5.4.2 Polarisation effects on phase correlation in relation to frequency

This subsection shows the heatmaps generated from the phase matrices  $_{vv}\mathbf{B}_x$ ,  $_{vh}\mathbf{B}_x$ ,  $_{hh}\mathbf{B}_x$  and  $_{hv}\mathbf{B}_x$ . The phase correlation patterns for the four identically polarised pairs are illustrated in Figure 5-18.

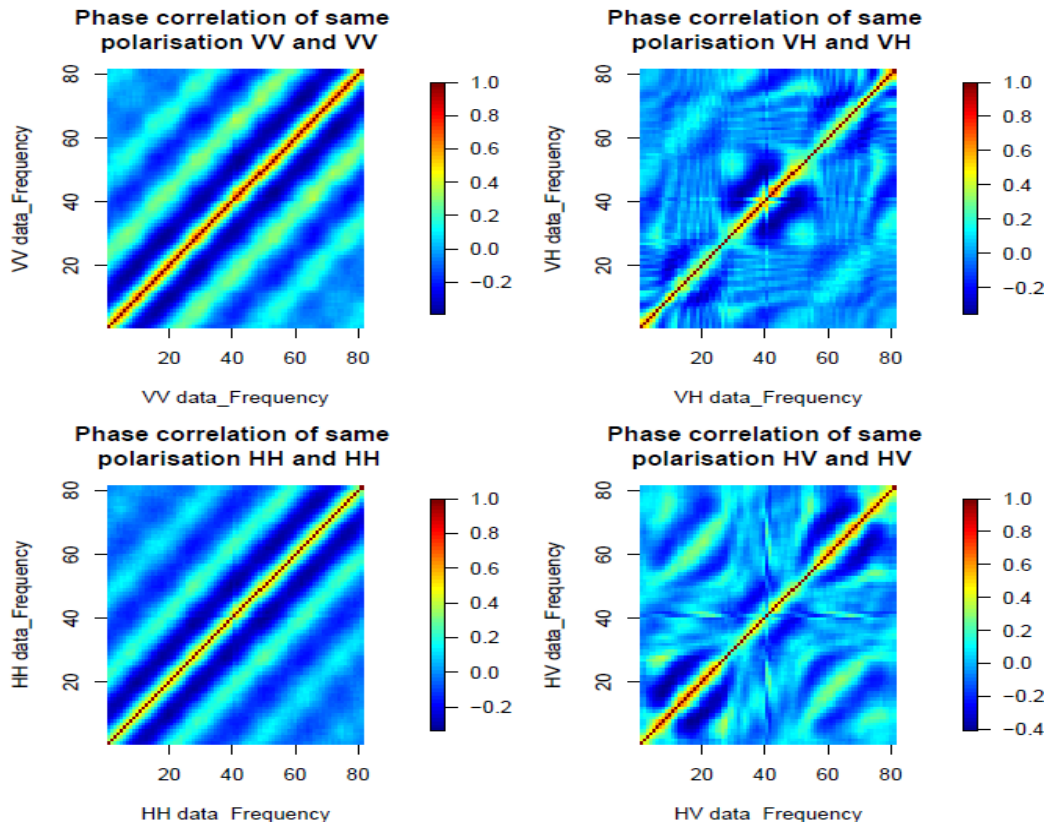
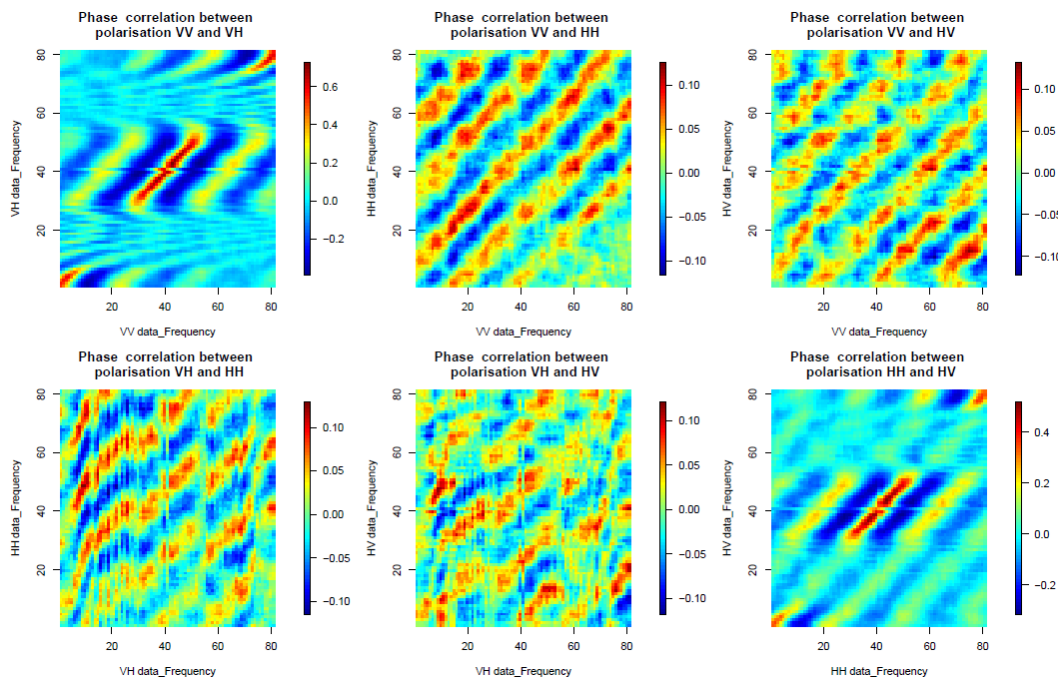


Figure 5-18: Heatmap of phase correlation between same polarisation settings

In Figure 5-18, the co-polarised panels exhibit patterns that share a number of characteristics with the corresponding amplitude correlation patterns, namely the data is most strongly correlated near the diagonal and lines equal distant from it having similar correlation values. The difference is as we move further away from the diagonal; the correlation does not monotonically decrease but fluctuates periodically. This is not so surprising since the phase is closely related to the trigonometric functions. A more significant observation is that distance between adjacent peaks is again 20 frequency offsets. For cross-polarised settings, the correlation again forms a chequered pattern, although not as clear as the corresponding amplitude patterns. As with the amplitude patterns, a shift of 20 frequency offsets along the diagonal will superimpose one pattern onto the other.



**Figure 5-19: Heatmap of phase correlation between different polarisation settings.**

The correlation heatmaps of signal phase for the remaining 6 polarisation pairings are shown in Figure 5-19: Heatmap of phase correlation between different

polarisation settings.. The patterns for (VV, VH) and (HV, HH) are again distinct from the others but very similar to each other. All panels display a wavy striped pattern, this confirms that the impact of phase is periodical.

### 5.4.3 Polarisation effects on signal correlation in relation to frequency

Final part of the frequency related study presents the polarisation effects on the received signal. The correlation heatmaps generated from the signal matrices  $w\mathbf{X}$ ,  $vh\mathbf{X}$ ,  $hh\mathbf{X}$  and  $hv\mathbf{X}$  are in Figure 5-20.

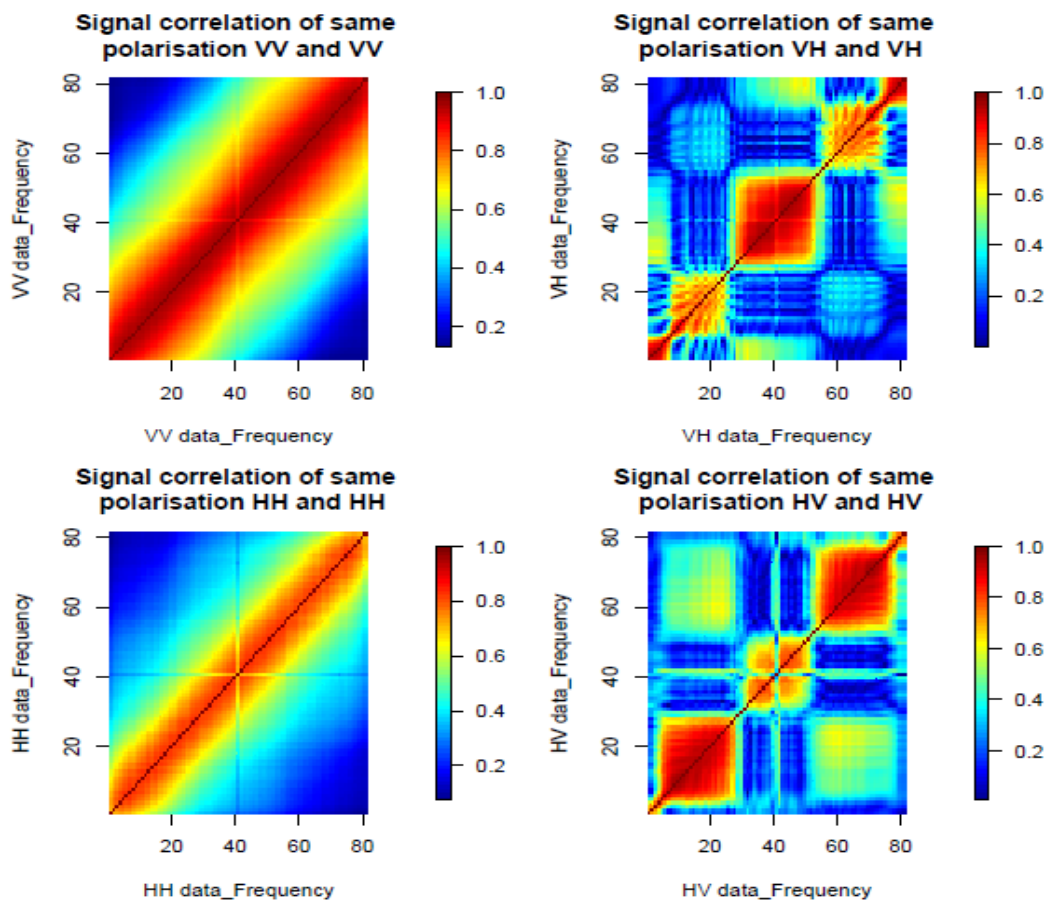
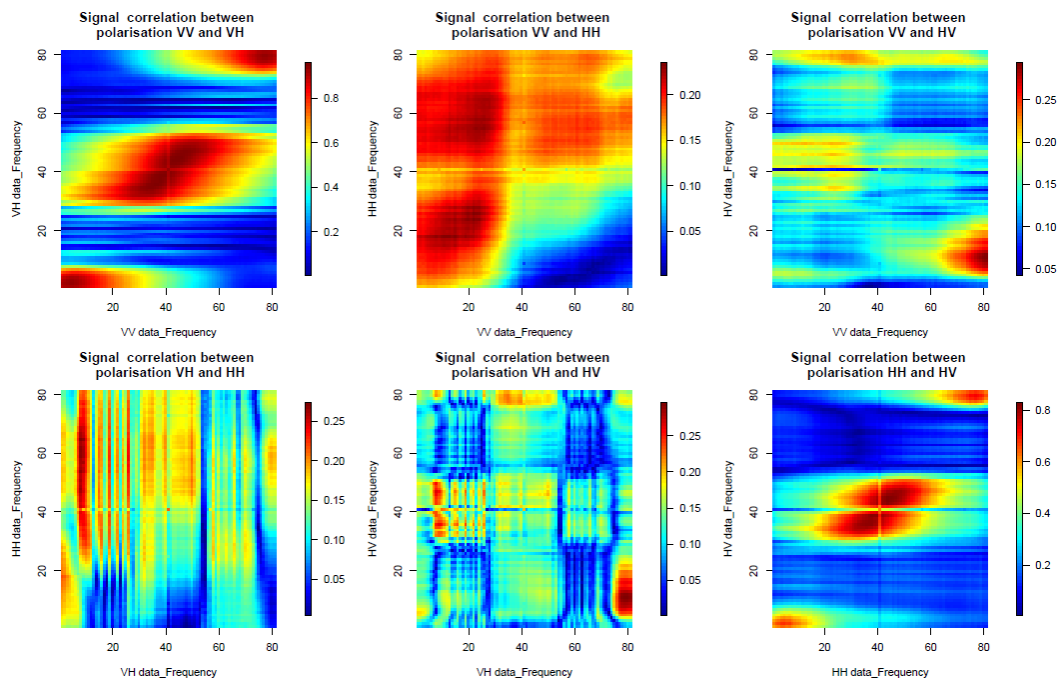


Figure 5-20: Heatmap of signal correlation between same polarisation settings

The patterns are almost identical in shape to the corresponding patterns for amplitude. The difference is that here the contrast is much stronger. The influence of phase is harder to see, although looking at the co-polarised panels closely reveals that the signal correlation shows the superimposed pattern of the corresponding amplitude and phase patterns, with greater intensity in regions of high correlation. This indicates that the correlation signal is greatly enhanced with the addition of phase information.



**Figure 5-21: Heatmap of signal correlation between different polarisation settings**

Figure 5-21 shows signal correlation between different polarisation settings. Again, both the shape and grouping of the patterns are similar to those of amplitude correlation, while the intensity is higher. The (VH, HV) pattern exhibits symmetry with respect to both axis indicating the similarities between the VH and HV channels.

So far in this section, the effects of polarisation on the signal in relation to frequency has been explored, the main findings were:

- Polarisation has a systematic effect on signal correlation in relation to frequency; instead of being a collection of random values, the correlation coefficients fall into well manner patterns.
- Polarisation has significant effects on the amplitude correlation; co-polarised settings exhibit vastly different patterns to cross-polarised settings.
- It also affects the phase correlation strongly, unlike the phase distribution which isn't affected.
- The signal correlation reveals a similar pattern to that of amplitude, except that regions of high correlation are even more pronounced.
- Cross-polarised channels exhibit an interesting chequered pattern which can be utilised for increased channel efficiency.
- Many correlation patterns are periodic in nature, in relation to the period, the figure 20 frequency offsets comes up time and again.

This concludes the correlation analysis in relation to frequency. The next subsection will explore the effects of polarisation on signal correlation with respect to receiver orientation.

#### **5.4.4 Polarisation effects on signal correlation across receiver orientation**

This subsection looks at the effect of polarisation in relation to 16 receiver orientation of antenna element due to the circular Rx array. The correlation coefficients were computed between samples corresponding to different Rx orientations. Overall, the correlation between receiver orientations is weaker and

more random in nature. The results are evident that the notable correlations are only presented polarisation settings are the same. Otherwise, the correlation matrices more or less revert to a collection of random values close to 0, even if the samples in comparison come from adjacent orientations. Therefore, this section only presents the correlation heatmap of the 4 scenarios where the polarisation settings are the same.

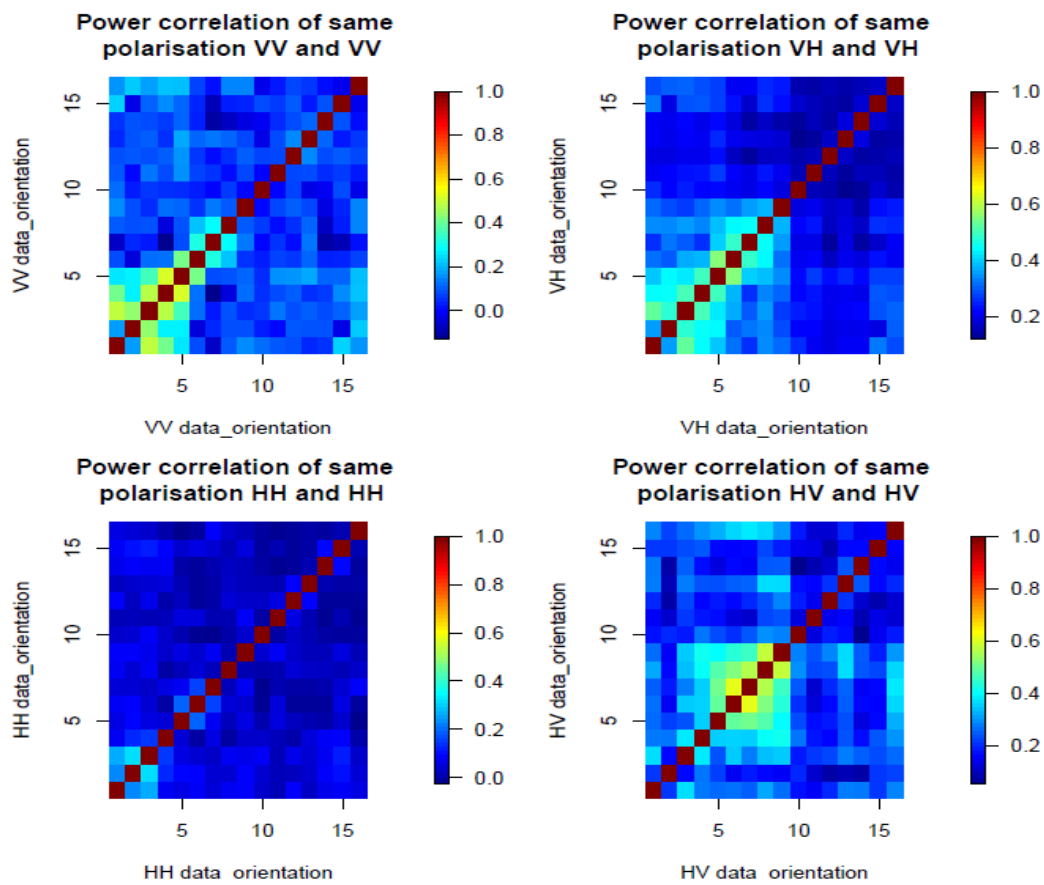


Figure 5-22: Heatmap of amplitude correlation in relation to Rx orientation

Figure 5-22 shows the correlation pattern for amplitude, the 4 panels corresponds to the 4 polarisation settings. It shows that the correlation of amplitude between receiver orientations is at best moderate, although regions showing the highest levels of correlation are near the diagonal indicating that received signal amplitudes from neighbouring orientations do have a degree of similarity. In this

turn suggest that spatial factors such as the distance and the angle between elements of different orientations do have relevance.

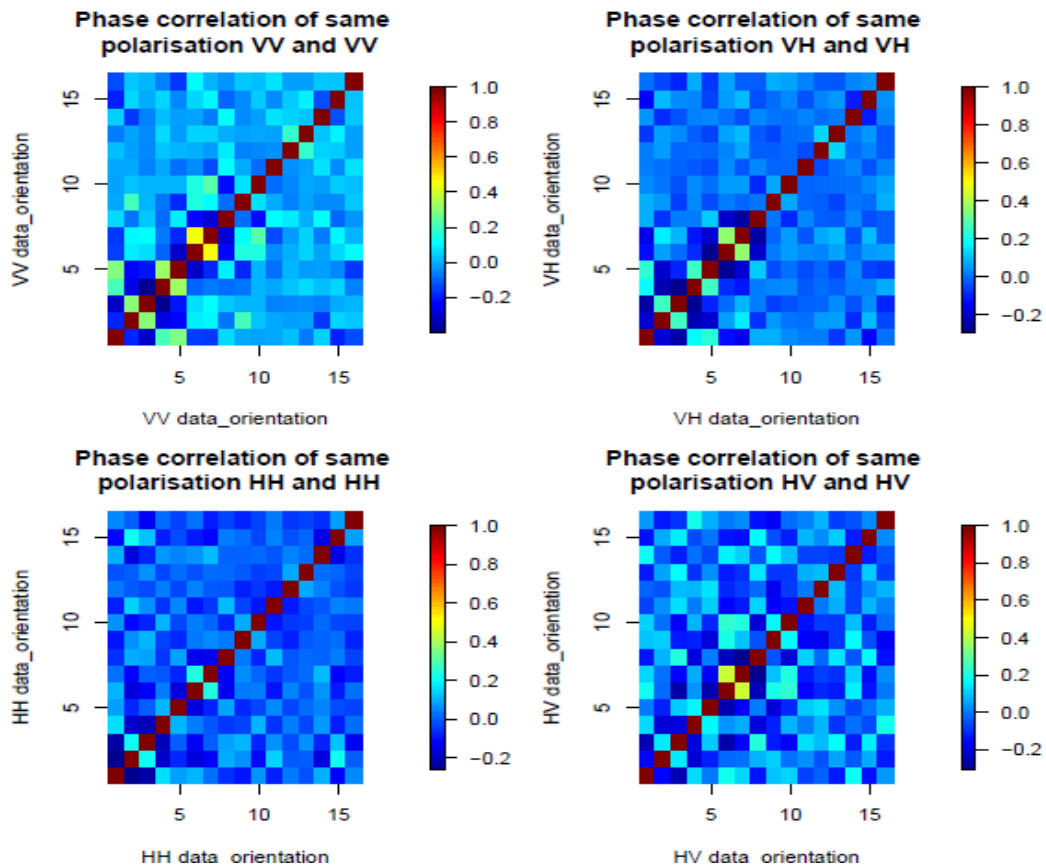


Figure 5-23: Heatmap of phase correlation in relation to Rx orientation

Figure 5-23 shows correlation heatmap for phase in relation to receiver orientation. The patterns appear relatively noisy and random. However, unlike completely uncorrelated items, most of the individual elements show levels of correlation significantly greater than zero. A comparison to Figure 5-11 reveals a correspondence, though it's not immediately obvious to see. The receiver orientations corresponding to the region displaying the highest correlations (the same few yellow pixels in each panel) are the same orientations that received the strongest levels of signal in Figure 5-11.

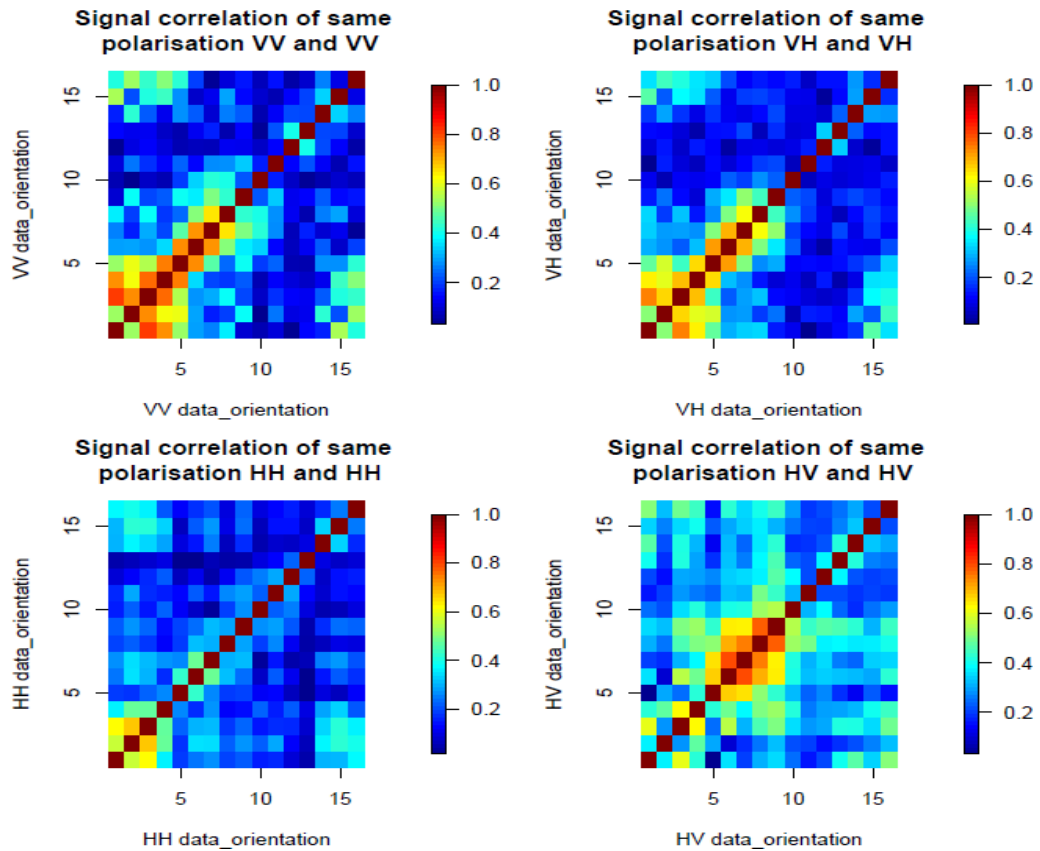


Figure 5-24: Heatmap of signal correlation in association with Rx orientation

Figure 5-23 shows correlation heatmap for signal in relation to receiver orientation. The correlation patterns for the combined signal displays much stronger levels of correlation compared to the pattern for individual amplitude and phase components, both of which displayed weak levels of correlation. Take the panel HH for example, the heatmaps for both the amplitude and phase components are blue throughout indicating correlation no greater than 0.3, yet the corresponding heatmaps for signal contains regions where the correlation approaches 0.7 represented by orange. This shows that the individual amplitude and phase components do not necessarily have to correlate in order for the combined signal to do so, suggesting that in this case the complete product is greater than the sum of its parts.



The receiver orientations do not show uniform levels of correlation, despite being symmetrical relative to the circle. The orientations displaying the highest levels of signal correlation matches with those in corresponding amplitude and phase patterns, as well as those that received the strongest signals in Figure 5-11. This indicates a relationship between signal strength and correlation from which it could be suggested that the reason some neighbouring orientations that do not show higher levels of correlation is because the average received signal strength at those orientations are relatively, such that the influence of noise becomes more significant. The randomising effect of noise reduces signal correlation resulting in uneven levels of correlation across the receiver orientations.

#### **5.4.5 Polarisation effects on coherence bandwidth**

Coherence bandwidth, estimated from the measured data, has been defined and discussed in section 4.2.2. This section presents more specific results: coherence bandwidth under individual polarisation settings. These results are computed based on the correlation coefficients between signals across the frequency domain seen in subsection 5.4.1.

For every measurement position, 4 coherence profiles can be generated in correspondence with the 4 polarisation settings. The coherence bandwidth values obtained from the profiles of the same polarisation can be collected and statistically compared against those collected from other polarisation settings. This way the influence of individual measure positions is eliminated, so that some light can be shed on the effects of polarisation on the coherence bandwidth in a general sense, rather than restricted specific measurement positions.

The results of the study indicate that statistically speaking, polarisation settings can have an effect on the coherence bandwidth of the channel. Generally, co-polarised settings have greater coherence bandwidth than cross-polarised

settings. Figure 5-25 show a comparison of the correlation heatmap between the 4 polarisation settings

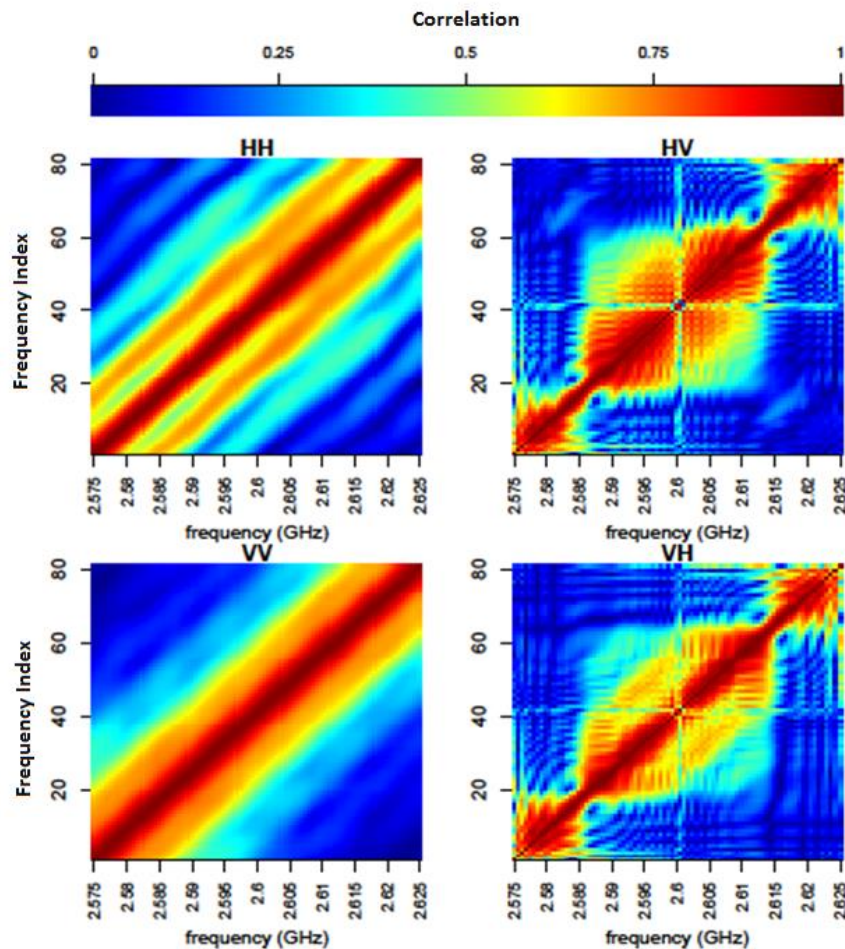


Figure 5-25: Heatmap of signal correlation across the frequency domain

As can be seen, the coherence correlation patterns are quite different between co-polarised and cross-polarised settings. Due to the clearly distinguished equal potential diagonal stripes, the coherence bandwidth for co-polarised settings can be readily read of the heatmap without the coherence profile. However, for cross-polarised settings, it would be very difficult to do the same and the coherence profile would be required, See Figure 5-26

The x-axis shows the frequency difference between two signals, the y-axis is the average correlation between signals given frequency difference. To obtain the coherence bandwidth, choose a threshold correlation value from the y-axis and read off the corresponding frequency difference on the x-axis, that value would be the coherence bandwidth for the chosen correlation threshold. For example, the interception between the curve and the top line is the coherence bandwidth for the 0.9 threshold, which ensures a signal correlation of 0.9 or above. Similarly, the crossing point between the curve and the bottom line gives the value of the coherence bandwidth for signal correlation greater than 0.5.

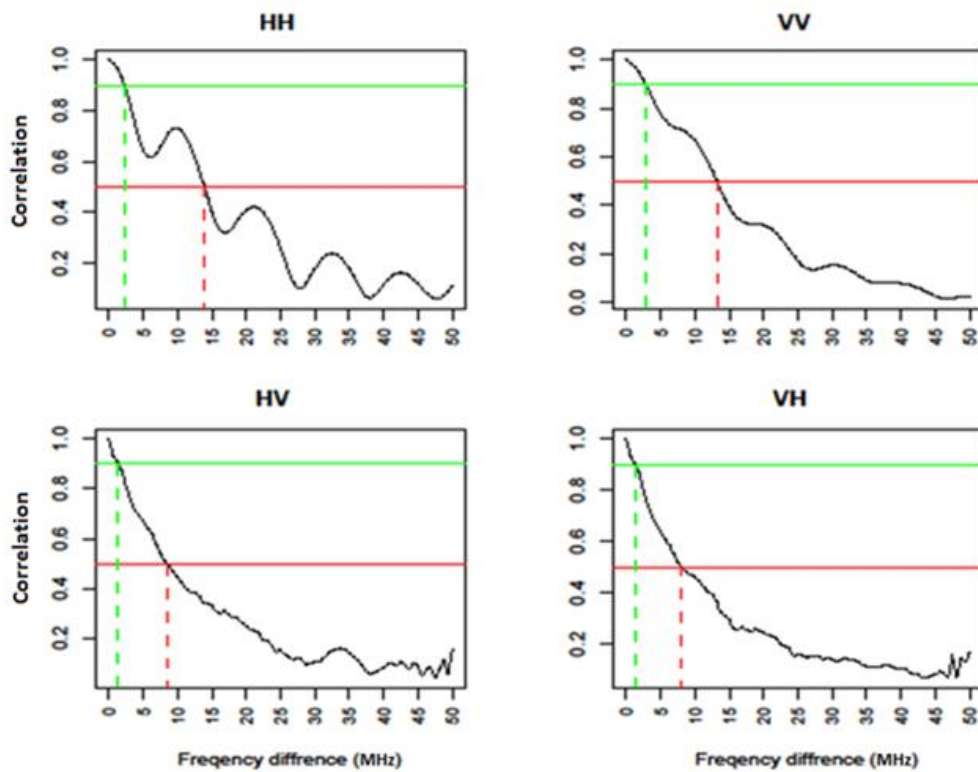


Figure 5-26: Coherence profile generated from correlation matrix

It is clear to see that the coherence bandwidth for co-polarised settings is wider than cross-polarised settings for both threshold values, which confirms the effect of antenna polarisation on the coherence bandwidth of the channel.

#### **5.4.6 Correlation of previous findings observed from different positions**

Some of the correlations matrices presented in the previous subsections show strong patterns, but they were generated from individual measuring positions and selected as a typical representation of the correlation matrices from all the measuring sites, in order to illustrate what the typical pattern look like. However, even though they were the typical representations, there are of course variations from site to site, and it's not a very scientific approach to draw any conclusions based on their 'typicality'. It is necessary to statistically correlate the correlation patterns themselves before drawing firm conclusions. Therefore the presentations to be made this subsection are crucial to the whole of section 5.4, as it validates the findings of the previous sections.

In order to assess the commonality of the correlation patterns presented in earlier subsections and to tell whether were site specific or not, the same statistical correlation method is employed, but this time to correlate the correlation patterns. This is possible because the information contained in the correlation matrices are arranged in fixed order, and forms 1 to 1 correspondences with correlation matrices from other measuring positions. For example, column 5 row 16 of a frequency related amplitude correlation matrix from any measuring position would always contain the correlation coefficient between samples corresponding to the 5<sup>th</sup> and the 16<sup>th</sup> frequency offsets measured at that position. With this fixed order, the correlation coefficients between the matrices from 2 different positions can be simply computed by rearranging both correlation matrices into vectors, i.e. concatenate the columns together, and compute the correlation coefficient between the 2 vectors with the previously stated method in the usual way.

### ***Confirmation of phase correlation across different locations***

Figure 5-27 shows the correlation of phase correlation matrices across 60 measuring positions. The correlation patterns for cross-polarised settings are almost entirely red (correlation coefficient  $> 0.8$ ), indicating high levels of correlation between all 60 measuring positions. The patterns for co-polarised settings show a greater variation in the correlation value, but on the whole the patterns are still dominated by orange and red regions representing coefficient values over 0.7. This confirms that the individual site specific phase correlation patterns are highly correlated across the different measuring positions, validating the conclusions drawn about the effect of polarisation on phase correlation in subsection 5.4.2.

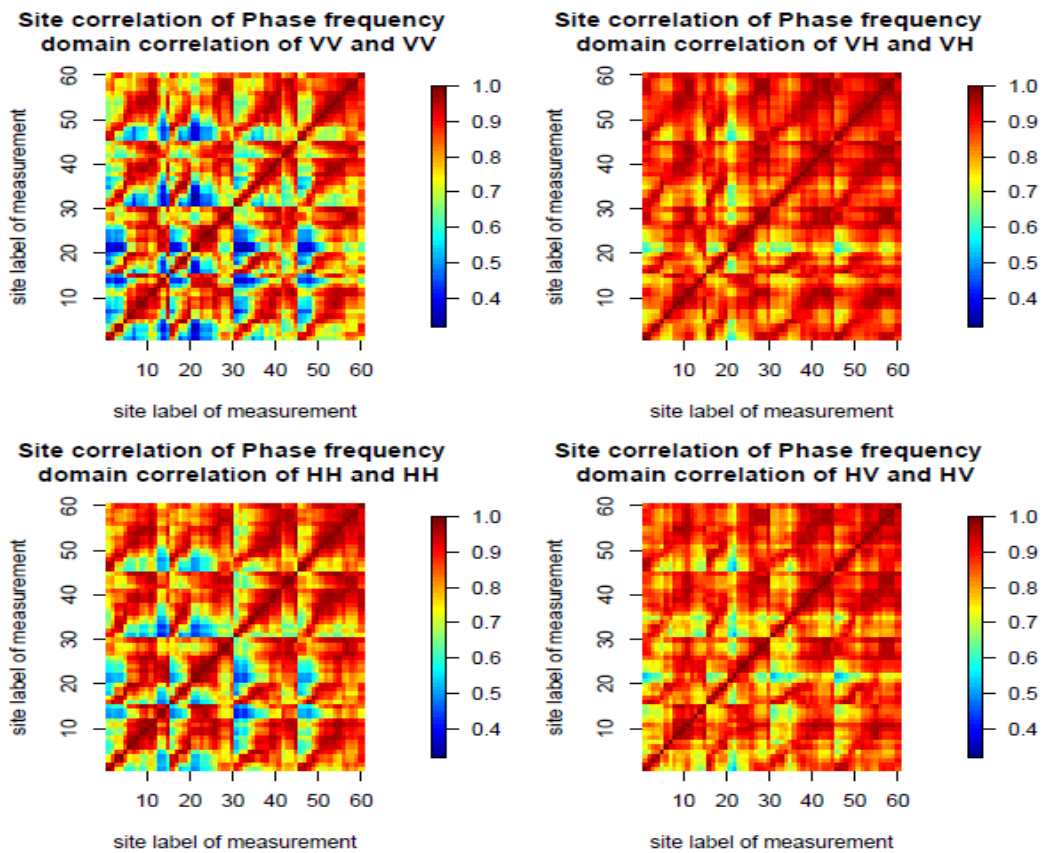


Figure 5-27: Correlation of phase correlation across measuring sites.

### ***Confirmation of amplitude correlation across different locations***

Similarly, Figure 5-28 shows the correlation of amplitude correlation across the different sites. This time, the correlations for all 4 polarisation settings are virtually entirely over 0.8. This give a firm base to draw the conclusion that the findings presented in subsection 5.4.1 is valid for all measuring positions, irrespective of where the data was collect from.

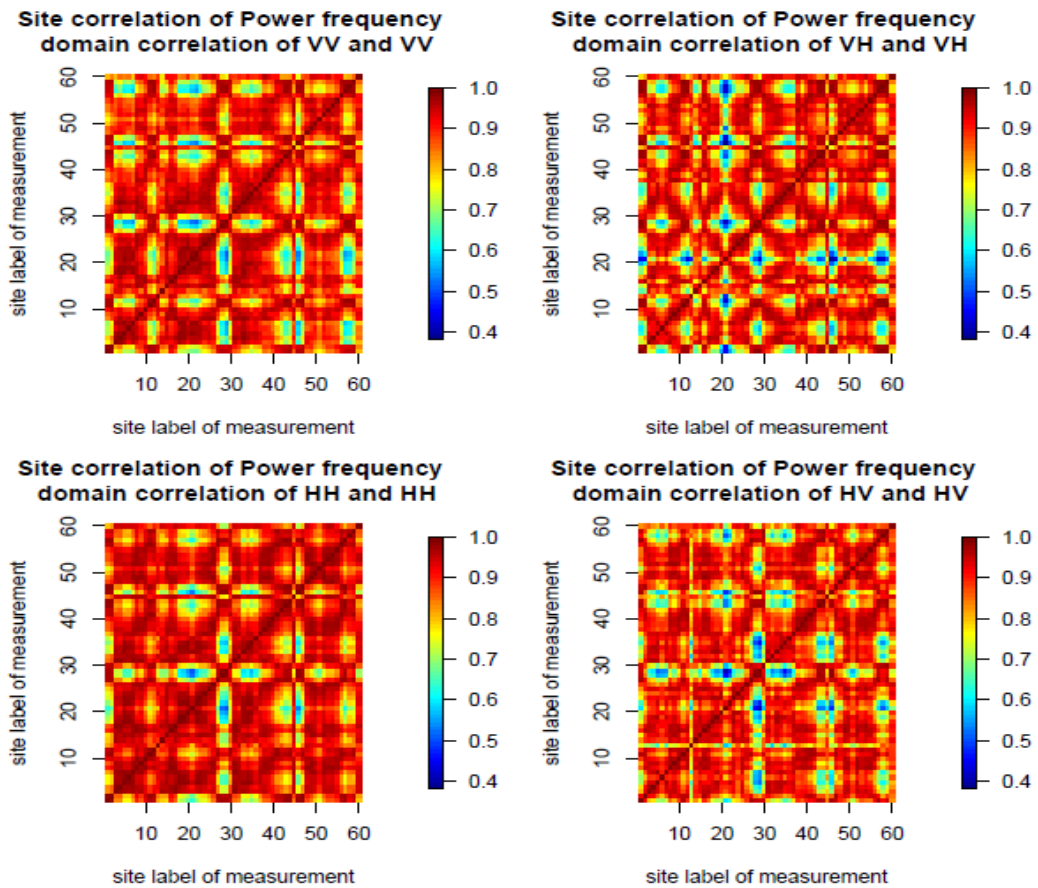
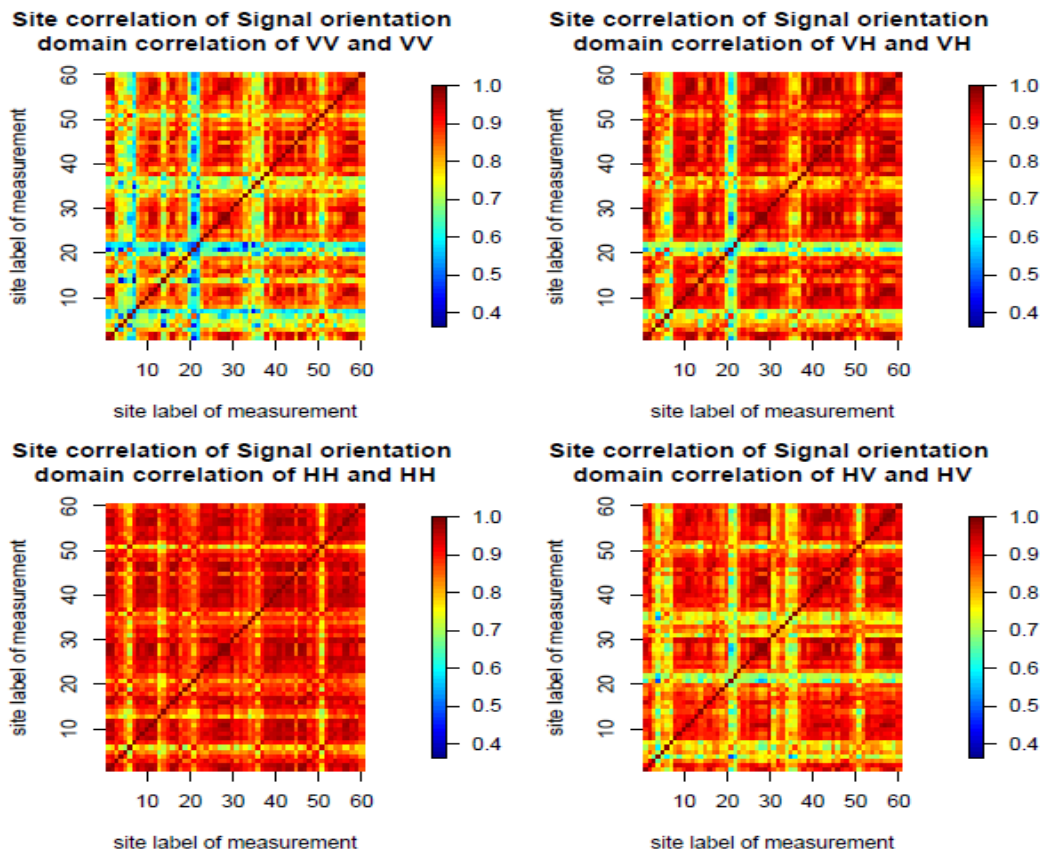


Figure 5-28: Correlation of amplitude correlation across measuring sites.

### ***Confirmation of signal correlation across the different locations***

Finally, the correlation of signal correlation is shown in Figure 5-29. Again the figure is very similar to the previous ones, high correlation values greater than 0.8 dominates the landscape. This validates the conclusions of subsection 5.4.3.



**Figure 5-29: Correlation of signal correlation across measuring sites.**

In summary, the results presented in this section confirms the consistency of the correlation patterns presented in previous sections across all of the measuring sites, and in doing so validates the findings of previous sections.

## 5.5 Data based analysis of polarisation diversity gain

The previous sections of this chapter described the effects of polarisation on signal distribution and signal correlation. This section will tie the results from these different perspectives together, drawing logical links between them to sketch an overall prospectus for improving system performance through a novel polarisation diversity combining scheme.

Polarisation diversity is the concept of using multiple signals of different polarisations to improve system performance. The signals are combined at the receiver via a diversity combining scheme such as *selection combining* (SC), *equal-gain combining* (EGC) and *maximal-ratio combining* (MRC). Unlike space diversity, polarisation diversity do not require large inter element spacing which often becomes impractical in compact devices.

The previous two sections explored the strength and correlation of signals in differently polarised sub-channels. As it happens, sub-channel signal strength and sub-channel correlation are two of the main factors that determines the diversity gain. [102]. Sub-channel signal strength determines the *cross-polar discrimination* (XPD) of the channel which influences SC techniques whilst sub-channel correlation affects the channel capacity. In general, higher correlation between sub-channels results in lower system capacity and less diversity gain [103].

Figure 5-30 Depicts a  $2 \times 2$  dual-polarized MIMO system, the channel matrix  $\mathbf{H}$  is comprised of 4 sub-channels  $h_{VV}$ ,  $h_{VH}$ ,  $h_{HV}$ ,  $h_{HH}$ , and be written as:

$$\mathbf{H} = \begin{bmatrix} h_{VV} & h_{VH} \\ h_{HV} & h_{HH} \end{bmatrix} \quad (5.1)$$



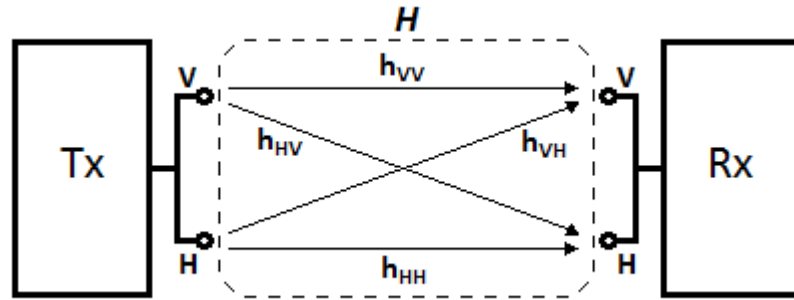


Figure 5-30:  $2 \times 2$  MIMO system with dual-polarised antennas

Here  $h_{VV}$  and  $h_{HH}$ , represents the co-polar sub-channels of  $\mathbf{H}$  whilst  $h_{VH}$  and  $h_{HV}$  represents the cross-polar sub-channels.

The channel transfer matrix  $\mathbf{H}$  of a MIMO system having dual-polarised antennas on both ends of the transmission link is significantly different to that of a mono-polarised, spatial MIMO system. In the spatial case, all of the sub-channels are *independent and identically distributed* (i.i.d.) with equal average received power. However, this is not the case for dual-polarised MIMO channels [104], where sub-channels differ in terms of average received signal strength, Ricean K-factor, and correlation and XPD. This was shown in section 5.3, where differently polarised sub-channels exhibited different properties. The difference in received power between sub-channels of different polarisations characterises the XPD of the channel, which is a useful indicator of potential for polarisation diversity gains.

### 5.5.1 Effect of cross-polar discrimination on selection gain

Cross-polar discrimination is the difference, in dB, of the mean signal strength between co-polar sub-channels and cross-polar sub-channels, it can be written as a vector with two components [105]:

$$\begin{aligned} X_V &= \frac{E(|h_{VV}|^2)}{E(|h_{VH}|^2)} \\ X_H &= \frac{E(|h_{HH}|^2)}{E(|h_{HV}|^2)} \end{aligned} \quad (5.2)$$

$X_V$  is the ratio of the mean signal power received, by  $R_{X_V}$ , from  $T_{X_V}$  and  $T_{X_H}$ , whilst  $X_H$  is the ratio of the mean signal power received, by  $R_{X_H}$ , from  $T_{X_H}$  and  $T_{X_V}$ .

XPd is a useful measure of the degree of cross-coupling, or depolarisation in a channel, which is the phenomenon of purely V polarised waves emerging with H polarised components and vice versa. Cross-coupling is mainly caused by oblique reflections and scattering from obstacles as the wave propagates through the environment. Consequently, this effect can be significant in small cell scenarios.

Previous results has shown that the propagation characteristics of H and V polarised waves are significantly different, which facilitates antenna selection techniques where the sub-channel with highest instantaneous received power is chosen. In general, due to low antenna heights in indoor environments and Brewster's angle phenomenon, the instantaneous received power expected for purely V polarised waves is greater than that of H polarised waves, i.e.  $E(|h_{VV}|^2) > E(|h_{HH}|^2)$  [97]. Let  $\beta$  be the ratio between  $E(|h_{HH}|^2)$  and  $E(|h_{VV}|^2)$  and normalising  $E(|h_{VV}|^2)$  to 1, we have:

$$\begin{aligned} E(|h_{VV}|^2) &= 1 \\ E(|h_{HH}|^2) &= \beta \leq 1 \end{aligned} \tag{5.3}$$

from (5.2) and (5.3) we can write:

$$\begin{aligned} E(|h_{VH}|^2) &= \frac{1}{X_V} \\ E(|h_{HV}|^2) &= \frac{\beta}{X_H} \end{aligned} \tag{5.4}$$

with these parameters in place, an upper bound on the MIMO channel capacity in the form of mean squared Frobenius norm can be expressed as:

$$\overline{W} = N_r^V N_t^V + \beta N_r^H N_t^H + \frac{1}{X_V} N_r^V N_t^H + \frac{\beta}{X_H} N_r^H N_t^V \tag{5.5}$$

where  $N_r^V, N_t^V, N_r^H, N_t^H$  are the number of V polarise Rx, V polarised Tx, H polarised Rx, and H polarised Tx antenna elements respectively. Notice that as the XPD ( $X_V$  and  $X_H$ ) increases,  $\overline{W}$  decreases. Thus greater XPD will result in less channel capacity and polarisation diversity gain. This is because polarisation diversity achieves gains mainly through cross-polarised sub-channels. When the XPD becomes too high, the cross-polarised waves becomes negligible and the system essentially reduces to a co-polar channel and hence the available degrees of diversity is lost [106].

As mentioned earlier, the optimal strategy is to select the sub-channels with the highest instantaneous received power. The probability that the strongest sub-channel to be selected is cross-polarised reduces as XPD increases. Figure 5-31 shows the average SNR gain achieved as a monotonic decreasing function of the

XPD. The gain has maximum value of 3dB at 0 XPD and decreases asymptotically to 1.56dB as XPD tends to infinity.

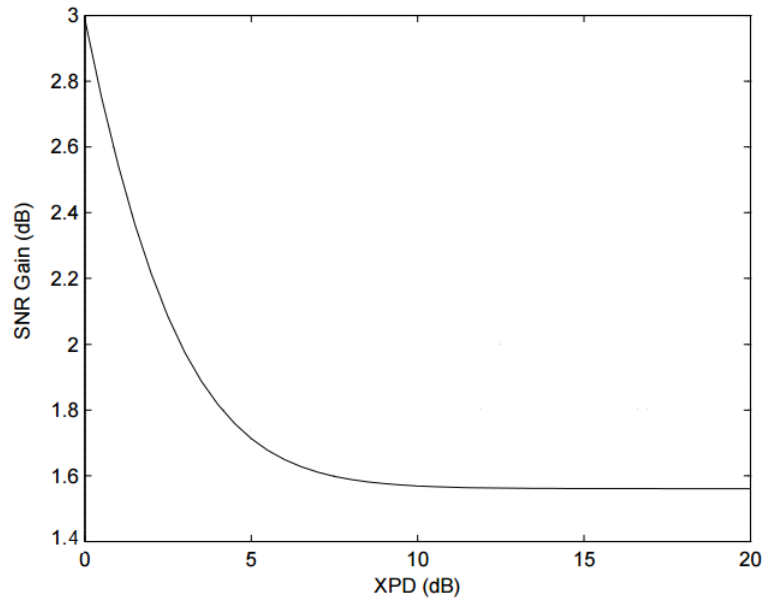


Figure 5-31: polarisation diversity gain as a result of XPD

The findings in section 5.3 has shown that the value of XPD for the measurement scenarios was around 3dBs, indicating substantial cross-coupling between the two polarisations, which in turn encourage polarisation diversity techniques [107].

### 5.5.2 Effect of sub-channel correlation on diversity gain

The second factor which determines diversity gain is the sub-channel correlation which was investigated in section 5.4. The maximum degrees of diversity,  $\eta$ , equals to the product  $\mathbf{N}_r \times \mathbf{N}_t$ , which are the number of Rx and Tx elements respectively. However, correlation between the sub-channels reduces the degrees of freedom and the number of independent channels. This reduces the diversity gain for selection combining performed on signals from multiple Rx antennas. On the other hand, for an individual Rx receiving multiple signals from different Tx's, where the

appropriate diversity combining technique is EGC or MRC, correlation between the signals will enhance the overall aggregate signal and improve diversity gain. Therefore stronger correlations between VV and VH sub-channels (and similarly HH and HV) will correspond to greater polarisation diversity gain.

### 5.5.3 Polarisation diversity combination scheme

The signal correlation heatmaps presented in Figure 5-16 –Figure 5-21 show that both polarisation and frequency affects the sub-channel signal strength, by choosing frequencies with strong correlations and combining with MRC at a single Rx, a significant polarisation matching gain can be achieved. Furthermore, the multiple signals at different Rx in the array can be combined using SC to also take advantage of the diversity gain, see Figure 5-32. The findings from sections 5.3 and 5.4 provides evidence that polarisation play a role to achieve uncorrelated sub-channels, which will help increase channel capacity.

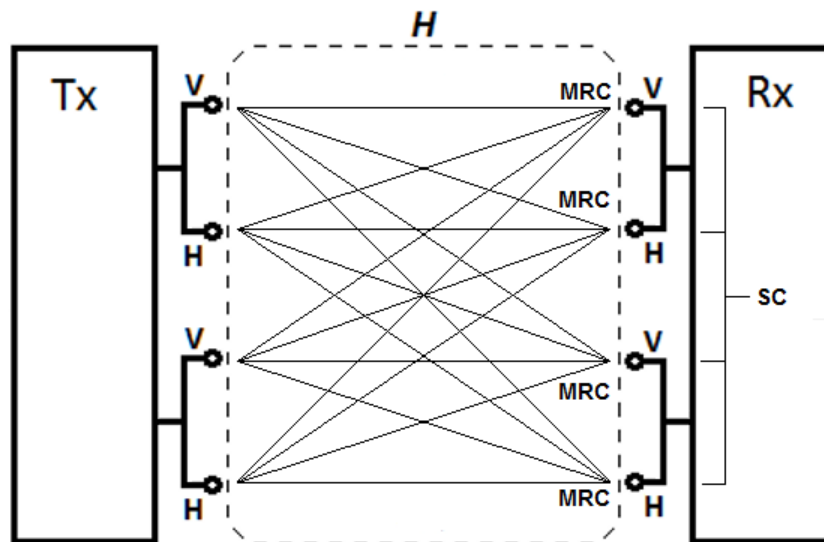


Figure 5-32: Polarisation diversity combination scheme for dual-polarised MIMO channel

Using the above combination scheme, the polarisation diversity gain for different polarisation setting can be computed at each measurement position. The heatmap below shows the diversity gain for differently polarised sub-channels, each row corresponds to data from one measurement position. The figure shows that diversity gain is also dependent on the frequency, which is a consequence of the frequency selective behaviour of the polarisation fading exhibited in section 5.3. Furthermore, cross-polarised sub-channels (HV and VH) shows greater diversity gain than co-polarised channels, which is expected for the low 3dB value of XPD for the (small cells) measurement environment. It is interesting to note that due to the periodic variation of sub-channel signal strength demonstrated by results from previous sections, the range of frequencies corresponding to the highest diversity gain is different for HV and VH. This is very useful and can be exploited by selecting the polarisation setting with the highest gains for each frequency.

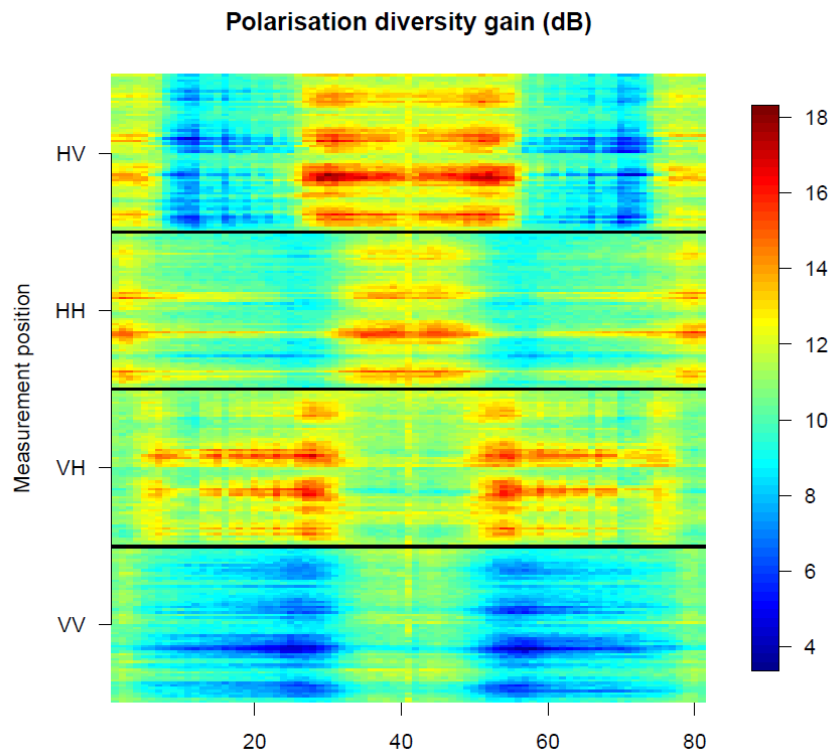
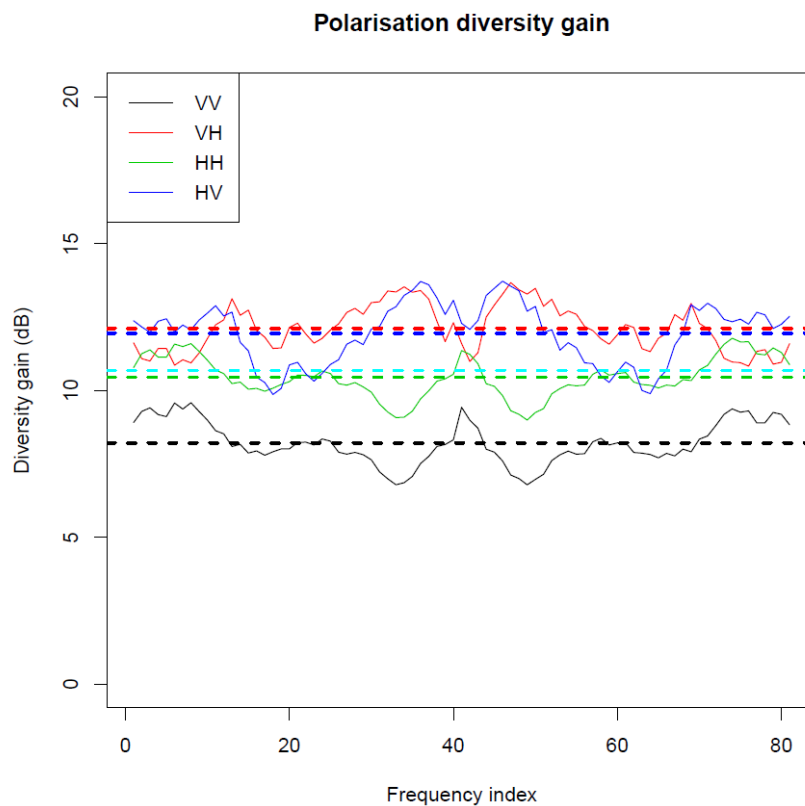


Figure 5-33: Polarisation diversity gain for each polarisation setting across different frequencies

Figure 5-34 shows the average polarisation diversity gain across all measurement positions for each of the 4 possible polarisation settings. The dotted lines, with colours corresponding to the legend, indicate the mean diversity gain after further averaging across frequencies. The cyan dotted line represents the overall mean diversity gain. As can be seen from the figure, the gain for cross-polarised sub-channels VH and HV are very close to each other and significantly higher than co-polarised sub-channels. The gains for VH and HV are 12.2dB and 12.1dB respectively. For co-polarised channels, VV (7.9dB) has far the lower diversity gain than HH (10.4dB) and is the lowest overall. This is because previous results revealed that VV sub-channels has the highest signal strength and therefore the vertical component of the XPD,  $X_v$ , is the highest, which leads to lower diversity gains for VV. The overall mean polarisation diversity gain is 10.6dB.



**Figure 5-34: Mean polarisation diversity gain across all measurement positions for differently polarised sub-channels**

Figure 5-35 shows the histograms of raw channel power for differently polarised sub-channels in comparison to the power achieved after applying the proposed polarisation combination scheme shown in Figure 5-32. By visual inspection, the application of polarisation diversity makes the distribution of channel power less skewed than individual polarisations, as a result, diversity gain is achieved.

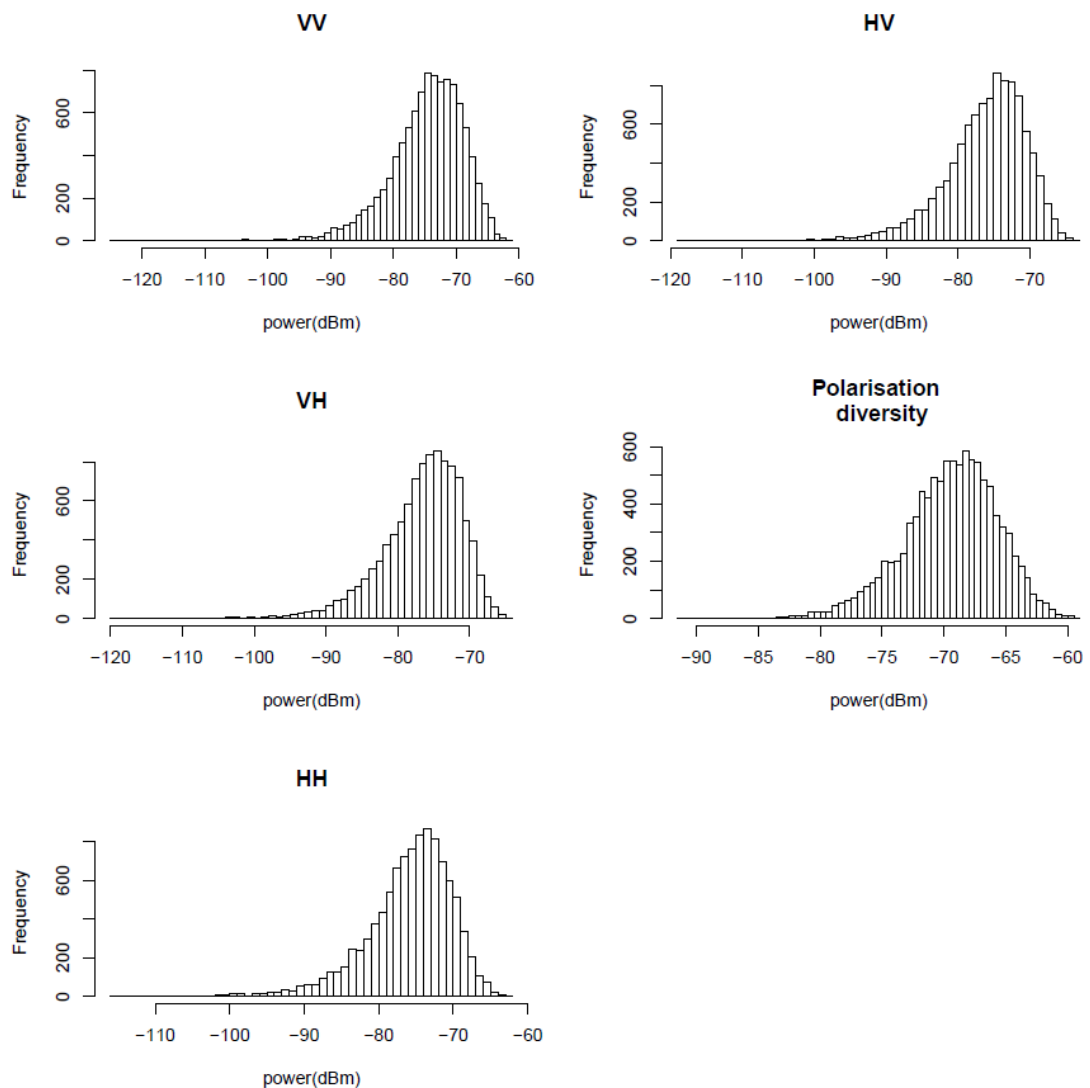
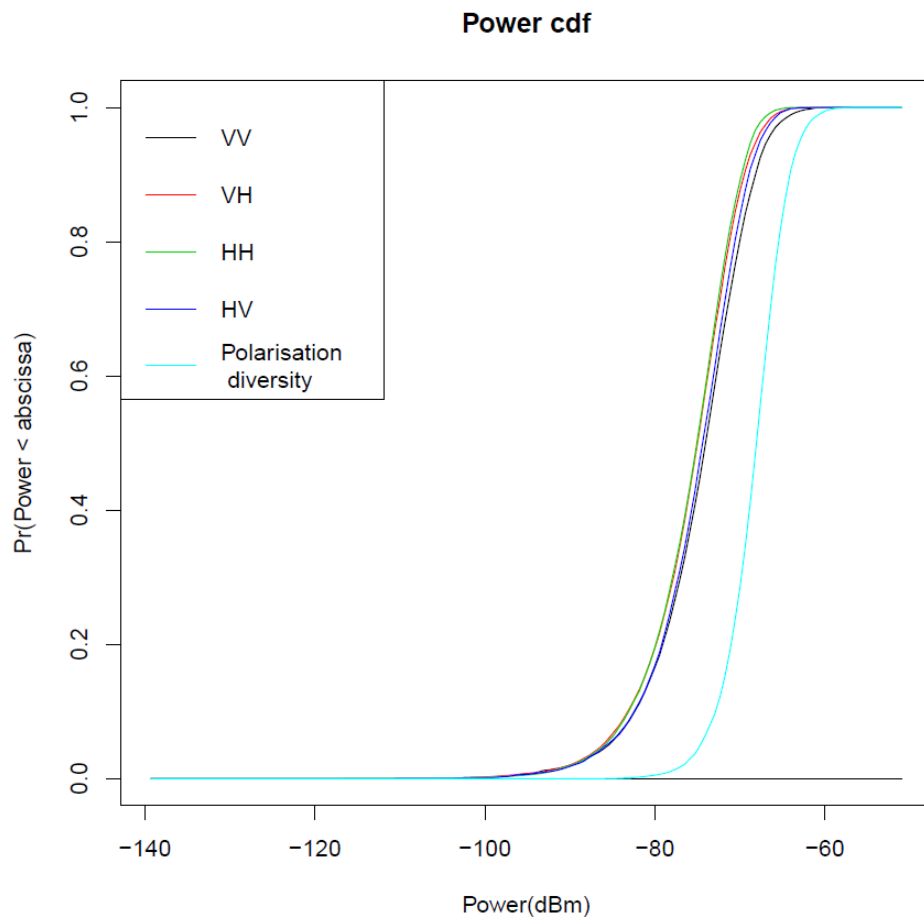


Figure 5-35: Histograms of the raw channel power for different polarisation settings in comparison with power achieved through proposed diversity combining scheme



Figure 5-36 show the CDF of the sub-channel power for different polarisation settings in comparison with channel power after polarisation diversity combining scheme. The ordinate shows the probability that the channel power is smaller than the power on the corresponding abscissa. As can be seen the polarisation diversity achieves a significant gain over individually polarised sub-channels. The median, or 50<sup>th</sup> percentile, channel power from the diversity scheme is -67dB compared to -75 to -76dB for individual sub-channels.



**Figure 5-36: CDF of sub-channel power for different polarisation settings in comparison with polarisation diversity combining scheme**

## 5.6 Summary

This chapter presented detailed investigation into the polarisation aspect of dual-polarised MIMO channel in small cell environments. The first part of the chapter, from section 5.2 to 5.3, studied the variation of sub-channel power and phase with respect to polarisation, frequency and receiver orientation. A clear and consistent difference emerged between co-polar and cross-polar channels across the measurement positions. The VV setting generally performed the best with mean received signal strength 6 dB higher than the setting with the lowest average, HH. The average XPD was evaluated at 3dB, which prompted the polarisation diversity study in section 5.5.

For co-polar settings, the sub-channel power is consistent with respect to frequency, whilst as for cross-polar sub-channels the signal strength varies by up to 12 dB across different frequencies. This difference is consistently found in all measurement points. The mean received power of VH and HV sub-channels averaged across 81 frequencies are almost identical, but at individual frequency points, the received power of VH and HV sub channels differs by over 3dB for over 75% of the frequencies. These two results provide great potential for polarisation diversity with respect to frequency.

The signal strength across different Rx orientations varies by up to 6dB, with VV exhibiting the highest average sub-channel power, see Figure 5-13. On the other hand, polarisation settings do not appear to significantly affect the signal phase distribution, see Figure 5.6. The signal phase in general sense approximately follows uniform distribution, except at 5 sampling frequencies which include the central frequency 2.6GHz. The five frequencies are sequential with fixed interval in-between and symmetrical about the central frequency. A distribution test with k-s approach reveals that the phase distribution at these frequencies all rejected uniformity. This is most likely caused by antenna array calibration.

The second part of the chapter, in section 5.4, studied the correlation between sub-channels of different polarisations. Polarisation settings have great impact on the correlation between signals of different frequencies. The signal correlation observed across the frequency domain exhibit different patterns under different polarisation settings. Explicitly, for co-polarised settings the pattern forms diagonal stripes, whereas for cross-polarised settings pattern shows chequered boxes. See Figure 5-16 and Figure 5-20.

Polarisation settings do not show significant effects on the correlation between signals of different receiver orientations. See Figure 5-22 - Figure 5-24. The gap between the five frequency sample points where the phase data lose uniformity (Figure 5-10) is linked with the interval between stripes shown on the correlation heatmap with respect to frequency, of signal phase (Figure 5-18) and the peak-to-trough distance of signal strength observed across the frequency domain for cross-polarised settings (Figure 5-5).

Polarisation settings impact the coherence bandwidth of wireless channel. Based on the experimental data, the coherence bandwidth is wider for co-polarised settings than cross-polarised settings, and wider for the VV setting than the HH setting, see Figure 5-26. The amplitude, phase and signal correlation patterns across different measurement sites are universal and not position specific.

The last part of this chapter, in section 5.5, studied polarisation diversity in dual-polarised MIMO channels. This section builds upon the signal power results from section 5.3 and signal correlation results from section 5.4 as power and correlation are the two main determination factors of potential polarisation diversity gain. By exploiting the differences in signal power and correlation between co-polar and cross-polar sub channels, and between different frequencies, a new diversity combination scheme is proposed and is shown to provide a 10.6dB overall diversity gain.

## CHAPTER 6

### CONCLUSIONS AND FUTURE WORK

*This Chapter concludes the thesis, and discuss the potential directions that can be followed to build on the work presented.*

## 6.1 Conclusions

This study has shed new light on the characteristic and properties of the wireless channel in small cells environments, including I2I, I2O and IOI scenarios. Due to the availability of comprehensive and rare data, this work was able to look into and investigate many different aspects of a wireless channel closely corresponding to that of the small cell propagation environment, including: path loss, wall penetration factor, environmental variation, delay spread, coherence bandwidth, angular spread, antenna orientation & polarisation, sub-channel frequency, correlation, power distribution, phase and polarisation diversity.

The objectives of this research consists of two main aspects: firstly to model the small cells wireless channel, and secondly to characterise the said channel. These objectives have been successfully met via the investigations presented in this thesis. Chapter 3 produced and validated an empirical path loss model that gives accurate results for small cell environments, whilst Chapters 4 and 5 successfully characterised the channel with respect to several independent variables, including environment, frequency, polarisation, antenna orientation.

The main contributions of the work are structured into two parts, organised in chapters 3 to 5. The first part includes chapters 3 and 4 where the main contribution is the characterisation and modelling of extensive channel data using well established methods in the field of wireless communications. The soundness of the methods employed are well known and results are subsequently of significance. The novelty of this part of the investigation comes from the comparisons of the channel parameters between different types of small cells propagation scenarios, including I2I, I2O and IOI. This is also the case for the path loss model as well which provides good accuracy in all types of small cell environments. The path loss model was validated by a second dataset measured in another small cell environment which also features I2I, I2O and IOI propagation.

By distinguishing these different environments, the model can be quickly implemented for system level simulations without requiring much equipment and computation power. As for the key channel parameters of RMS delay spread, coherence bandwidth and RMS angular spread, comparisons of their values between scenarios provides useful characterisation of the small cell wireless propagation channel. The results are useful of a range of wireless network planning applications, from determining the maximum transmission rate to sustaining reliable reception via waveform design and choice of bandwidth.

The second part of the contribution correspond to chapter 5. In the first half a number of well-established techniques from the fields of statistics and engineering were employed to study antenna polarisation effects of MIMO channels in small cells environment from a data oriented perspective. Given that both the data and the methodology employed to study the data are rarely seen before in the field of wireless communication, it is unsurprising that similar finding are not previously reported in the literature.

Although the methods employed are in a sense novel, there are strong indications that the results of the investigation are valid. Firstly the techniques employed are proven and effective in other research areas, and have been carefully applied to wireless channel characterisation. Secondly, doubts about the findings happening by chance due to inconsistencies in the source data were addressed when the findings were validated statistically across all measurement positions. With the concerns addressed, the novelty of the approach in this part of the study turns into a strength and give the thesis originality. The finding in this part of the study reveals many well-structured patterns in the sub-channel signal strength and correlation, which provides the prerequisite step before potential exploitation and utilisation.

In terms of topic of study, this part of the investigation focused on the variations in sub-channel power and correlations with respect to antenna polarisation, channel frequency, and receiver orientation. A clear and consistent difference emerged between co-polar and cross-polar sub-channels in their variation of signal power across different frequencies. This result, together with periodic power patterns in cross-polar sub-channels seen in section 5.3 and the 3dB value found for the XPD of this small cells environment, provides high digress of diversity and naturally encourages the studying of polarisation diversity, which was in turn carried out in chapter 5.

Using the results of sub-channel power, sub-channel correlation and cross polar discrimination from sections 5.3 and 5.4, a polarisation diversity study for dual-polarised MIMO channel was carried out. The study produced a new diversity combination scheme that takes advantage of the variations in sub-channel power and correlation, in conjunction with frequency, for cross-polar channels. By employing a combination of MRC and SC at different stages of the process the diversity combination scheme achieved an overall mean diversity gain of 10.6dB across the different types of small cell environments present in the data.

In summary the exploration in this thesis produced a new path loss model and a new polarisation diversity combination scheme for dual-polarised channels in small cells environments. Moreover, comparisons of key channel parameters between different types of small cell environments provided in depth characterisation of the wireless propagation channel in small cells environments.

## 6.2 Future Work

Although much time was spent analysing the data looking for predictable structures and verifying the results, not enough time was focused on looking at the potential implications and applications of the findings.

With regards to the first part of the study containing chapters 3 and 4, the empirical model can be improved in many aspects, such improving generalisation and considering more environmental factors. Or it could be used, along with the channel parameters, as references when constructing brand new propagation models. With the model as it is, efforts could be spent on looking to adapt it and other similar and related models into a practical system of small cell propagation prediction, and the channel parameters could be tested to tune or verify their value. Another line of investigation is to employ similar measurement techniques to the one presented in chapter to obtain similar data, then using the investigations already carried out in this work as a basis to look at other aspects of the data overlooked in this work, finally correlate and combine the results to obtain potential new models or new insights in relation to the channel.

With regards to chapter 5, one or two of the regular and periodic patterns are readily exploitable but most others require a lot more thought and consideration. However, as nearly all of human technology is, in one way or another, based on the fundamental concept of utilisation and exploitation of foreknowledge granted by predictions, and patterns are the prerequisite to predictions, in-depth investigation into the patterns revealed in this study with the aim of practical implementations offers one promising avenue of further research. Another path to follow is to adapt some of the techniques used in this chapter to other data to look for new patterns.



---

## BIBLIOGRAPHY

- [1] V. Chandrasekhar, J. Andrews and A. Gatherer, "Femtocell networks: a survey," *IEEE Communications Magazine*, vol. 46, no. 9, pp. 59-67, 2008.
- [2] "Informa Telecoms & Media," [Online]. Available: <http://www.informatandm.com/>. [Accessed 10 11 2012].
- [3] Cisco, "Cisco Visual Networking Index: Forecast and Methodology, 2012–2017," 29 May 2013. [Online]. Available: [http://www.cisco.com/en/US/solutions/collateral/ns341/ns525/ns537/ns705/ns827/white\\_paper\\_c11-481360.pdf](http://www.cisco.com/en/US/solutions/collateral/ns341/ns525/ns537/ns705/ns827/white_paper_c11-481360.pdf). [Accessed 10 July 2013].
- [4] H. T. Dinh, C. Lee, D. Niyato and P. Wang, "A Survey of Mobile Cloud Computing: Architecture, Applications and Approaches," *Wireless Communications and Mobile Computing, Wiley Journals*, 2011.
- [5] A. Karalisa, J. D. Joannopoulosb and M. Soljacic, "Efficient wireless non-radiative mid-range energy transfer," *Annals of Physics*, vol. 323, no. 1, p. 34–48, Jan. 2008.
- [6] "Small Cell Forum," [Online]. Available: <http://www.smallcellforum.org/>. [Accessed 12 5 2013].
- [7] "Carriers see small cells as key to LTE-Advanced," RCR Wireless, [Online]. Available: <http://www.rcrwireless.com/article/20111103/carriers/carriers-see-small-cells-as-key-to-making-lte-pay/>. [Accessed 14 2 2012].

- [8] "HetNet Market Summary & Forecasts: Macro Cells, Small Cells & Wi-Fi Offload," ARCchart, [Online]. Available: <http://www.arcchart.com/reports/heterogeneous-networks-hetnets-report.asp>. [Accessed 17 11 2012].
- [9] A. R. Mishra, *Fundamentals of Cellular Network Planning and Optimisation: 2G/2.5G/3G... Evolution to 4G*, John Wiley & Sons, 2004.
- [10] W. C. Y. Lee, "Effects on Correlation Between Two Mobile Radio Base-Station Antennas," *IEEE Transactions on Communications*, vol. 21, no. 11, pp. 1214-1224, Nov 1973.
- [11] R. Clarke, "A statistical theory of mobile-radio reception," *Bell Systems Technical Journal*, pp. 957-1000, Jul.-Aug. 1968.
- [12] P. L. Rice, A. G. Longley, K. A. Norton and A. P. Barsis, "Transmission loss predictions for tropospheric communications circuits," U.S. Dept. of Commerce National Telecommunications & Information Administration, Institute for Telecommunications Sciences (NTIA-ITS), Technical Note 101, revised 1/1/1967.
- [13] M. Nakagami and W. G. Hoffman, "The m-distribution, a general formula of intensity distribution of rapid fading," *Statistical Methods in Radio Wave Propagation*, 1960.
- [14] N. Sagias, D. Zogas, G. Karagiannidis and G. Tombras, "Channel capacity and second-order statistics in Weibull fading," *IEEE Communications Letters*, vol. 8, no. 6, pp. 377-379, June 2004.
- [15] C. Loo, "A statistical model for a land mobile satellite link," *IEEE Transactions on Vehicular Technology*, vol. 34, no. 3, pp. 122-127, Aug. 1985.

- [16] W. R. Hoefer, "The Transmission-Line Matrix Method - Theory and Applications," *IEEE Transactions on Microwave Theory and Techniques*, vol. 33, no. 10, pp. 882 - 893, Oct. 1985.
- [17] J.-M. Gorce, K. Jaffres-Runser and G. de la Roche, "Deterministic Approach for Fast Simulations of Indoor Radio Wave Propagation," *Antennas and Propagation, IEEE Transactions on*, vol. 55, no. 3, pp. 938 - 948, Mar. 2007.
- [18] G. Rodriguez, Y. Miyazaki and N. Goto, "Matrix-based FDTD parallel algorithm for big areas and its applications to high-speed wireless communications," *IEEE Transactions on Antennas and Propagation*, vol. 54, no. 3, pp. 785 - 796, Mar. 2006.
- [19] H.-R. Chuang and L.-C. Kuo, "3-D FDTD design analysis of a 2.4-GHz polarization-diversity printed dipole antenna with integrated balun and polarization-switching circuit for WLAN and wireless communication applications," *IEEE Transactions on Microwave Theory and Techniques*, vol. 51, no. 2, pp. 374 - 381, Feb. 2003.
- [20] A. Valcarce, D. Lopez-Perez, G. de la Roche and J. Zhang, "Predicting Small-Scale Fading Distributions with Finite-Difference Methods in Indoor-to-Outdoor Scenarios," in *Vehicular Technology Conference, IEEE 69th*, April 2009.
- [21] B. Zhang, Z. Xue, W. Ren, W. Li and X. Sheng, "Accelerating FDTD algorithm using GPU computing," *2011 IEEE International Conference on Microwave Technology & Computational Electromagnetics (ICMTCE)*, pp. 410 - 413, May 2011.
- [22] T. Nagaoka and S. Watanabe, "Accelerating three-dimensional FDTD calculations on GPU clusters for electromagnetic field simulation," *2012*

---

*Annual International Conference of the IEEE on Engineering in Medicine and Biology Society (EMBC)*, pp. 5691-5.

- [23] L. Mattes and S. Kofuji, "Overcoming the GPU memory limitation on FDTD through the use of overlapping subgrids," *2010 International Conference on Microwave and Millimeter Wave Technology (ICMMT)*, pp. 1536 - 1539, May 2010.
- [24] Z. Yun, S. Lim and M. Iskander, "An Integrated Method of Ray Tracing and Genetic Algorithm for Optimizing Coverage in Indoor Wireless Networks," *IEEE Antennas and Wireless Propagation Letters*, vol. 7, pp. 145 - 148, 2008.
- [25] G. Durgin, N. Patwari and T. Rappaport, "Improved 3D ray launching method for wireless propagation prediction," *Electronics Letters*, vol. 33, no. 16, pp. 1412 - 1413, Jul. 1997.
- [26] A. Schmitz, T. Rick, T. Karolski, L. Kobbelt and T. Kuhlen, "Beam tracing for multipath propagation in urban environments," *3rd European Conference on Antennas and Propagation*, pp. 2631 - 2635, Mar. 2009.
- [27] Z. Lai, N. Bessis, G. de la Roche, P. Kuonen, J. Zhang and G. Clapworthy, "The Development of a Parallel Ray Launching Algorithm for Wireless Network Planning," *International Journal of Distributed Systems and Technologies*, 2010.
- [28] COST Action 231, "Digital mobile radio towards future generation systems, final report," tech. rep., European Communities, EUR 18957, 1999.

- 
- [29] J. Walfisch and H. L. Bertoni, "A theoretical model of UHF propagation in urban environments," *IEEE Transactions on Antennas and Propagation*, vol. 36, no. 12, pp. 1788-1796, Dec. 1988.
- [30] F. Ikegami, S. Yoshida, T. Takeuchi and M. Umehira, "Propagation factors controlling mean field strength on urban streets," *IEEE Transactions on Antennas and Propagation*, vol. 32, no. 9, pp. 822-829, Aug 1984.
- [31] J. M. Keenan and A. J. Motley, "Radio Coverage in Buildings," *British Telecom Technology Journal*, vol. 8, no. 1, pp. 19-24, Jan. 1990.
- [32] "AWE Communication," [Online]. Available: [www.awe-communication.com](http://www.awe-communication.com). [Accessed 27 01 2012].
- [33] K.-W. Cheung, J.-M. Sau and R. Murch, "A new empirical model for indoor propagation prediction," *IEEE Transactions on Vehicular Technology*, vol. 47, no. 3, pp. 996-1001, Aug. 1998.
- [34] A. G. M. Lima and L. Menezes, "Motley-Keenan model adjusted to the thickness of the wall," in *2005 SBMO/IEEE MTT-S International Conference on Microwave and Optoelectronics*, July 2005.
- [35] A. Aragon-Zavala, B. Belloul, V. Nikolopoulos and S. Saunders, "Accuracy evaluation analysis for indoor measurement-based radio-wave-propagation predictions," *IEE Proceedings - Microwaves, Antennas and Propagation*, vol. 153, no. 1, pp. 67-74, Feb. 2006.
- [36] Y. Solahuddin and R. Mardeni, "Indoor empirical path loss prediction model for 2.4 GHz 802.11n network," in *2011 IEEE International Conference on Control System, Computing and Engineering (ICCSCE)*, Nov. 2011.

- [37] Y. Okumura, E. Ohmori, T. Kawano and K. Fukuda, "Field strength and its variability in VHF and UHF land-mobile," *Review of the Electrical Communication Laboratory*, pp. 825 - 873, 1968.
- [38] M. Hatay, "Empirical formula for propagation loss in land mobile radio services," *IEEE Transactions on Vehicular Technology*, vol. 29, no. 3, pp. 317 - 325, Aug. 1980.
- [39] G. de La Roche, A. Valcarce and J. Zhang, "Hybrid Model for Indoor-to-Outdoor Femtocell Radio Coverage Prediction," in *IEEE 73rd Vehicular Technology Conference*, Budapest, May 2011.
- [40] Z. Ji, B.-H. Li, H.-X. Wang, H.-Y. Chen and T. Sarkar, "Efficient ray-tracing methods for propagation prediction for indoor wireless communications," *IEEE Antennas and Propagation Magazine*, vol. 43, no. 2, pp. 41 - 49, Apr. 2001.
- [41] T. Kurner and A. Meier, "Prediction of outdoor and outdoor-to-indoor coverage in urban areas at 1.8 GHz," *IEEE Journal on Selected Areas in Communications*, vol. 20, no. 3, pp. 496 - 506, Apr. 2002.
- [42] G. de la Roche, P. Flipo, Z. Lai, G. Villemaud, J. Zhang and J.-M. Gorce, "Combination of geometric and finite difference models for radio wave propagation in outdoor to indoor scenarios," *2010 Proceedings of the Fourth European Conference on Antennas and Propagation (EuCAP)*, pp. 1-5, Apr. 2010.
- [43] V. Chandrasekhar and J. Andrews, "Uplink capacity and interference avoidance for two-tier femtocell networks," *IEEE Transactions on Wireless Communications*, vol. 8, no. 7, pp. 3498-3509, July 2009.

- [44] D. Lopez-Perez, A. Valcarce, G. de la Roche and J. Zhang, "OFDMA Femtocells: A Roadmap on Interference Avoidance," *IEEE Communications Magazine*, vol. 47, no. 9, pp. 41-48, 2009.
- [45] R. ITU-R, "Propagation data and prediction methods for the planning of short-range outdoor radio communication systems and radio local area networks in the frequency range 300 MHz and 100 GHz," tech. rep., p. 1411 & p. 1238.
- [46] V. Erceg and K. V. S. Hari et al., "Channel models for fixed wireless applications," tech. rep., IEEE 802.16 Broadband Wireless Access Working Group, Jan. 2001.
- [47] J. Kivinen, X. Zhao and P. Vainikainen, "Empirical characterization of wideband indoor radio channel at 5.3 GHz," *Antennas and Propagation, IEEE Transactions on*, vol. 49, no. 8, pp. 1192-1203, Aug. 2001.
- [48] P. Kyösti et al., "WINNER II channel models," WINER II Public Deliverable, pp.42–44, Sep. 2007.
- [49] OFCOM, "Predicting coverage and interference involving the indoor-outdoor interface," Tech. Rep., 2007.
- [50] A. Valcarce and J. Zhang, "Empirical Indoor-to-Outdoor Propagation Model for Residential Areas at 0.9–3.5 GHz," *Antennas and Wireless Propagation Letters, IEEE*, vol. 9, pp. 682-685, 2010.
- [51] D. Umansky, G. de la Roche, Z. Lai, G. Villemaud, J.-M. Gorce and J. Zhang, "A New Deterministic Hybrid Model for Indoor-to-Outdoor Radio Coverage Prediction," in *Antennas and Propagation, European Conference on*, Rome, Apr. 2011.

- [52] G. de la Roche, D. Umansky, Z. Lai, G. Villemaud, J.-M. Gorce and J. Zhang, "Antenna Height Compensation for an Indoor to Outdoor Channel model based on a 2D Finite Difference Model," in *29th Progress In Electromagnetics Research Symposium (PIERS)*, Marrakesh, Mar. 2011.
- [53] X. Gao, A. Glazunov, J. Weng, C. Fang, J. Zhang and F. Tufvesson, "Channel measurement and characterization of interference between residential femto-cell systems," in *Proceedings of the 5th European Conference on Antennas and Propagation (EUCAP)*, pp. 376, 2011.
- [54] V. M. Kolmonen and e. al., "A Dynamic Dual-Link Wideband MIMO Channel Sounder for 5.3 GHz," *Instrumentation and Measurement, IEEE Transactions on*, vol. 59, no. 4, pp. 873-883, April 2010.
- [55] "Channel Sounder," [Online]. Available: <http://www.channelsounder.de/ruskchannelsounder.html>. [Accessed May 2013].
- [56] MEDAV GmbH, "Antenna Array Calibration and MIMO Channel Sounding," 2008. [Online]. Available: [http://www.medav.de/fileadmin/redaktion/documents/English/competence\\_antenna\\_e.pdf](http://www.medav.de/fileadmin/redaktion/documents/English/competence_antenna_e.pdf). [Accessed 12 July 2013].
- [57] A. Boettcher, C. Schneider, M. Narandzic, P. Vary and R. S. Thomae, "Power and delay domain parameters of channel measurements at 2.53 GHz in an urban macro cell scenario," in *2010 Proceedings of the Fourth European Conference on Antennas and Propagation (EuCAP)*, 2010.
- [58] P. Almers et al., "Survey of channel and radio propagation models for wireless MIMO systems," *EURASIP Journal on Wireless Communications and Networking*, vol. 2007, p. 19070 (19pp), 2007.



- [59] L. Correia, *Mobile Broadband Multimedia Networks*, Academic Press, 2006.
- [60] "3GPP Specification 25.996," [Online]. Available: <http://www.3gpp.org/ftp/specs/html-INFO/25996.htm>. [Accessed May 2013].
- [61] J. Poutanen, K. Haneda, L. Liu, C. Oestges, F. Tufvesson and P. Vainikainen, "Parameterization of the COST 2100 MIMO channel model in indoor scenarios," in *Proceedings of the 5th European Conference on Antennas and Propagation*, April 2011.
- [62] C. Fang, B. Allen, E. Liu, J. Zhang, A. Glazunov and F. Tufvesson, "Empirical indoor-to-outdoor and building-to-building propagation model at 2.6 GHz," in *IC1004 Joint workshop on Small Cell Cooperative Communications*, Lyon, May 2012.
- [63] C. Fang, B. Allen, E. Liu, P. Karadimas, J. Zhang, A. Glazunov and F. Tufvesson, "Indoor-indoor and indoor-outdoor propagation trial results at 2.6 GHz," in *Loughborough Antenna and Propagation Conference*, Loughborough , Nov 2012.
- [64] B. Allen, J. Webber, P. Karlsson and M. Beach, "UMTS spatio-temporal propagation trial results," in *Eleventh International Conference on Antennas and Propagation*, 2001.
- [65] S. Ghassemzadeh, R. Jana, C. Rice, W. Turin and V. Tarokh, "Measurement and modeling of an ultra-wide bandwidth indoor channel," *IEEE Transactions on Communications*, vol. 52, no. 10, pp. 1786- 1796, Oct. 2004.

- 
- [66] A. Ribeiro, C. Castelli, E. Barrientos and E. Conforti, "Coherence bandwidth in a 1.8-GHz urban mobile radio channel," in *Microwave and Optoelectronics Conference*, IMOC 2007.
- [67] M. Al-Nuaimi and A. Siamarou, "Coherence bandwidth characterisation and estimation for indoor Rician multipath wireless channels using measurements at 62.4GHz," *IEE Proceedings on Microwaves, Antennas and Propagation*, vol. 149, no. 3, pp. 181- 187, Jun 2002.
- [68] N. Czink, E. Bonek, X. Yin and B. Fleury, "Cluster angular spreads in a MIMO indoor propagation environment," in *IEEE 16th International Symposium on Personal, Indoor and Mobile Radio Communications. PIMRC 2005*, 2005.
- [69] A. Paulraj, R. Roy and T. Kailath, "Estimation Of Signal Parameters Via Rotational Invariance Techniques - Esprit," in *Nineteenth Asilomar Conference on Circuits, Systems and Computers*, 1985.
- [70] M. Shafi, M. Zhang, A. Moustakas, P. Smith, A. Molisch, F. Tufvesson and S. Simon, "Polarized MIMO channels in 3-D: models, measurements and mutual information," *IEEE Journal on Selected Areas in Communications*, vol. 24, no. 3, pp. 514-527, Mar. 2006.
- [71] R. Vaughan, "Polarisation diversity in mobile communications," *IEEE Transactions on Vehicular Technology*, vol. 39, no. 3, p. 177–185, Jun. 1990.
- [72] S. Kozono, T. Suruhara and M. Sakamoto, "Base station polarization diversity reception for mobile radio," *IEEE Transactions on Vehicular Technology*, vol. 33, no. 4, p. 301–306, Nov. 1984.

- 
- [73] T. Mao, "Radiation Characterization of Slant Polarization Antennas," *Microwave Journal*, May 1999.
- [74] X. Quan, R. Li, Y. Fan and D. Anagnostou, "Analysis and Design of a 45<sup>°</sup> Slant-Polarized Omnidirectional Antenna," *IEEE Transactions on Antennas and Propagation*, vol. 62, no. 1, pp. 86-93, Jan. 2014.
- [75] Y. Benjamini, "Opening the Box of a Boxplot," *The American Statistician*, 1988.
- [76] J. M. Chambers, W. S. Cleveland, B. Kleiner and P. A. Tukey, *Graphical Methods for Data Analysis*, Wadsworth & Brooks/Cole, 1983.
- [77] M. Wilk and R. Gnanadesikan, "Probability plotting methods for the analysis of data," *Biometrika*, vol. 55, no. 1, pp. 1-17, 1968.
- [78] R. A. Becker, J. M. Chambers and A. R. Wilks, *The New S Language*, Wadsworth & Brooks/Cole., 1988.
- [79] W. A. Shewhart, *Statistical Method from the Viewpoint of Quality Control*, 1939.
- [80] J. S. Oakland, *Statistical Process Control*, New York: Wiley, 2002.
- [81] W. A. Shewhart, *Economic Control of Quality of Manufactured Product*, Van Nordstrom, 1931, p. 1931.
- [82] R. Nancy, *Tague's The Quality Toolbox*, Second Edition, ASQ Quality Press, p.155-158, 2004.
- [83] A. Kolmogorov, "Sulla determinazione empirica di una legge di distribuzione (On the empirical determination of a distribution law)," *Giorn. Ist. Ital. Attuari*, vol. 4, pp. 83-91, 1933.

- 
- [84] N. Smirnov, "Tables for estimating the goodness of fit of empirical distributions," *Annals of Mathematical Statistics*, vol. 19, pp. 279-281, 1948.
- [85] W. J. Conover, *Practical Nonparametric Statistics*, New York: John Wiley & Sons. p.295–314, 1971.
- [86] M. Hollander and D. A. Wolfe, *Nonparametric Statistical Methods.*, New York: John Wiley & Sons, 1999.
- [87] D. F. Bauer, "Constructing confidence sets using rank statistics," *Journal of the American Statistical Association*, vol. 67, pp. 687-690, 1972.
- [88] K. Pearson, "Notes on the history of correlation," *Biometrika*, vol. 13, pp. 25-45, 1920, Reprinted in Pearson and Kendall, 1970, 185-205.
- [89] J. L. Rodgers and W. A. Nicewander, "Thirteen ways to look at the correlation coefficient," *The American Statistician*, vol. 42, no. 1, pp. 59-66, 1988.
- [90] E. Hoong, "Application of Paired t-test and DOE Methodologies on RFID Tag Placement Testing using Free Space Read Distance," in *IEEE International Conference on RFID*, Grapevine, TX, 26-28 March 2007.
- [91] G. Casella and R. L. Berger, *Statistical inference*, Thomson Learning, 2002.
- [92] J. Rice, *Mathematical Statistics and Data Analysis*, Duxbury Press, Apr 2006.
- [93] N. Rahman, *A Course in Theoretical Statistics*, London: C. Griffin, 1968.
- [94] M. Kendall and A. Stuart, *The Advanced Theory of Statistics, Volume 2: Inference and Relationship*, London: C. Griffin, 1973.

- 
- [95] G. S. N. Raju, *Antennas and wave propagation*, Pearson Education India,, 2006.
- [96] F. Qureshi, M. Antoniadis and G. V. Eleftheriades, "A compact and low-profile metamaterial ring antenna with vertical polarization," *IEEE Antennas and Wireless Propagation Letters*, vol. 4, pp. 333-336, 2005.
- [97] P. Kyritsi and D. C. Cox, "Propagation characteristics of horizontally and vertically polarized electric fields in an indoor environment: simple model and results," in *IEEE Vehicular Technology Conference*, Vol. 3, pp. 1422-1426, 2001.
- [98] C.M.Cuadras, "Geometrical Understanding of the Cauchy Distribution," *Questiio*, vol. 26, pp. 283-287, 2002.
- [99] E. Telatar, "Capacity of Multi-antenna Gaussian Channels," *European Transactions on Telecommunications*, vol. 10, no. 6, pp. 585-595, 1999.
- [100] J. Hogema, "Shot Group Statistics," 2 2005. [Online]. Available: [http://home.kpn.nl/jhhogema1966/skeetn/ballist/sgs/sgs.htm#\\_Toc96439743](http://home.kpn.nl/jhhogema1966/skeetn/ballist/sgs/sgs.htm#_Toc96439743). [Accessed 8 3 2104].
- [101] R. Verdone and A. Zanella, *Pervasive Mobile and Ambient Wireless Communications: COST Action 2100.*, Springer Science & Business Media., 2012.
- [102] C. B. Dietrich Jr, K. Dietze, J. R. Nealy and W. L. Stutzman, "Spatial, polarization, and pattern diversity for wireless handheld terminals," *IEEE Transactions on Antennas and Propagation*, vol. 49, no. 9, pp. 1271-1281, 2001.

- 
- [103] D. S. Shiu, G. J. Foschini, M. J. Gans and J. M. Kahn, "Fading correlation and its effect on the capacity of multielement antenna systems," *IEEE Transactions on Communications*, vol. 48, no. 3, pp. 502-513, 2000.
- [104] V. Erceg, P. Soma, D. S. Baum and S. Catreux, "Multiple-input multiple-output fixed wireless radio channel measurements and modeling using dual-polarized antennas at 2.5 GHz.," *IEEE Transactions on Wireless Communications*, vol. 3, no. 6, pp. 2288-2298, 2004.
- [105] J. Jootar and J. R. Zeidler, "Performance analysis of polarization receive diversity in correlated Rayleigh fading channels," in *IEEE Global Telecommunications Conference, 2003*, Vol. 2, pp. 774-778, 2003.
- [106] Z. Shen, J. G. Andrews and B. L. Evans, "Upper bounds on MIMO channel capacity with channel Frobenius norm constraints," in *IEEE Global Telecommunications Conference, GLOBECOM'05*, Vol. 3, pp. 5-pp, 2005..
- [107] R. U. Nabar, V. Erceg, H. Bölcskei and A. J. Paulraj, "Performance of multi-antenna signaling strategies using dual-polarized antennas: Measurement results and analysis.," *Wireless Personal Communications*, no. 23(1), pp. 31-44, 2002.
- [108] Z. Zhang, Z. Yun and M. F. Iskander, "Ray tracing method for propagation models in wireless communication systems," *Electronics Letters*, vol. 36, no. 5, pp. 464-465, Mar 2000.
- [109] A. Molisch, "A generic model for MIMO wireless propagation channels in macro- and microcells," *IEEE Transactions on Signal Processing*, vol. 52, no. 1, pp. 61 - 71, Jan. 2004.

## LIST OF ACRONYMS

$\gamma$	Path loss exponent
$\theta_{rms}$	Root Mean Squared Angular Spread
$\mu$	Mean
$\rho$	Correlation Coefficient
$\sigma$ , SD	Standard Deviation
$\sigma^2$	Variance
$\tau_{rms}$	Root Mean Squared Delay Spread
3GPP	3rd Generation Partnership Project
AoA	Angles of Arrival
Bc	Coherence Bandwidth
BS	Base Station
C/I	Carrier-to-Interference Ratio
CDF	Cumulative Distribution Function
CDMA	Code Division Multiple Access
CLC	Central Control Line
COST	European Cooperation in the Field of Scientific and Technical Research
DSL	Digital Subscriber Line
EGC	Equal-Gain Combining
EIRP	Equivalent Isotropically Radiated Power

FDTD	Finite-Difference Time-Domain
FFT	Fast Fourier Transform
GPU	Graphic Processing Unit
GSM	Global System for Mobile Communications
$H(f)$	Channel Transfer Function
$h(t)$ , IR	Impulse Response
HetNet	Heterogeneous Networks
HH	Horizontal to Horizontal Polarisation
HV	Horizontal to Vertical Polarisation
I2I	Indoor to Indoor
I2O	Indoor to Outdoor
IOI	Indoor to Outdoor to Indoor
ITU	International Telecommunication Union
LCL	Lower Control Line
LLS	Linear Least Squares
LNA	Low Noise Amplifier
LOS	Line of Sight
LTE	Long Term Evolution
MIMO	Multiple Inputs Multiple Outputs
MRC	Maximal-Ratio Combining
NLOS	Non-Line of Sight
O2I	Outdoor to Indoor



PAS	Power Azimuth Spectrum
PDF	Probability Density Function
PDP	Power Delay Profile
PL	Path Loss
$PL_0$	Path loss at reference distance $d_0$
PLUL	Uplink Path Loss
QoS	Quality of Service
Rc	Receiver Column
RMSE	Root Mean Squared Error
Rx	Receiver
$Rx_H$	Horizontally Polarised Receiver Element
$Rx_V$	Vertically Polarised Receiver Element
SC	Selection Combining
SINR	Signal to Interference and Noise Ratio
SSDL	Downlink Signal Strength
SUI	Stanford University Interim
TD-SCDMA	Time Division Synchronous Code Division Multiple Access
TLM	Transmission Line Matrix
Tx	Transmitter
$Tx_H$	Horizontally Polarised Transmitter Element
$Tx_V$	Vertically Polarised Transmitter Element
UCL	Upper Control Line

UE	User Equipment
UMTS	Universal Mobile Telecommunication System
UTD	Universal Theory of Diffraction
VH	Vertical to Horizontal Polarisation
VV	Vertical to Vertical Polarisation
WCDMA	Wideband Code Division Multiple Access
WiMAX	Worldwide Interoperability for Microwave Access
WLAN	Wireless Local Area Networking
XPD	Cross-Polarisation Discrimination